RICE UNIVERSITY

A Real-time Snapshot Hyperspectral Endoscope and Miniature Endomicroscopy Objectives for a Two Field-Of-View (Bi-FOV) Endoscope.

by

Robert Timothy Kester

A THESIS SUBMITTED
IN PARTIAL FULFILLMENT OF THE
REQUIREMENTS FOR THE DEGREE

Doctor of Philosophy

APPROVED, THESIS COMMITTEE:

Tomasz Tkaczyk, Chair, Assistant Professor
Bioengineering, Electrical and Computer Engineering

Rebecca Richards-Kortum, Stanley C. Moore Professor
Bioengineering

Ann M. Gillenwater, Professor, Head and Neck Surgery
The University of Texas M. D. Anderson Cancer Center

Erzsebet Merenyi, Research Professor, Electrical and
Computer Engineering

HOUSTON, TEXAS
AUGUST 2010

UMI Number: 3425204

ProQuest LLC
789 East Eisenhower Parkway
P.O. Box 1346
Ann Arbor, MI 48106-1346

ABSTRACT

A Real-time Snapshot Hyperspectral Endoscope and Miniature Endomicroscopy Objectives for a Two Field-Of-View (Bi-FOV) Endoscope.

By

Robert Timothy Kester

This thesis focuses on the development of two novel imaging technologies which will serve as the basis for the future development of a two field-of-view or "Bi-FOV" endoscope capable of imaging at both microscopic and macroscopic regimes simultaneously. The goal of the Bi-FOV is to provide clinicians with a better tool for pre- and early cancer detection. The first technology developed makes it possible to obtain low cost, high performance, miniature optical systems for use in the microscopic portion of the Bi-FOV endoscope. The second technology developed for the Bi-FOV is a real-time snapshot hyperspectral endoscope called the IMS endoscope. The IMS endoscope is based on an image mapping technique which is capable of achieving high temporal and spatial resolution, excellent optical throughput, and low costs. The parallel, high throughput nature of this technique enables the device to operate at frame rates of 5.2 fps while collecting a 3D (x, y, λ) datacube of 350 x 350 x 48. We have successfully imaged tissue in vivo resolving tissue vasculature and oxy-hemoglobin which are important early cancer biomarkers.

Acknowledgements

I would like to thank my advisor, Dr. Tomasz Tkaczyk for your guidance and friendship over the past five years. Your vision, knowledge, creativity, and encouragement have made many things possible for me and the future looks even brighter. I also want to thank you for the cool thesis project which has been way more fun, challenging, and exciting than I could have imagined.

Many thanks to my committee members: Dr. Richards Kortum, Dr. Ann Gillenwater, and Dr. Erzsebet Merenyi for your expert advice and help along the way. I am honored to have such a great committee.

I would also like to thank my labmate Liang Gao for helping develop the image mapping spectrometry technique. This has been such a great adventure so far and I am looking forward to where it will go from here.

I would also like to thank Noah Bedard, and Dr. Nathan Hagan for helping me with my research and working on the software aspects of the IMS endoscope.

None of this would have been possible without the support of my lovely wife Eva, who has been there for me every step of the way. I love you. I would also like to thank my children, Noah, Sophie, and soon-to-be born Juliet (a.k.a baby Peanut) for keeping things in perspective and making me have fun along the way. You kids are great.

Most importantly, I would like to thank G-d and his son Jesus Christ for leading me through the difficult times, showing me unending love and mercy, and blessing me so richly along the journey of life.

This work was funded by NIH grants R01 CA124319, R01EB002179, R01CA103830, and R21EB009186.

Table of Contents

1. INTRODUCTION

1.1. Objective and Specific Aims

The objective of this research is to develop two critical technologies, low cost high performance miniature optics and real-time hyperspectral imaging. These technologies will be integrated into a single two field-of-views (macroscopic and microscopic) or Bi-FOV endoscope that will be used for the detection, screening, and monitoring of cancer and its precursors. The specific aims of this project are as follows:

Specific Aim 1: Develop a miniature, high performance endomicroscope objective for a confocal endomicroscope and evaluate its performance using optical calibration standards and biological models.

Specific Aim 2: Develop a real-time hyperspectral endoscope and evaluate its performance using optical calibration standards and biological models.

The outcome of this research will provide the necessary technological base for the design and construction of a single, integrated Bi-FOV endoscope that can be used in clinical studies.

1.2. Overview

This dissertation describes the development of low cost, high performance miniature optics for endoscopy, a real-time hyperspectral endoscope, and the future integration of these technologies into a Bi-FOV endoscope. The dissertation is organized as follows.

Chapter 1 lists the specific aims of the research and provides a brief overview of the topics to be discussed.

Chapter 2 provides background information on current trends in endoscopic technologies for both macroscopic and microscopic modalities as they relate to early cancer detection and why a dual mode Bi-FOV endoscope is needed.

The next few chapters (3-5) present the work that completes Specific Aim 1 of my research.

Chapter 3 describes the development of a high numerical aperture endomicroscope objective for a fiber confocal reflectance microscope. The technology developed for this objective achieves the unique combination of high performance, miniature size, and multi-function integration.

Chapter 4 describes the additional development of the technology in Chapter 3 to achieve low cost without sacrificing performance or size. The end result is a self aligning high numerical aperture endomicroscope objective that achieves diffraction limited performance and can be assembled in approximately 15 minutes.

Chapter 5 assesses the biological imaging performance and fabrication costs of these self-aligning miniature optical systems against other miniature systems and a high quality benchtop microscope objective.

Chapters 6 and 7 present the work that completes Specific Aim 2 of my research.

Chapter 6 describes the first real-time snapshot hyperspectral endoscope for early cancer diagnostics based on a new hyperspectral imaging technology called image mapping spectrometry (IMS). A prototype has been developed capable of acquiring 3D (x, y, λ) datacubes of 350 x 350 x 48 at a rate of 5.2 frames per second. Initial biological images of the lower lip of a normal human volunteer have been obtained through a fiber optic probe of diameter = 1mm.

Chapter 7 presents the development of the most critical component in the IMS endoscope called the image mapper. The image mappers are fabricated using precision diamond machining technology to achieving state-of-the-art feature sizes, surface accuracy, and optical performance.

Chapter 8 summaries the technological developments of both the microscopic, low cost high performance miniature objectives, and macroscopic, real-time snapshot hyperspectral endoscope, portions of the Bi-FOV endoscope. Future work and directions for the continued development of the Bi-FOV endoscope are also discussed.

2. BACKGROUND

Cancer is the second leading cause of death in the United States and will affect nearly half of all Americans in their lifetime [Ries 2008]. Success of treatment has been shown to have a strong correlation to the stage at which the disease has been first detected. Unfortunately most people are diagnosed at later stages (III or IV) where treatments are less effective, expensive, and more invasive [Lingen 08]. The goal of my research is to further advance optical imaging technologies for pre-and early cancer detection primarily for remote tissue sites such as the esophagus and/or colon. In the following sections I will review current research in optical imaging technologies for the screening and detection of pre- and early cancer.

2.1. Optical Imaging Technologies

Numerous optical imaging techniques for early cancer screening and detection have been developed over the last decade. Most of the technologies developed to date, have been either of the macroscopic or microscopic type. Microscopic techniques can obtain sub-cellular level information but have a small field of view (< 1 mm). Many of these techniques have been reported to have good correlation to histology for various types of early cancers [Collier 2007, Meining 2007]. Although, these results are encouraging, implementation of *in vivo* microscopy as a stand-a-lone screening tool seems impractical due to the long and tedious procedure that would be required to survey an entire organ site for potentially cancerous tissue. Macroscopic techniques on the other hand have the potential to provide quicker screening times since they have a larger field of view (> 1mm). However, the main limitation of macroscopic techniques is that they typically have lower levels of specificity than microscopic approaches [Wilson 2007]. Due to these complementary attributes there has been a growing interest in combining both macroscopic and microscopic systems into a single endoscope to enhance the detection of pre- and early staged cancer.

2.2. Current Trends in Microscopic Imaging

Microscopy remains the gold standard for evaluation and characterization of cancer. The physiological changes in tissue organization, cellular size, shape, and nucleus are all visual indicators of the progression and stage of cancer. Cancer diagnosis is typically performed by a pathologist in a lab examining a tissue biopsy removed from the patient under a high performance bench top optical microscope. There are several limitations with this approach for diagnosis such as biopsy sampling error, unnecessary patient trauma, and delayed results during examination to name a few. The current trend in optical microscopy has been to translate some of these well established techniques and processes from *ex vivo* to *in vivo* applications in the hopes that real-time non-invasive "optical biopsies" will overcome many of these limitations. *In vivo* microscopes (called endomicroscopes) have demonstrated the ability to provide the necessary morphologic and molecular features needed for determination of pre- and early cancer [Liang 2001, Rouse 2002, Udovich 2007, Kano 2004, Flusberg 2005, Hsiung 2008]. Figure 2.1 shows images recently obtained by Hsiung et. al. for identifying colonic adenoma from normal mucosa *in vivo* using a commercial fluorescence confocal endomicroscope (Cellvizio-GI, Mauna Kea Technologies). In Fig. 2.1(a) Hsiung has identified a suspicious lesion using white light endoscopy. The endomicroscope was then used to obtain confocal microscopic images of the polyp and surrounding regions Fig. 2.1(b)-(d) which are able to differentiate between normal and dysplastic crypts demonstrating the usefulness and added cancer detection capability of an *in vivo* microscopic system.

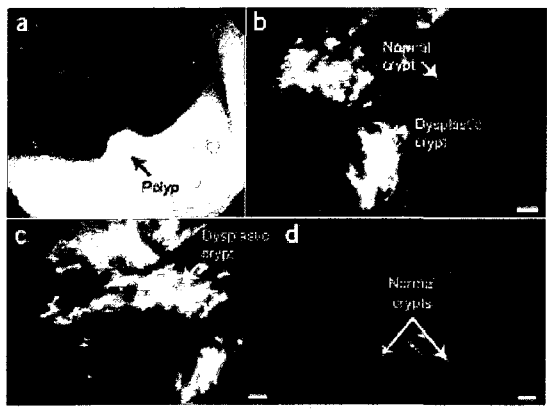

Fig 2.1- In vivo confocal fluorescence images of the border between colonic adenoma and normal mucosa (a) Endoscopic (b) Border (c)

Dysplastic crypt. (d)Adjacent mucosa. Scale bar, 20 microns [Hsiung 2008].

To further improve upon these *in vivo* microscopes research groups are developing new micro-fabrication technologies and approaches to make them smaller, less expensive, with better imaging performance. Most of this work has taken place in the distal end (tissue side) of the systems. Confocal endomicroscopes now incorporate miniature MEMS based actuators in the distal end of fiber optic probes for improvement of the final image resolution [Seibel 2006, Shin 2007, Ra 2007, and Miyajima 2004]. Most *in vivo* microscopes rely on fiber optics to transfer the imaging capabilities inside of the body, however limitations in their imaging performance due to fiber pixilation, back reflections, cross talk and bulky scanning mechanisms have lead some groups to pursue "fiber-less" approaches. These techniques attempt to miniaturize the entire optical device (optics, camera, light source, and mechanics) into a self contained system that can fit inside of the body as demonstrated by Rogers et al. [Rogers 2008] for a multi-modal miniature microscope as well as some slightly larger hand-held microscopes [Loewke 2008, Warger 2007] for more accessible tissue sites such as the oral cavity. The one common feature of all of these systems is the use of a high-performance miniature objective lens for illuminating and imaging the tissue site of interest. The need to miniaturize these high performance systems has however come at an expensive price. Research grade and other low volume devices often cost in the range of $8-$25K per unit and are still relatively expensive parts, in higher volumes often constituting a substantial fraction of the entire system cost. The reason for this expense is twofold. First, the optical and optomechanical components must be very precise to achieve diffraction limited imaging performance. Second, the optical components must be assembled and aligned within tight tolerances, which often requires highly trained personnel and precision alignment equipment to provide constant feedback throughout the whole process. Even as component volumes increase, the cost of these devices still remain relatively high due to the labor-intensive assembly process. This remains a big challenge for the continued development of endomicroscopy and its wide spread use. Another challenge for these endomicroscopes is their usefulness as a screening and/or diagnostic tool for pre- and early cancer detection since their field of view (FOV) is

small (< 1 mm). Some commercial companies such as Mauna Kea Technologies, are exploring software techniques such as image stitching to superficially increase the FOV of these systems [Osdoit 2006 & 2007], however, the tissue area must still be tediously scanned by the clinician.

2.3. Trends in Macroscopic Optical Imaging

A growing trend in macroscopic imaging techniques for early and pre-cancer detection has been to enhance their diagnostic capabilities by improving the spectral content of their images. Spectroscopy techniques have demonstrated that endogenous cancer bio-markers such as NADH, FAD, collagen, and oxy- and deoxy-hemoglobin have distinct fluorescence and reflectance based spectral signatures [Drezek 2001, Wu 2007, Zonios 1999]. These molecular bio-markers may serve as important indicators in identifying pre- and early cancerous regions to more traditional morphologic and architectural features. Researchers are now actively pursuing new ways to incorporate this spectral information into standard white light imaging systems. One such technique is autofluorescence imaging which utilizes the natural, endogenous fluorescence of tissue for identification of cancerous regions. Several groups have shown improvement in the detection of various types of pre-cancers using autofluorescence alone and/or in combination with white light endoscopy [Lane 2006]. In the colon, Wilson et. al. demonstrated that autofluorescence imaging improved their ability to differentiate premalignant (ademomatous) from benign (hyperplastic) polyps from 58% to 81% [Zanati]. Figure 2.2 shows an example of how spectrally enhanced imaging can enhance the detection of cancer over white light imaging. In Figure 2.2(A) the white light image appears normal for Barrett's Esophagus; however, under autofluorescence imaging (Figure 2.2(B)) the abnormal autofluorescence signature from the cancerous region is detected and false colored purple on the display screen for the clinician to quickly identify and biopsy for further diagnosis. Narrow band imaging has also shown tremendous potential has a viable pre-cancer detection technique. Narrow band imaging uses a spectral reflectance imaging technique to enhance mucosal morphology and microvascular patterns in tissue. Research groups have used narrow band imaging with white light to detect high-grade dysplasia in Barrett's Esophagus patients with high sensitivities in the range of 94-

100% and specificities ranging from 74-98% [Sharma 2006 Kara 2006]. Recently, a tri-modal imaging system combining narrow band imaging, autofluorescence, and high resolution white light imaging into a single endoscope maintained high sensitivities (>90%) while improving the false positive rate by 55% over just a bi-modal system using autofluorescence and white light imaging [Curvers 2008]. However, in this study 3 patients went undetected with the tri-modal system but were later discovered to have high grade dysplasia through random biopsies. In light of this work, researchers are now actively pursuing hyper-spectral imaging techniques in hopes that further improvement in spectral resolution will translate to even better pre- and early stage cancer detection.

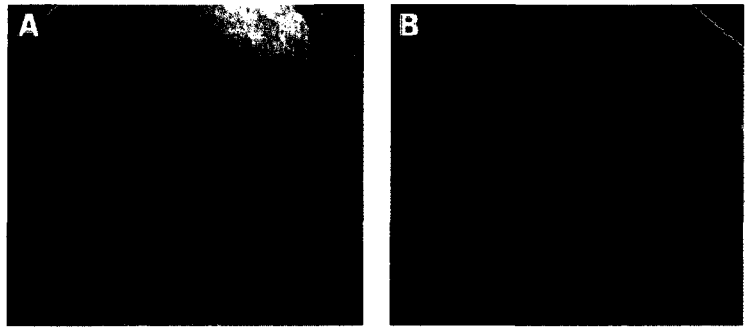

Figure 2.2- Images of Barretts Esophagus with histologically verified adenocarcinoma (A) under white light endoscopy the tissue appears normal. (B) Under Autofluorescence imaging a small purplish area is seen at the 1 o-clock position [Curvers 08].

Several hyperspectral techniques have been proposed, but drawbacks have limited their use as affordable, real-time screening tools. The main limitation of these approaches has been their reliance on scanning techniques which can only capture a fraction of the full datacube at a time and therefore cannot be real-time without sacrificing other important imaging parameters such as signal-to-noise ratio (S/N). For example, expensive tunable filters such as liquid crystal or acousto-optic, have been used to acquire the increased spectral bandwidth [Vo Dinh 2004, Gebhart 2007, Martin 2006 , Roblyer 2009, Pan & Tromberg 2004]. However, not only are these filters prohibitively expensive, but also delay imaging acquisition times (>23 secs) due to the serial fashion in which the spectral data is collected.

Recently, several new snapshot hyperspectral imaging approaches have been developed which have the potential to overcome the challenges of scanning based techniques by acquiring the entire 3D (x, y, λ) datacube simultaneously. These techniques include aperture splitting [Mathews 2008], field sampling [Matsuoka 2002, Bodkin 2006], computed tomography imaging spectrometry (CTIS) [Ford 2001], and coded aperture snapshot spectral imaging (CASSI) [Gehm 2007, Wagadarikar 2009]. To date only aperture splitting and field sampling techniques have been shown to acquire and display the 3D (x, y, λ) datacube in real-time which is one of the main requirements for *in vivo* imaging. However, these techniques have other limitations. Aperture splitting has reduced optical throughput and resolution because it divides the numerical aperture from each object point by the same number of spectral channels. Field sampling sacrifices spatial for spectral resolution by under sampling the object plane in a discrete fashion or compromises optical throughput by sampling only a portion of the light from each point in the image. Therefore, while techniques that enable simultaneous acquisition of the 3D (x, y, λ) datacube are desirable for real-time imaging, the reduction in performance of the other imaging parameters has limited their usability for many *in vivo* applications.

Following the current trends in cancer diagnostic research two technologies have been identifying for further develoment toward the ultimate goal of a Bi-FOV endoscope. The first technology is focused on developing low cost, high performance miniature optics which can be used at the distal end of the Bi-FOV endoscope. Develoment of this technology will enable the future integration of both widefield and high resolution imaging modalities within a small endoscope capable package without compromising performance. The second technology to be developed is a real-time snapshot hyperspectral imaging system which can be used to explore the benefits of enhanced spectral detection for widefield endoscopic imaging. Both of these technologies are currently not available for implementation into the Bi-FOV endoscope and represent significant contributions toward the biomedical community.

3. HIGH NUMERICAL APERTURE ENDOMICROSCOPE OBJECTIVE FOR A FIBER CONFOCAL REFLECTANCE MICROSCOPE[a]

[a]The contents of this chapter have been published in the following journal articles: R. T. Kester, T. S. Tkaczyk, M. R. Descour, T. Christenson, and R. Richards-Kortum, "High numerical aperture microendoscope objective for a fiber confocal reflectance microscope," Opt. Express 15, 2409-2420 (2007).

This chapter presents the beginning of my work toward the development of low cost, high performance miniature optics for endomicroscopy. Described below is the first generation of miniature high performance optics that I developed. A prototype objective was designed, fabricated, and tested for an *in vivo* fiber confocal reflectance microscopy (FCRM) system, although the technology can also be adapted for other imaging modalities. The objective is one of the first to achieve near diffraction limited imaging performance, integration of critical system components (i.e. hydraulic suction lines and unlatching mechanism), miniature endoscopy compatible size, and low component costs. To achieve these goals the objective incorporates a novel optical design approach combining off-the-shelf glass lenses and high volume plastic injection molding lenses. In addition, the objective uses high precision LIGA fabricated components to integrate imaging components with hydraulic suction lines into a common housing which has never been done before. The final objective measures only 3.85 mm in outer diameter and 14.65 mm in length. The device is diffraction limited for λ = 850 nm, has a numerical aperture of 1.0, a field of view of 250 μm, and a working distance of 450 μm. The one drawback of this design approach however was the long and complex assembly process needed to construct the objective which takes up to 8 hrs. This long assembly is addressed in the next chapter (chapter 4) with the second generation of miniature high performance optics.

3.1. Introduction

This chapter presents the development of a high numerical (NA) aperture diffraction limited endomicroscope objective that is part of a fiber confocal reflectance microscope (FCRM) system [Liang 2001]. Previous miniature objectives have been designed for this system to work with a probe that has a

10 mm outside diameter (O.D.), which includes an image bundle (Sumitomo IGN-15/30) that has a 2.5 mm O.D. and two hydraulic suction lines that measure 0.3 mm O.D. The intended use of the original system is for *in vivo* imaging of oral and cervical precancers where probes of this size are appropriate. However, to extend the ability of the FCRM system to image the interior of hollow organs such as the colon or urinary bladder, the maximum probe O.D. must be equal to or less than 4 mm, which would make it compatible with current endoscopy probes. The objective presented in this paper meets this criteria with an outer diameter of 3.85 mm and length of 14.65 mm (object plane to end of fiber ferrule) without sacrificing optical performance of the original design (see table 3.1).

In addition to miniaturization, cost is also an important factor in the objective design. Disposable components are often desired in the medical community because it eliminates the need for repeated sterilization procedures. Since the only part of the fiber confocal microscope that comes in contact with the tissue is the objective, there is strong motivation to make this component disposable. Typical endomicroscope objectives are not disposable since they require precise miniature optics that are expensive and difficult to align. A disposable high-NA miniature objective has been developed in our group by using only plastic injection molded optics and optomechanical features [Chidley 2002 & 2006]. This miniaturized objective had an O.D. of 8 mm, which was acceptable for imaging oral and cervical regions; however, it exceeds the size required for endoscopic imaging (< 4mm). To meet this new size limitation and disposability requirement, a hybrid approach was proposed that combines both plastic injection-molded optics and glass optics. The final design utilizes inexpensive components with one off-the-shelf glass element, two plastic injection-molded elements, and LIGA fabricated optomechanics, which are all easily mass producible. We believe this is the first endomicroscope objective for fiber confocal reflectance microscopy that offers high performance at a low cost.

3.2. Fiber confocal reflectance microscope system overview

The FCRM is a reflectance based microscope that is currently used to detect precancerous lesions by confocal imaging in the oral cavity and in the cervix. The FCRM is a point scanning, epi-illumination

system in which monochromatic light is focused to a point and then raster scanned across a coherent fiber bundle composed of 30,000 individual fibers. At the distal end of the bundle, each fiber is imaged to a specific location on the tissue by a miniature objective. In the presence of an index mismatch between the nucleus and the cytoplasm of an abnormal cell, light is reflected back through the system. This index mismatch is roughly $\Delta n = 0.05$ which translates to 0.034% of incident flux reflected, but can be increase to $\Delta n = 0.07$ with acetic acid solution [Sung 2002]. A beamsplitter redirects the reflected signal toward an avalanche photodiode (APD) which collects the reflected light converting it to an electrical signal for image acquisition and processing. To obtain images in 3D, hydraulic suction lines are used to translate different tissue layers through the focus region as it is being raster scanned in the lateral direction.

The low reflected signal from the tissue requires a design which optimizes the signal-to-noise ratio (SNR). A large contribution to noise comes from reflections off the fiber bundle surfaces since they are conjugate to the object plane. To reduce these reflections, both surfaces are immersed in an index matching oil. The objective elements must be AR coated and designed to minimize the irradiance from back reflections at the fiber bundle surface. In addition to reducing the background noise, the system is designed with a large NA objective to maximize collection of the reflected signal. A number of groups are also developing contrast agents to boost the reflected signal from abnormal cells [El Sayed 2005, Huang 2006, Loo 2005, Lin 2005, Sokolov 2003]. A more detailed description of the FCRM can be found in previous papers [Liang 2001, Sung 2002].

3.3. Optical Design

3.3.1.Design requirements

The design requirements for the new endomicroscope objective are similar to previous designs [Liang 2001, Chidley 2006] as it is intended to work with the same FCRM system described in the section above. The main difference in design specification is size constraint of the objective. For endoscopy applications, the O.D. of the probe cannot exceed 4 mm. Therefore, the optics, optomechanics, and hydraulics, which are necessary for imaging at multiple depths, must now be integrated into one small package. In addition,

the design wavelength has been changed from 1064 nm to 850 nm for use with metallic nanoparticle contrast agents. Table 3.1 lists all the design specifications.

Table 3.1. Design Specifications for Third Generation Objective.

Specification	**Value**
NA at object/tissue	1.0 (n_{water} = 1.33)
NA at image/fiber	0.3 (n_{oil} = 1.48)
Working distance	450 μm
Field of view (diameter)	250 μm
Telecentric	Object and image space
Object plane sag	≤5 μm (size of 1 cell)
Wavelength	1064nm (old) to 850 nm (new)
Outer Diameter (OD)	≤4 mm (new)

3.3.2.Design process

For this objective, it is imperative that the optics be miniaturized as much as possible to allow room for the optomechanical and hydraulic features that must reside within the reduced 4mm O.D. To determine if this is a realistic goal, the theoretical limit for the optics clear aperture was examined for a doubly telecentric system. Equations (1) and (2) are used to predict the minimum diameter for both object and image space [Liang(2) 2002].

$$Minimum\_Diameter_{object} = fullFOV + 2\tan\left[\sin^{-1}\left(\frac{NA_{obj}}{n_{obj}}\right)\right]WD \quad (1)$$

$$Minimum\_Diameter_{image} = fullFOV|m| + 2\tan\left[\sin^{-1}\left(\frac{NA_{img}}{n_{img}}\right)\right]z' \quad (2)$$

Where WD is the working distance, m is the objective magnification, NA is the numerical aperture, and z' is the image distance measured from the last optical surface. Inserting the design requirements from table 1 into equations (1) and (2) yields a diameter of 1.28 mm. The clear aperture does not need to remain at this theoretical limit, since that would over constrain the design preventing the necessary freedom for aberration correction but this limit does indicate that a solution is possible within a 4 mm diameter. The largest minimum diameter of 1.28 mm is from the object side where the rays are expanding at the fastest rate due to the high numerical aperture. For miniaturization, the highest power elements should be placed closest to these rapidly expanding rays to constrict them early in the design, resulting in the smallest

possible system clear aperture diameter. Attempts to miniaturize systems using only plastic optics have been unsuccessful due to low refractive indices, i.e., $n_{plastic}$~1.5 of plastics. Glass optics have much higher refractive indices of up to n_{glass}~ 2.0, but are expensive for high precision miniature elements. In an attempt to keep the cost of the objective low while maintaining a small OD, it was decided that an off-the-shelf high index glass element would be used. Typically off-the-shelf optics cannot be used for miniature high NA objectives since the latter require tight tolerances. However, by using an innovative lens mounting feature, as discussed later in the paper, the loose lens tolerances can be mitigated to an acceptable level. Since most of the power resides in the glass element, plastic injection-molded aspheric elements can be used primarily for aberration correction.

3.3.3.Final design form

The final design is a three element objective with a clear aperture diameter of 2.75mm. The design meets all of the criteria described in Table 3.1. The first element in the objective is a standard 2 mm diameter plano convex lens (Edmund Optics P/N: R45-955). The last two elements are custom plastic aspheric lenses. The lenses are made out of ZEONEX 480R plastic. Manufacturing issues were addressed in the design with consultation from a local plastic injection-molding company, Aurora Optical Inc., who also produced the initial prototypes of the plastic lenses. Fig. 3.1 illustrates a two dimensional layout of the lens system and Table 3-2 lists the lens prescription.

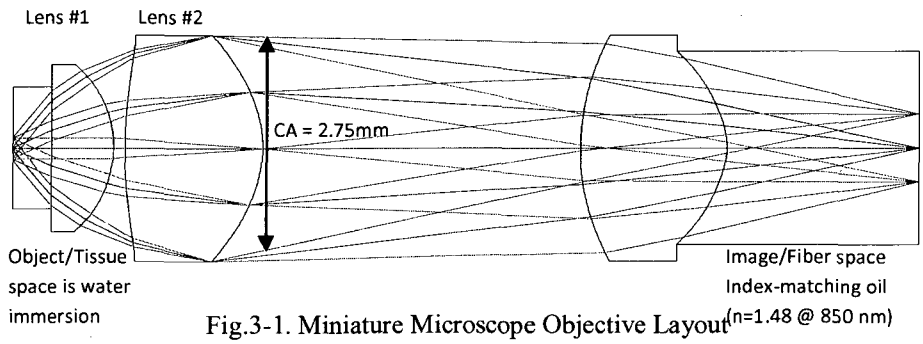

Fig.3-1. Miniature Microscope Objective Layout

Table 3.2. Miniature Microscope Objective Lens Prescription

Surf	Comment	Radius	Thickness	Glass	CA
OBJ*	TISSUE	1.500	0.504	SEAWATER	0.25
1	1st LENS	Infinity	0.800	LASFN9	1.48

2		-1.280	0.141		2.03
3*	2nd LENS	4.098	1.785	480R	2.58
STOP*		-1.433	4.105		2.75
5*	3rd LENS	2.646	1.893	480R	2.75
6*		-0.816	2.474	OIL (n=1.48)	2.35
IMA	FIBER	Infinity			0.83

*Aspheric Surface

Surf	Conic	4th	6th	8th
OBJ		27.954	-1185.370	
3		-0.0398	0.0132	
STOP	-1.016		-6.165E-4	9.553E-4
5	1.340		-6.913E-3	-1.497E-3
6	-3.636		-0.136	0.054

The optical performance of the design is shown in Fig. 3.2. The design is diffraction limited over the entire field of view for λ = 850 nm as shown in the spot diagrams in Fig. 3.2(a) and the MTF plots in Fig. 3.2(c). Fig. 3.2(b) displays the percent of distortion versus the field position (y-axis). The maximum distortion is approximately 0.25% or 1.5 microns at the 0.707 field position. This error is acceptable since it is smaller than the 7 micron fiber-to-fiber spacing within the fiber bundle and individual fiber displacement error of +/- 2 microns [Liang 2002].

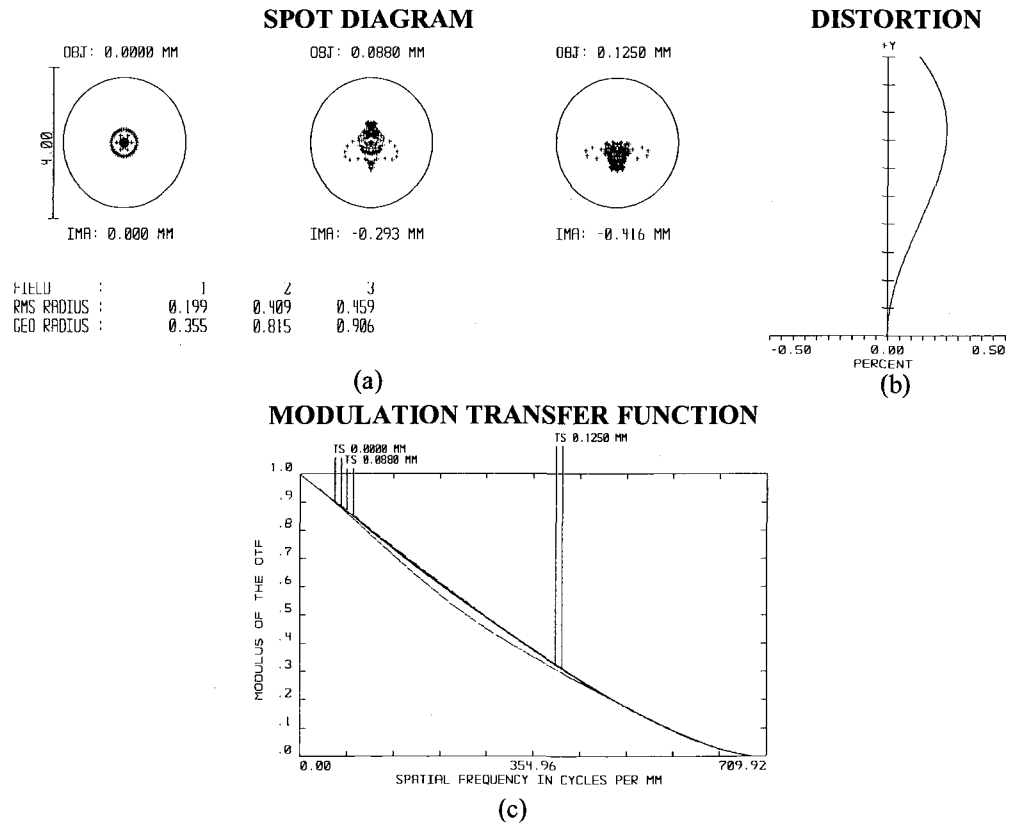

Fig. 3.2. Theoretical performance of the endomicroscope objective. (a) Geometric spot diagrams for three radial image positions: on-axis, 0.707 field, and full field. (b) Distortion plot in

percentage of deviation from chief ray location. (c) Modulation transfer function plot for the same image field positions in (a).

3.3.4. Tolerance analysis

A tolerance analysis was performed to predict fabrication success for the final design. Tolerances for the glass element are specified in the Edmund Optics catalog and displayed in table. Tolerances for the plastic optics are specified by the plastic injection-molder, and are also listed in Table 3.3.

Table 3.3. Tolerances for miniature optics in endomicroscope objective.

Description	**Glass**	**Plastic**
Radius	1%	0.5%
Thickness (mm)	±0.05	±0.020
Diameter (mm)	+0.0/-0.05	±0.020
Surface Irreg.	NA	<2 fringes
Surface Decenter (mm)	(see below text)	±0.025
Surface tilt	(see below text)	±0.15 deg
Index tolerances	0.001	0.001

Decentration of the first lens (glass) is eliminated with the optomechanics (see section 3.6), and is not specified in Table 3.3. Surface tilt for a plano-convex spherical element can also be considered as decentration, and likewise, is also not specified. Element decentration is assumed to be ±3 microns.

The tolerance analysis used a Monte Carlo (MC) simulation that statistically adjusts design parameters outlined in Table 3.3 using a normal distribution, and then evaluates the performance of the system based on the RMS spot size. Compensation parameters are the object position, image position, and object shape. Object shape is allowed to vary due to the object sectioning capability of the system. The acceptance criteria is that fifty percent (50%) of the Monte Carlo simulations must have a RMS spot size equal to or less than the diffraction limited Airy disk spot size. Table 3.4 lists the proportion of Monte Carlo simulations which result in an RMS spot size smaller than a threshold value.

Table 3.4. Monte Carlo tolerance results for objective.

Pop.	**RMS Spot Size**
90% ≤	5.62 μm
50% ≤	3.86 μm
10% ≤	2.18 μm

50% of the MC simulations resulted in an RMS spot size less than or equal to 3.86 microns which is close enough to the Airy disk spot size of 3.46 microns that it is acceptable, especially when comparing these sizes to the diameter of the individual fibers (~4 microns) which couple the light at the objectives image plane back through the system.

3.3.5.Ghost reflection analysis

As mentioned previously, the reflected signal from abnormal cells is ~ 0.034% of the incident flux. The reflected signal is so small it is imperative that back reflections in the objective be reduced to minimum levels. Optical surfaces are coated with an anti-reflection (AR) coating to decrease reflections from 4-5% to 0.25% of the incident flux, except for the surface which contacts the index matching fluid where AR coating is not needed. Even with AR coatings, the back reflections are still an order of magnitude larger than the reflected signal from tissue. If a back reflection comes to focus near the image plane, its irradiance level is comparable to the object signal, increasing the need for increased dynamic range of the detector. Spot sizes at image plane are analyzed using ZEMAX Ghost Focus Generator [ZEMAX]. Irradiance values are computed assuming uniform flux density across the field of view. In cases where reflected rays are vignetted, throughput is estimated by ratioing solid angles. Fig. 3.3 shows the reflected light rays from some of the surfaces. Table 3.5 lists the irradiance contributions from each surface.

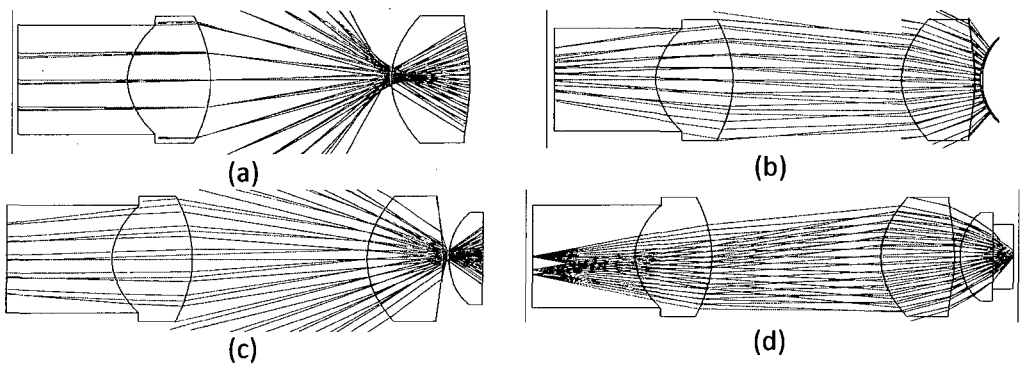

Fig. 3.3. Schematic of back reflections from some of the surfaces in objective. (a) surface 3, (b) surface 2, (c) surface 1, (d) tissue.

Table 3.5. Back reflection irradiance comparison to signal irradiance.

Surface	E (W/m^2)

1 (c)	9E0
2 (b)	4E2
3 (a)	3E1
4	3E1
5	2E3
6	2E2
Tissue (d)	3E7

The irradiance level from the tissue to the fiber bundle location is 4 orders of magnitude (~ 10^4) larger than that from the other surfaces. From this analysis it is evident that back reflections will have a minimal impact on the system performance.

3.3.6.Optomechanical design

The optomechanical design needs to have high precision, small feature size, low cost, and ease of assembly. Traditionally machined, molded, or stamped parts are limited in feature size and precision but offer high throughput and low cost depending on complexity of design. Other processes, such as electro-discharge machining (EDM), produce parts with high precision and small feature size, but are expensive and low volume. An alternative to these approaches are LIGA fabricated components [The MEMS HANDBOOK 2006]. LIGA is a German acronym, for X-ray lithography (X-ray Lithographie), Electroplating (Galvanoformung), and Molding (Abformung)). The process offers high precision (sub micron dimensional control), repeatable processing based on lithography, and low cost due to high throughput from batch or parallel fabrication. Feature sizes range from millimeter to sub-millimeter dimensions [The MEMS HANDBOOK 2006]. The use of LIGA fabricated parts also allows for easy implementation of complex miniaturized geometries without additional component cost. These attributes make LIGA fabricated components ideal for this application. The process does have limitations in that the surface shapes must be vertical in nature, and typical surface layers do not exceed 500 microns in thickness. However, with proper design these limitations can be overcome.

The final optomechanical design for the miniature microscope objective is shown in Fig. 3.4. The elements in the drawing are all to scale. Ray tracing through the objective illustrates the object and image locations and the optical element clear apertures. The housing is composed of a series of layers made of nickel. Most layers are 500 microns in thickness and have dimensional tolerances of +/- 2 microns. The

disadvantage of using this stacking approach is that the individual layer tolerances in the axial direction increase by the number of layers between the elements. Fortunately, the optical system is less sensitive in this direction and can tolerate this error. The lateral tolerances are the critical parameters which are still held. As the layers are stacked, the possibility that the location of each layer can shift giving a "Tower of Pisa" effect is possible. However, with this design the tightest tolerances are associated with the first two elements which are near the distal tip of the objective mitigating this concern. The advantage of using this stacking approach is that the design becomes very modular. Layers can be easily added or removed without having to redesign the optomechanics. The layers are intended to be diffusion bonded/soldered to one another providing a rigid watertight objective.

The tissue (object) is located in the bottom right corner of Fig. 3.4 and is immersed in saline solution. The saline solution is delivered by the hydraulic channels located in an isolated ring between the optics and outer diameter of the objective. The ring is split into two crescent shaped channels by two through pins used for alignment during assembly (see Fig. 3.5(a)). The channels converge at the object chamber. One channel is used for suctioning and the other is used for filling and removing bubbles from the chamber. Each hydraulic channel connects to a standard silicone or PTFE tube at the end of the objective. The hydraulics are used to move tissue through the objective focal plane for 3D imaging. In addition to providing 3D sectioning, the hydraulic channels can also be used for delivery of contrast agents or for marking areas of tissue with dye for later analysis.

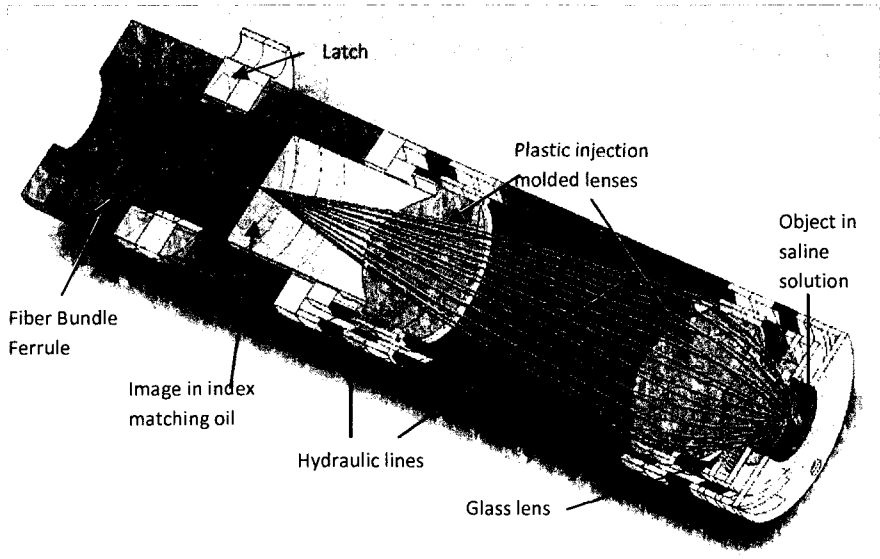

Fig. 3.4. Optomechanical assembly schematic of endomicroscope objective.

The distal tip of the fiber bundle is attached to a ferrule that fits into the objective at the rear. The objective includes a latch to lock the fiber bundle in optimum position for imaging. The latch is a bi-stable spring, which locks in both an outward and inner position. Fig. 3.7 shows a sequence of pictures where the fiber bundle is inserted into the objective and then locked in place.

The plastic injection-molded optics is held in proper position by a mechanical flange molded into the lens that centers on a rim located in the housing. A retaining ring is used to secure the optic in place from the back side. The glass element is positioned in the objective using a self centering ring. The ring actively engages the lens surface flexing away as it makes contact, while centering the lens with respect to its optical axis as shown in Fig. 3.5. This retaining ring eliminates any decentration associated with off-the-shelf lens manufacturing error.

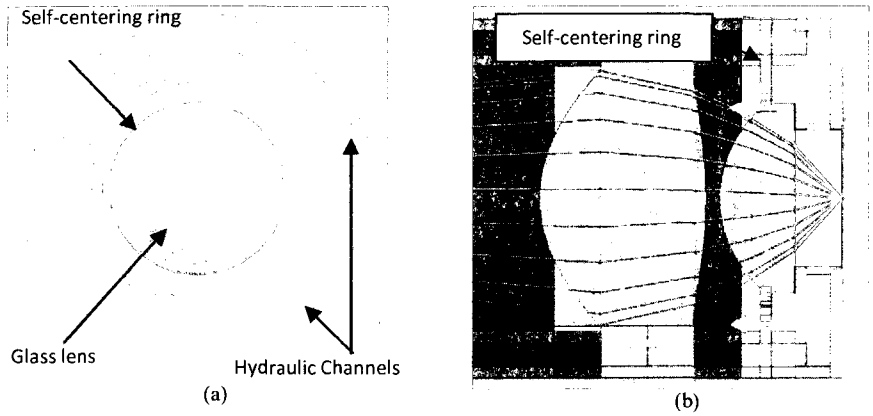

Fig. 3.5. LIGA manufactured self-centering ring for glass element in objective. (a) Front view of self-centering ring. (b) Side view of self-centering ring showing the flexing direction of ring.

3.4. Assembly/Testing

3.4.1. Assembly

For prototyping purposes, the plastic optics were diamond turned instead of injection molded. Diamond turning a soft material like Zone 480R, is difficult, and leaves tool marks across the surface. White light profilometry measured an rms roughness of ~ ½ wave and an average peak-to-valley of ~ 3 waves. For initial performance testing this surface is acceptable, however, the performance will be slightly degraded. The lenses were also not anti-reflection (AR) coated. The objective is assembled using a vertical stacking approach in which two precision through pins hold alignment as the layers are slid into place. The optics are added to the objective as it is being assembled. The LIGA components are secured in place using UV curable epoxy. The epoxy is applied to the outside wall of the objective after the layers are pressed together, and does not add to the thickness of the objective. In the future, layers of the objectives will be diffusion/solder bonded together making it water tight for use with hydraulics. The fiber bundle ferrule is assembled in the same manner as the objective. Fig. 3.6(a) shows some individual components used in the objective assembly. Fig. 3.6(b) is a picture of the complete endomicroscope objective. Both pictures are taken with a U.S. penny to show its relative size.

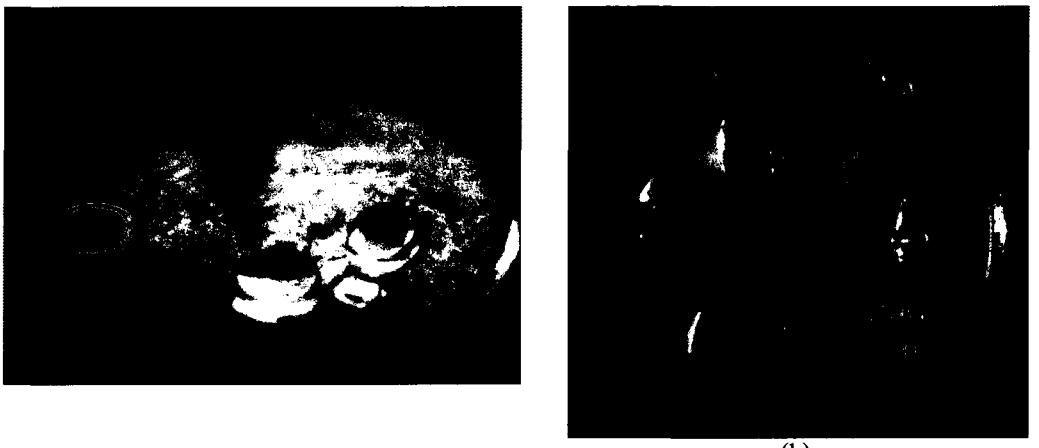

(a) (b)

Fig. 3.6. Pictures of actual endomicroscope objective and components. (a) Some components used in the objective (lenses, objective layers, and ferrule). (b) Assembled endomicroscope objective.

Since the objective is intended to be a disposable component of the FCRM system, it is important that its integration with the system is easy and simple. The next sequence of pictures demonstrate the seamless mating of the objective with the fiber bundle ferrule. Once the bundle is fully inserted into the objective, the operator pushes down on the latch handle, 'snapping' the latch spring into its inner locking position. The two pieces are securely held together until the operator lifts the latch handle up, at which time, the latch spring 'snaps' back to its unlocked position. The fiber bundle ferrule can now slide freely from the objective for disposal. The objective is designed with a ferrule stop that prevents the fiber bundle from damaging the objective lens or itself during insertion and removal.

Fig. 3.7. Sequence of pictures showing the integration of the fiber bundle with objective.

3.4.2.Testing

The objective was tested on a modified optical bench test setup described in detail in M. Chidley's paper [Chidley 2006]. The source was changed from a 1064 nm Nd:YAG laser (Amoco 1064-50P) to an 850 nm IR LED (LEDtronics L200CWIR851). The spinning diffusers in the test setup were also eliminated, since the LED source is inherently incoherent. The objective is tested in trans-illumination. The test targets are placed in an immersion oil bath at the objective's image location and uniformly illuminated from behind. The objective images the target to the water immersed object location. A water immersion IR objective (Olympus UM575) with matching NA (NA=1.0 WI) and a tube lens (f=120mm doublet) relays the image onto a CCD camera (Pulnix TM-745E) for analysis. Two methods were used for evaluating the optical performance of the objective. A simple first test involves imaging a standard 1951 United States Air Force (USAF) Resolution target. The target contains groups of vertical and horizontal bars with known spatial frequencies. The highest resolved spatial frequency roughly indicates the resolving capability of the system. The test is only meant to provide a quick evaluation of performance since it is susceptible to human error. Fig. 3.8(a) shows the objective resolving the smallest elements on the resolution chart, the Group 7 element 6 bars, which correspond to a spatial frequency of 228 line pairs per millimeter (LPMM). This spatial frequency corresponds to a resolution of 760 LPMM at the tissue or 1.3 microns (object plane). The FCRM's lateral resolution is limited by the fiber-to-fiber spacing of the fiber-optic bundle and not the objective's lateral resolution. The fiber-to-fiber spacing is ~ 7 microns (71 LPMM) in image space, or ~ 2.1 microns (238 LPMM) in object space. The axial resolution of the system is estimated to be ~ 2 microns [Olympus]. The second more quantitative test used to evaluate the optical performance of the objective is the slanted-edge technique [Burns 2000]. MTF results are extracted from an image of a slanted edge using data processing. Images are taken at two corners, the upper right and lower left, of a square box. Since MTF results are only valid for the axis perpendicular to the edge, both a horizontal and vertical edge were analyzed to better evaluate the objective performance. Fig. 3.8(b) shows the location of two images taken from the upper right corner.

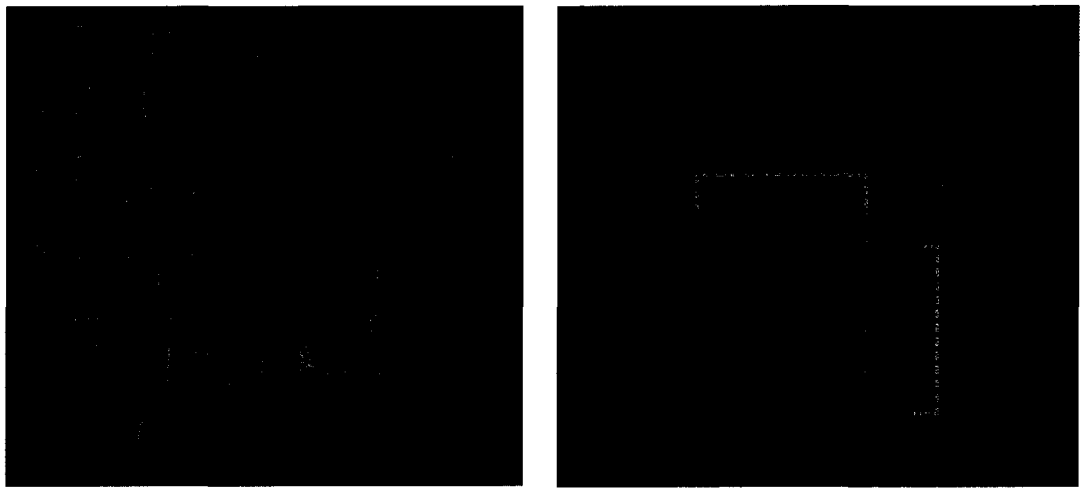

Fig. 3.8. Optical performance results for endomicroscope objective. (a) USAF resolution target imaged by objective. (b) Slanted-edge data acquisition locations for upper right corner.

The MTF results (in image space) are shown in Fig. 3.9. Each curve corresponds to the vertical and horizontal edges of the square. The average Strehl ratio (SR) for the entire system is 0.61 at 850 nm. The Strehl Ratio (SR) compares the peak irradiance in the measured Airy disk to that of the theoretical Airy disk providing a convenient single value measure, ranging from 0 (poor) to 1 (best), of system image quality. Improving the optical surface quality by injection molding the plastic lenses instead of diamond turning should increase this result. The objective was tested in transmission instead of reflection to reduce the effect of back reflections since the optics were not AR coated.

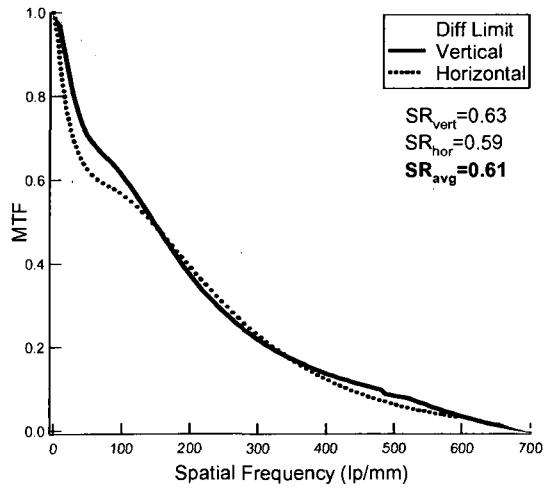

Fig. 3.9. MTF and SR performance for endomicroscope object at four edges of a square.

3.5. Conclusion

A miniature microscope objective has been designed, fabricated, and tested, for use in endoscopy applications. The objective integrates both imaging and hydraulic capabilities into a package whose size is only 3.85 mm outside diameter and 14.68 mm in length. The objective has a water immersion NA = 1.0 for maximum light collection at the tissue surface. Testing the prototype showed a Strehl ratio of 0.61 at the design wavelength of 850 nm. The objective components are inexpensive ~ $35 creating the interesting prospect for disposable use with a fiber confocal reflectance microscope. Future development is in process to fully implement and test the hydraulic capabilities of the objective . In addition, efforts to reduce the long assembly time are still required to fully realize the disposable aspects of this technology.

Acknowledgements

This research was supported by the National Cancer Institute under grants R01 EB002179 titled, "Fiber Optic In Vivo Confocal Microscopy," and R01 CA103830 titled, "Optical Systems for In Vivo Molecular Imaging of Cancer." The author would also like to thank Aurora Optical Inc. for use of their facilities.

4. Low Cost, High Performance, Self Aligning Miniature Optical Systems[a]

[a]The contents of this chapter have been published in the following journal article: R. T. Kester, T. Christenson, R. Richards Kortum, and T. S. Tkaczyk, "Low cost, high performance, self-aligning miniature optical systems," Appl. Opt. **48**, 3375-3384 (2009).

The most expensive aspects in producing high quality miniature optical systems are the component costs and long assembly process. For the first generation objective design descibed in chapter 3 the component costs were low compared to conventional technologies, however the assembly process was long taking up to 8 hrs. This chapter presents the development of a second generation of miniature optics technology which reduces both aspects through the implementation of self aligning LIGA optomechanics with high volume plastic injection molded and off-the-shelf glass optics. This zero alignment strategy has been incorporated into a miniature high numerical aperture (NA=1.0W) microscope objective. Tight alignment tolerances of less than 10 microns are maintained for all components which reside inside of a small 9 gauge diameter hypodermic tubing. A prototype system has been tested using the slanted edge MTF technique and demonstrated to have a Strehl ratio of 0.71. This universal technology is now being developed for smaller, needle-sized imaging systems and other portable point-of-care diagnostic instruments.

4.1. Introduction

Current advances in optical diagnostics and biomedical imaging have promoted numerous applications that require miniature, high-performance optical imaging systems. These applications include endoscope-compatible *in vivo* microscopes such as confocal reflectance and fluorescence [Liang 2001, Sung 2002, Rouse 2005], structured illumination [Rogers 2008], and multi- and two photon [Gobel 2004, Bao 2008, Levene 2004] systems. There is also growing interest in applying miniature optics for portable point-of-care diagnostics [Christodoulides 2005], and needle sized optical biopsy systems [Li 2000]. The need to miniaturize these high performance systems has come at an expensive price. Research grade and other low volume devices often cost in the range of $8-$25K per unit and are still

relatively expensive parts, in higher volumes often constituting a substantial fraction of the entire system cost. The reason for this expense is twofold. First, the optical and optomechanical components must be very precise to achieve diffraction limited imaging performance. Second, the optical components must be assembled and aligned within tight tolerances, which often requires highly trained personnel and precision alignment equipment to provide constant feedback throughout the whole process. Even as component volumes increase, the cost of these devices still remain relatively high due to the labor-intensive assembly process. The solution to this problem is to create self-centering optical components, where no additional adjustments and/or alignment are necessary. We propose such a zero-alignment design that incorporates precision self-aligning optomechanics fabricated using LIGA (German acronym **Li**thographie, **G**alvanoformung, **Ab**formung) technology with high volume plastic injection molded lenses and off-the-shelf glass lenses. This approach simplifies assembly, accommodates lower tolerance components, and eliminates the need for additional adjustments.

4.2. Optical Design

As a proof-of-concept, a new self-aligning miniature microscope objective was designed for use with a fiber confocal reflectance microscope (FCRM) already under development in our lab. This device was chosen for several reasons. First, the FCRM's primary application, *in vivo* tissue imaging, requires a high NA due to the low reflected signal (around 0.034% of the incident light onto the tissue) and the need to increase sampling of the fibers within the microscope's fiber bundle. Consequently, as the NA of the objective increases, the optical and optomechanical tolerances become tighter placing more stringent demands on the self-aligning design. If this approach works for these high NA systems, it should therefore also work for lower NA systems. Second, since the objective comes in contact with the patient it is more desirable for this component to be disposable which requires a cost-effective design that does not sacrifice optical performance. A summary of all of the design requirements for the miniature microscope objective is listed in Table 4.1.

Table 4.1. Miniature microscope objective top level optical design requirements

Optical Requirements	**Requirement**
NA at object/tissue	1.0 (n_{water} = 1.33)
NA at image/fiber	0.35
Working distance	≥450 μm
Field of view (diameter)	250 μm
Telecentric	Object/Image space
Object plane sag	≤5 μm (size of 1 cell)
Wavelength	808 nm
Outer Diameter (OD)	≤4 mm (new)
RMS Wavefront Distortion	≤.07λ

The final optical design for the miniature objective is shown in Fig. 4.1 along with the lens prescription in Table 4.2. The design was optimized and evaluated using lens design software ZEMAX [ZEMAX] to achieve diffraction limited performance. This design is cost effective being comprised of only 3 lenses, an off-the-shelf glass lens (Edmund Optics M43-396), and two custom plastic injection molded lenses. The design strategy was to have the off-the-shelf glass lens provide most of the optical power in the system, while the custom aspheric plastic lenses are used for optical aberration correction. This approach is inexpensive and also assists in the miniaturization of the objective since the light rays from the object (tissue) are constricted early in the system and not allowed to expand further outward as they propagate to the image (fiber optic bundle). It should be noted that, unlike conventional microscope objectives, this objective has a curved object surface to assist in aberration correction. This is permitted since the objective will be used with a fiber confocal reflectance microscope which has tissue sectioning capabilities. While the object plane is curved, the image plane must still remain flat for optimum coupling to the fiber bundle. The objective is also corrected for an anti-reflection coated coverslip which will be attached to the fiber optic bundle at the image plane. The main purpose of the coverslip is to remove unwanted back reflections from the system without compromising coupling efficiency from an angled polished surface. For this paper we primarily concentrate on the development of a general approach for assembly of a class of high NA optical systems and their expected performance. Therefore the objective is tested without the fiber bundle which limits system resolution (resolution of the FCRM is fiber bundle limited).

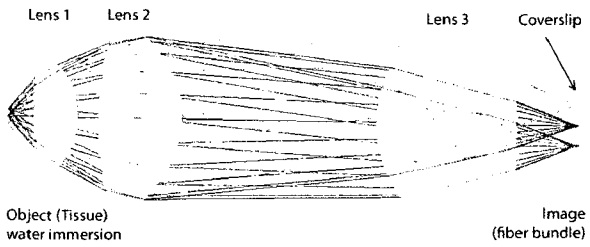

Fig. 4.1. Optical design layout of miniature microscope objective.

Table 4.2. Lens Prescription for Miniature Objective Optical Design.

Surf	Comment	Radius	Thickness	Glass	CA
OBJ*	TISSUE	1.494	0.459	SEAWATER	0.25
1	1st LENS	Infinity	0.800	LASFN9	1.37
2		-1.280	0.354		1.96
3*	2nd LENS	3.632	1.500	E48R	2.76
STOP*		-1.491	3.443		2.80
5*	3rd LENS	2.019	2.500	E48R	2.80
6		Infinity	0.967		1.68
7	COVERSLIP	Infinity	0.15	BK7	0.84
IMA		Infinity			0.71

*Aspheric Surface

Surf	Conic	4th	6th	8th
OBJ		30.1012	-1244.083	
3		-0.0400	0.01136	-1.590E-3
STOP	-1.02369		-1.219E-3	1.092E-3
5	-0.15485		-4.137E-3	5.818E-4

The performance metrics for this optical design are shown in Fig. 4.2. Figure 4.2(a) contains a plot of the modulation transfer function for the system (image side) at 3 field locations, on-axis (0 field), 100 microns (0.707 field), and 125 microns (full field). Figure 4.2 (b) includes plots of the field curvature and distortion. The field curvature is well corrected for both saggital and tangential planes at the image plane. The maximum distortion in the system is 1% which is acceptable for most users and can also be corrected in software if needed. Figure 4.2(c) displays geometrical spot diagrams for the on-axis, 0.707 field, and full field image points. The spots are within the circumscribing Airy disc (black circle), indicating diffraction limited performance.

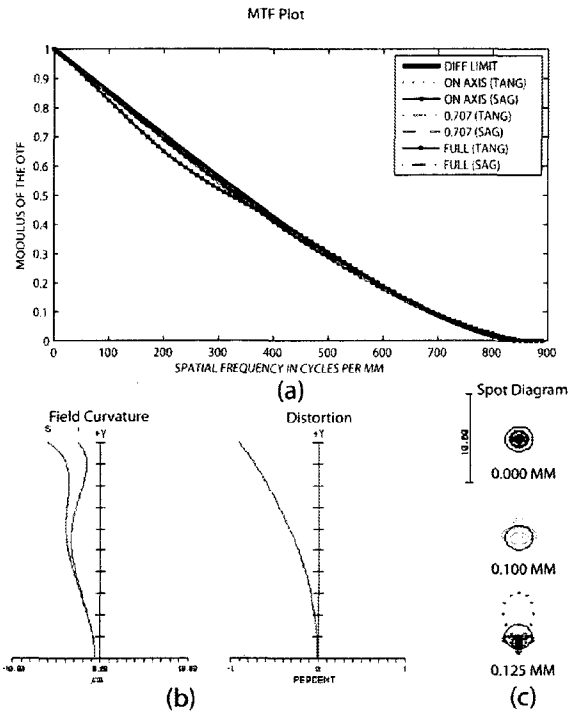

Fig. 4.2. Optical design performance of the NA = 1.0(water immersion) miniature objective. (a) Modulation transfer function for 3 field locations, on-axis, 0.707 field, and full field. (b) Field curvature for sagittal and tangential planes. (c) Spot diagrams for same 3 field locations in MTF with diffraction limited Airy disk.

A thorough tolerance sensitivity analysis was performed on the design to translate the optical performance requirements into optomechanical design requirements. The optical performance metric used was that the RMS wavefront error (RMS WFE) must be $\leq .07\lambda$. This metric requirement is a common and accepted criteria used for diffraction limited systems [Wetherall 1980]. The individual optomechanical tolerances were added together using the root sum of squares method (RSS) to estimate the overall system level error. The allocation of the tolerances with associated sensitivities is shown in Table 4.3.

Table 4.3. Optomechanical Tolerances and Tolerance Sensitivities Analysis.

Parameter	Nom. (mm)	Tol (mm)	rms WFE (λ)	Sen. (λ/mm)
Lens 1				
S2	1.28	0.020	0.002	0.10
Thick	0.8	0.050	0.044	0.88
Space(L1-L2)	0.354	0.020	0.020	1.00
Lens 2				
S1*	3.632	0.020	0.004	0.20
S2*	1.491	0.010	0.010	**1.00 (3)**
Thick	1.5	0.020	0.018	0.90
Tilt (elem)	0	0.010	0.017	**1.67 (2)**
Dec (elem)	0	0.008	0.037	**4.67 (1)**
Space(L2-L3)	3.443	0.020	0.012	0.62
Lens 3				
S1*	2.019	0.010	0.010	1.00
thick	2.5	0.020	0.005	0.24
Tilt (elem)	0	0.010	0.002	0.22
Dec (elem)	0	0.010	0.005	0.50
Space(L3-ima)	0.967	0.020	0.013	0.65
RSS rms WFE			**0.070**	

The total expected system RMS WFE is 0.070λ which meets the specification. In tolerancing the design, Lens 1 is fixed in place and all other errors are with respect to its position. In addition, component fabrication errors such as surface decentration and tilt present in the plastic lenses (Lens 2 & 3) are not considered as they are compensated for by the optomechanics and will be translated to element decentration and tilt. In principle this compensation is accomplished during the assembly of the objective. The mechanical mounts (Fig. 4.3) engage the spherical or slightly aspheric surfaces on both sides of the lens. When an axial force is applied, the lens surfaces slide on the mechanical mount's circular edge until completely seated. In this manner, the mechanical mount's central axis and the lens element's optical axis become aligned with each other. Therefore, the main system tolerance errors can be reduced to the following parameters: element position, surface radius, and element thickness. The optomechanical design focuses on minimizing these errors in order to obtain diffraction limited performance.

4.3. Optomechanical Design

The primary fabrication technology used in the optomechanics is LIGA (German acronym **Li**thographie, **G**alvanoformung, **A**bformung) which is a lithographic based set of processes capable of producing very precise, miniature, and inexpensive mechanical devices and components [Madou 2002]. LIGA fabricated components are an excellent technology for optomechanics since they have precise dimensional tolerances at the micron level for both lateral and axial dimensions and can be reliably mass produced. The technology also allows for miniature features not possible with traditional manufacturing techniques. Note, however, that LIGA components are limited to only vertically etched geometries. The biggest drawback to using these components for optomechanics is that the thickest layers are typically only 500 microns, while most miniature optical systems are several millimeters in length. To overcome this limitation we previously used a "vertical stacking" technique whereby sequential layers are stacked on top of each other and held in place using two gauge pins that run the length of the objective housing [Kester 2007]. However, this approach involved the use of many layers (27) and led to a long, tedious assembly process which offset the advantage of the low component cost. The approach proposed here assumed the need for realization of both low component cost and reduced assembly time, without sacrificing image quality, and lead to the new self-aligning optomechanical design concept.

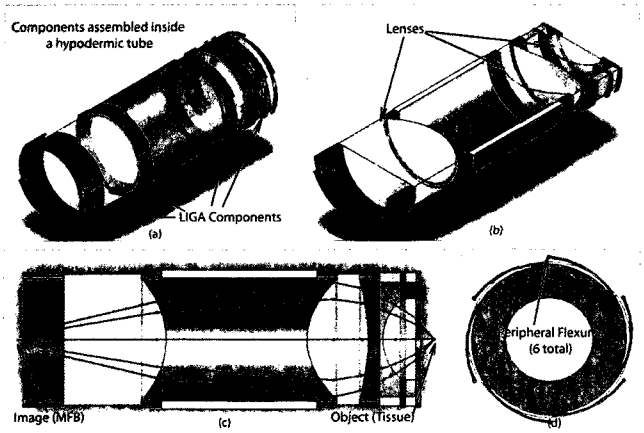

Fig. 4.3. Drawing of the self-aligning concept as applied to this miniature objective. (a) Isometric view of critical objective components

with lens barrel suppressed. (b) Sliced isometric view with lens components labeled. (c) Sliced side view of objective with actual light rays refracting through system from an on-axis field point. (d) Front view showing the 6 self centering flexures on the periphery of the LIGA optomechanics.

The self-aligning optomechanical design is shown in Fig. 4.3. The design and fabrication was developed in collaboration with HTmicro Inc., who has extensive experience in developing other miniature optomechanical components with our lab [Rogers 2008, Kester 2007]. In this approach, high precision LIGA mechanical layers are used to interface between the miniature lens barrel (Hypodermic tubing, Small Parts Inc., P/N: HTX-09X) and the optical lens elements with a smaller hypodermic tube (Small Parts Inc., P/N: HTX-10X) used as a spacer between lens 2 and 3. As discussed earlier, the layers provide a uniform circular edge contact with the lens surfaces and help align the optical axis of the lens element with the mechanical axis of the LIGA layer. The LIGA layers are aligned to the mechanical axis of the lens barrel (hypodermic tubing) through the use of 6 flexures integrated into the periphery of the part. These flexures compensate for any inner diameter variations of the lens barrel, while still maintaining alignment with the mechanical axis of the tube. The flexures were modeled (Fig. 4.4) as simple cantilevers to balance the internal stress of the flexure with the necessary force to align the optical components. The model assumed friction was the only movement inhibitor for the lens. The cantilever stress and force equation used in the design is described by (1) and (2):

$$F = \frac{\delta 3EI}{l^3} \qquad (1),$$

$$\sigma = \frac{Flh}{2I} \qquad (2).$$

F is resistance force to the flexure displacement, E is Young's Modulus, l, h, and b are the dimensional parameters, and I is defined as $I=1/12*bh^3$. The Young's modulus, E, for the flexure material (Ni Alloy) is 160 GPA and the maximum stress for this material is 1000-1050 MPa. The hypodermic tubing has an inner diameter (I.D.) range of 3.378-3.480 mm. The flexures can accommodate this I.D.

variation with a flexible range of 3.331-3.517 mm. They are also designed to be in constant contact with the I.D. of the tubing with the flexures extending past the I.D. of the tubing by a minimum of 37 microns. Therefore, when the flexures are inserted into the tubing there is at least 37 microns of inward displacement of the flexures pushing on the tubing. The minimum preload force due to this displacement corresponds to 42 mN. This force is sufficient to center Lens 1 (similar for other lenses) where only approximately 0.2 mN are required to overcome the frictional forces holding the lenses in place. The frictional force from Lens 1 is calculated using the relationship $F_f=\mu F_n$ where F_f is the friction force, μ is the coefficient of friction (nickel-glass interface is ~0.5), and F_n is the normal force due to gravity. The mass of the lens used for calculating the normal force is 3.2 x 10^{-5} kg (estimated from ZEMAX modeling software). It should be noted that there is a large safety factor of 200X applied to these calculations to take into account any errors due to the simplified cantilever model as well as other unknown parameters. Lastly, when the flexures undergo maximum compression due to a hypodermic tubing inner diameter of 3.331 mm the internal stress induced in the flexure reaches 300 MPa which must be kept below the maximum stress requirement previously stated. By satisfying the conditions imposed in equations 1 and 2 we are able to fine tune the flexures to provide sufficient self-aligning capabilities under all expected manufacturing tolerances while maintaining their integrity.

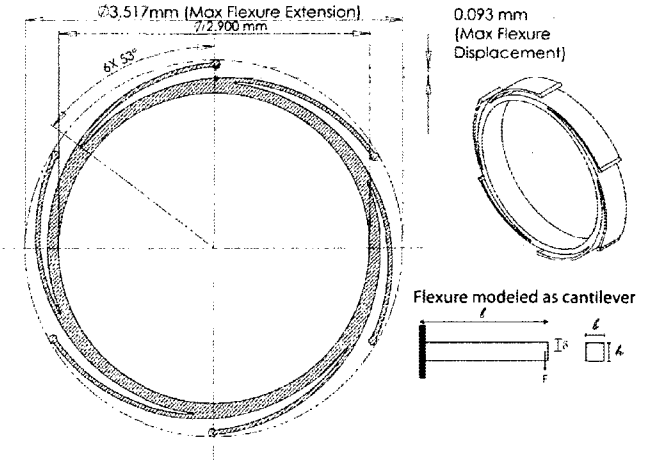

Fig. 4.4. Diagram of flexure design and analysis. Flexures where modeled as simple cantilevers to balance the force and stress equations.

The final aspect that will be discussed is the assembly process for the objective components. The assembly approach is sequential in nature starting with the object side components and finishing with the image side components, although the order can be reversed. The tubing is mounted in a fixture with one end secured to a flat metal surface and the other end open for component insertion. The parts are manually inserted into the tubing and then slid into place with the help of a precise gauge pin (Deltronic P/N: PPM25 3.4300mm). The gauge pin is held perpendicular and concentric to the mechanical axis of the tubing with the help of a watchmaker's staking toolset. Once all components are inside of the lens barrel, the ends are glued in place using Norland 61 UV curable epoxy and the objective is tested. Note that this manual procedure was used for prototyping only while for production batch-automatic assembly is envisioned.

4.4. Component Evaluation

The critical components in the self centering design were dimensionally characterized to gain more insight into the system imaging performance and also helped to validate the experimental results. In the process of prototyping and characterizing these components unexpected challenges required modifications to the design which ultimately lead to a better performing system. For example, some of the first miniature LIGA fabricated components shown in Fig. 4.5 (a), next to a US nickel for size comparison, were highly reflective, being composed of a Ni alloy material. Large amounts of stray light reflecting off the optomechanics entered the image plane, thus decreasing image contrast in early prototype systems. An oxidization process was then developed to blacken these components which improved the image contrast in subsequent prototype systems. These black oxidized components are shown in Fig. 4.5 (b).

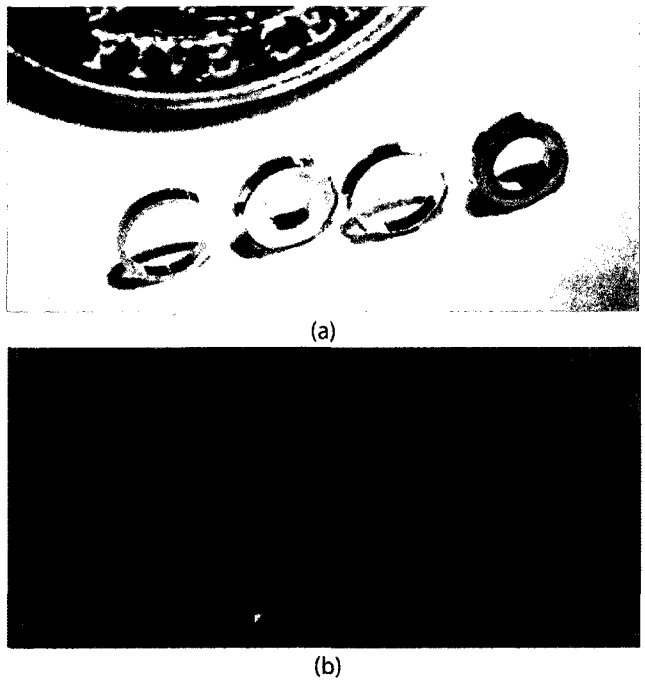

Fig 4.5. Pictures of prototype LIGA fabricated optomechanical components. (a) non-oxidized parts with high scattering. (b) black oxidized parts with low scattering.

A dimensional analysis of the LIGA components was performed using a Zygo NewView 5200 white light interferometer (WLI) to confirm the critical lateral and axial dimensions. The study evaluated 2 sets of 5 components. The first set was tested for lateral dimensions which included measurements of the flexure distance from the outer ring, flexure width, and inner-to-outer ring centration. These parts were measured in 6 locations equally spaced around the circumference of the part for a total of 30 measurements. The second set of components was measured for only thickness. The results from this study are shown in Table 4.4.

The lateral part dimensions are within the range needed for the optical design since they are under the 8-10 micron tolerance error budgeted in the tolerance analysis (Table 4.3). The thickness of the layers however is greater than expected with an error of 16.9 microns. Although this is above the expected axial tolerance, the system is less sensitive to axial position errors as shown by the low axial tolerance sensitivity range of 0.62-1.00 λ/mm depending on the optical space. Note also that this error

can be easily corrected by lapping LIGA wafers to the required thickness. In the most sensitive region (L1-L2 spacing) this additional thickness error would be around 13.8 microns using the root sum of squares (RSS) method. This effectively increases the WFE contribution from this tolerance by ~.01λ and also raises the expected system level RMS WFE to .08λ which is slightly above the criteria for diffraction limited performance. In the future, we expect the thickness tolerance of these layers to be within +/- 3 microns as the fabrication process is better optimized for this design.

Table 4.4. Lateral and axial measurements for critical features of the LIGA optomechanics taken with a white light interferometer.

Location	Dimensional Average Error (μm)	Error Standard Deviation (μm)
Flexure Width	+ 1.5	0.7
Flexure Distance	- 2.9	3.5
Inner to outer ring centration	1.1	0.2
Thickness	+16.9	13.7

Much of this design approach relies on the lens barrel (hypodermic tubing) providing a straight mechanical axis for aligning the optical components. In reality this tubing may have some "waviness" to it. To quantify the "waviness" of this tubing we used the WLI to collect surface profiles down the entire length of 5 hypodermic tubes cut to the length of our lens barrel as shown in Fig. 4.6. The surface profiles were taken on the outer diameter of the tubing with the assumption that any "waviness" observed will be similar inside of the tubing as well. The data was also filtered using a low pass FFT filter to remove surface roughness features less than the width of our thinnest LIGA layer (125 microns). The total scanned image length of 10 mm is a composition of 8 stitched images from a 20X objective with a FOV = 350 x 270 micron and lateral resolution = 1-2 microns. The results from this analysis are shown in Table 4.5. The average peak to valley (P-V) displacement from the best fit cylinder for all measurements was ~4 microns. This "waviness" of the hypodermic tubing is within the allowable tolerance for the high NA objective. When the lateral tolerance errors of the LIGA components and the 'waviness" of the tubing are added together using the RSS method the predicted

lateral error is 5.3 microns which is below the 8-10 microns required for diffraction limited performance.

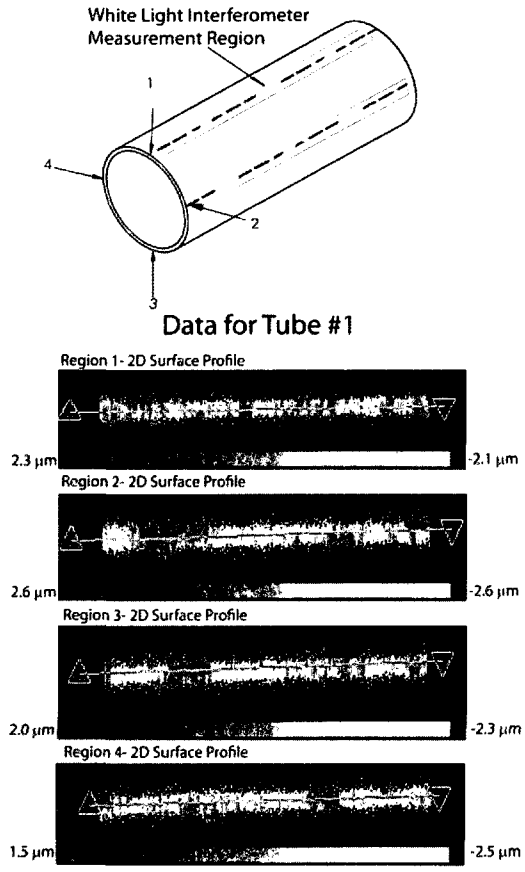

Fig. 4.6. Lens barrel (hypodermic tubing) waviness measurements measured with a white light interferometer around 4 full length regions of the tubing. Below are actual 2D surface profiles taken from Tube #1.

Table 4.5. Hypodermic tubing 'waviness' characterization results taken with a white light interferometer.

Tube #	Side1	Side 2	Side 3	Side 4	Tube Avg
1	4.3	5.2	4.3	4.0	4.5
2	2.9	3.9	4.8	3.4	3.8
3	3.4	4.3	3.9	3.2	3.7
4	3.2	3.2	3.4	2.7	3.1
5	4.5	3.2	3.0	4.8	3.9
Overall Average					**3.8**
Standard Deviation					**0.5**

*units in microns

Next, the interaction between the optomechanics and optics were examined. The first test explored the self-centering capability of the LIGA layers using a single optical component. For this test, Lens 1 and its associated optomechanics were used. A short hypodermic tubing (length = 3.5 mm) was cut to serve as the lens tube barrel. The optomechanical components and lens were placed inside the tubing and pressed in place using the gauge pin (Deltronic P/N: PPM25 3.4300mm) that is part of the assembly fixturing. The gauge pin presses the components against a microscope slide which is used as the base. The construct was then tested using the WLI. The WLI was configured to operate in 'stitching' mode to acquired 5 fields-of-view (4 on the LIGA layer, and 1- in the center of Lens 1) while keeping track of their relative positions. The individual FOV dimensions are 0.36 x 0.27 mm with a lateral resolution of 0.56 microns. A schematic of the test setup is shown at the top of Figure 4.7. Figure 4.7 (a) presents the raw 3D map of the apex of the lens shown as a red color indicating it is the highest surface (+173.55 microns) and the LIGA layer below this surface shown in blue color is the lowest surface (-131.26 microns). A 2D plot was then obtained (Figure 7 (b)) from the 3D map for both the x and y axis to find the center of the LIGA layer. The lens surface was then fit to the standard spherical surface equation:

$$(x-h)^2+(y-k)^2=r^2 \quad \textbf{(3)}$$

where h is the center of the surface in the x-axis, k is the center of the surface in the y-axis, and r is the radius of the surface, to find the center of the lens. For this measurement the center of the lens in the x-axis matches the center of the LIGA x-axis to within 0.2 microns. The test was repeated 3 times using the same lens but with different LIGA self-centering layers and found to have an average decentration of 7.2 +/- 2.8 microns. This initial result is encouraging since it is in the range of tolerances required for this design, however, more statistical data is still required to determine the robustness of this technique.

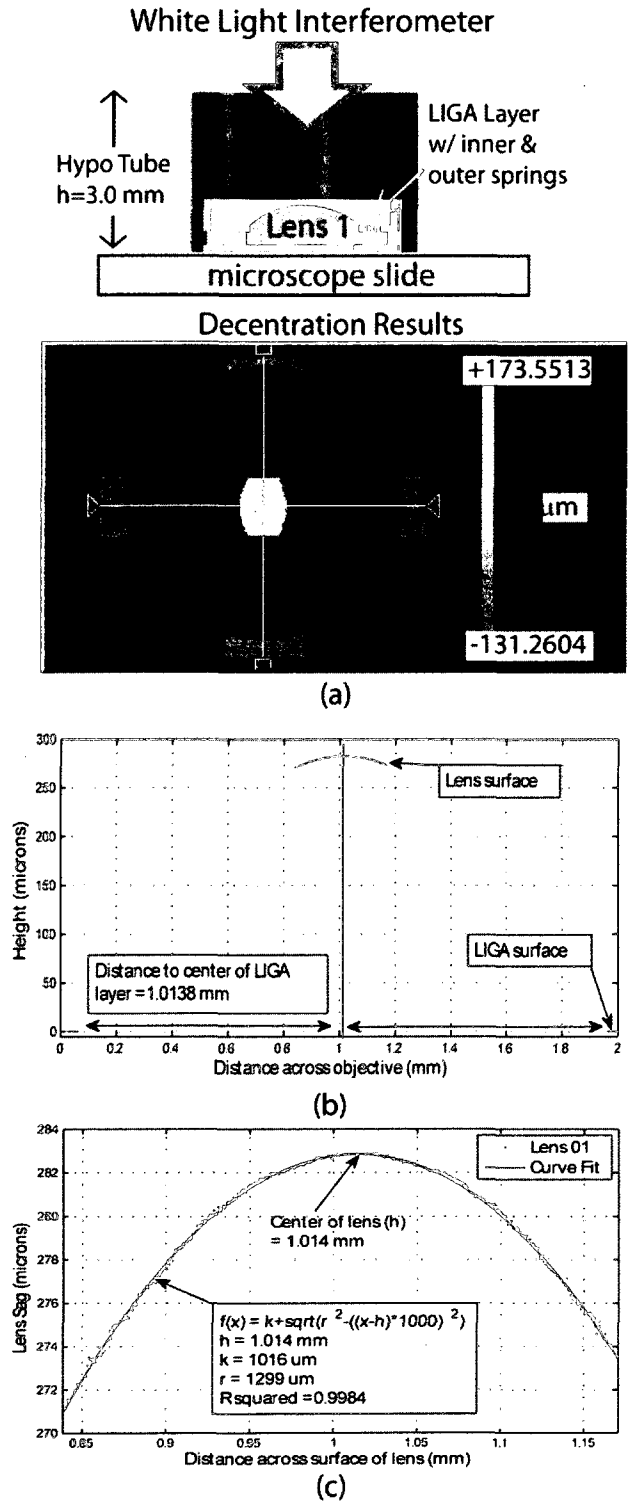

Fig. 4.7. Decentration test setup and initial results. (a) 3D map of the lens 1 and its LIGA layer tomography obtained by the WLI. (b) X-axis cross-section through lens and LIGA layer . (c) Curve fit results for the x-axis cross section of the lens apex used to find the lens center.

The element tilts for this design concept were also explored using a similar approach to the decentration analysis. The model used for this test is shown at the top of Figure 4.8 and consists of two Lens 3 elements and 5 LIGA layers (3 layers between the two lenses and one layer at both ends of the housing). A hypodermic tubing cut to a length of 6.5 mm is used to house all of the components. The components were inserted sequentially into the tubing and seated in place using the gauge pin. After assembly the model was tested using the WLI. First the tilt of the microscope slide was measured (see Figure 4.8 (1A & 1B)) and adjusted until it was sufficiently removed (<.05 microns over FOV 3.52 x 2.74 mm) from the base of the objective. Then, the WLI was re-positioned to the top of the objective and the tilt was measured for the flat surface of Lens 3 (see Figure 8 (2A & 2B)). The x and y tilt's were measured to be -1.71 mrad and -2.20 mrad respectively. The total magnitude of the tilt was calculated to be 2.8 mrad, which for a CA of 2.8mm corresponds to 7.84 microns. This result demonstrates that the element tilt is within the required tolerance specifications. However due to limited part(s) availability we were unable to study the effects of variations in the assembly procedure, components, users, etc., which still need to be explored in the future to obtain a more complete understanding of the design limitations and accuracy.

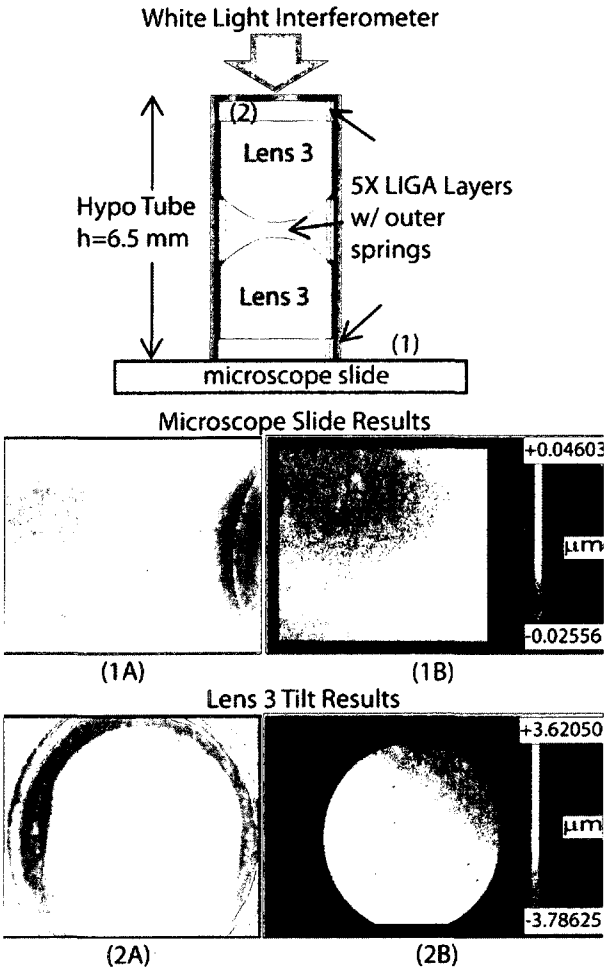

Fig. 4.8. Element tilt test setup and results. (1A) Grayscale image and (1B) WLI tomography results taken from region 1 (microscope slide). (2A) Grayscale image and (2B) WLI tomography results taken from region 2 (top of Lens 3) used to find tilt system components.

4.5. Optical Performance Results

For prototyping purposes the plastic injection molded lenses were manufactured on a diamond turning lathe by Syntec Optic Inc. to meet the required tolerances in Table 4.1. The RMS surface roughness for these lenses were slightly higher than we would expect from a mold and were measured, being on average 10 nm over a 350 X 270 micron region. Measurements were performed with the WLI. Initial prototype systems were assembled and tested using these lenses. Note that injection molded

components for NA = 1.0 microscope objectives were previously successfully presented as feasible [Chidley 2006, Liang 2002]. Fig. 4.9 shows two manufactured systems, one without and the other with a black oxidized coating, respectively.

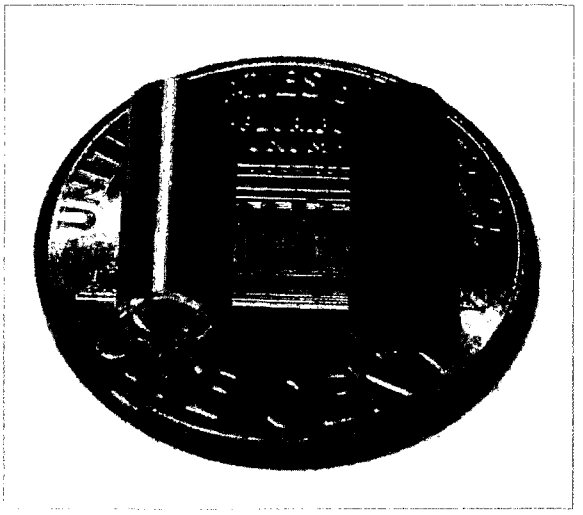

Fig. 4.9. Assembled miniature objective prototypes (oxidized and non-oxidized) on a US penny for size comparison.

The optical performance of the black oxidized objective was further evaluated using the slanted edge MTF technique [Burns 2000] as well as imaging a 1951 USAF resolution target. The test setup for these measurements is shown in Fig. 4.10. An IR LED (λp= 800 nm) and holographic diffuser are used to provide uniform incoherent illumination onto the target. To simplify the illumination system for testing purposes the objective was tested in reverse with the target being imaged from image to object space. This image is then relayed by a ZEISS Achroplan 63X NA=0.95 water immersion objective and tube lens onto a CCD camera. It should be noted that the objective was tested at a slightly lower NA than designed (NA=1.0). The smallest vertical and horizontal bars on the resolution target (Group 7 Element 6) corresponding to 256 line pairs per millimeter are resolved with this system as shown in Fig. 4.11 (a). However to better quantify the imaging performance of the miniature objective, a corner of one of these bars is imaged by the system (Fig. 4.11 (b)) and processed using the previously mentioned slanted edge technique to obtain an estimate of the MTF

curve for both the vertical and horizontal directions as well as an average MTF curve for both directions as shown in Fig. 4.11 (c). A useful single value metric for comparing optical imaging performance is known as the Strehl ratio (SR). It is the ratio of the area under the measured MTF curve (red) to the area under the ideal MTF curve (black) with 1 being the best and 0 being the worst. For this system the Strehl ratio is 0.71 which is a quite promising result since diffraction limited performance is maintained for SR's $\geq$0.8. Better image performance results are expected with tighter control of the optomechanical layer thickness and injection molding of the plastic lens elements (lower roughness of lens surface). The effect of the curved object plane on the overall performance of the system may also have contributed to the reduced image performance however it is difficult to quantify at this time.

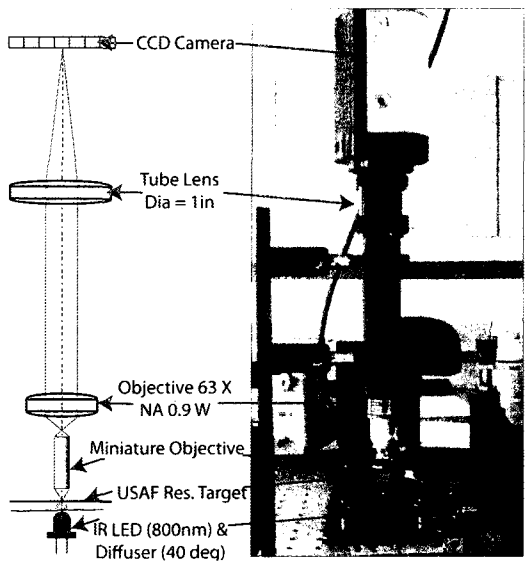

Fig. 4.10. Modulation Transfer Function (MTF) test setup for evaluation of prototype objective imaging performance.

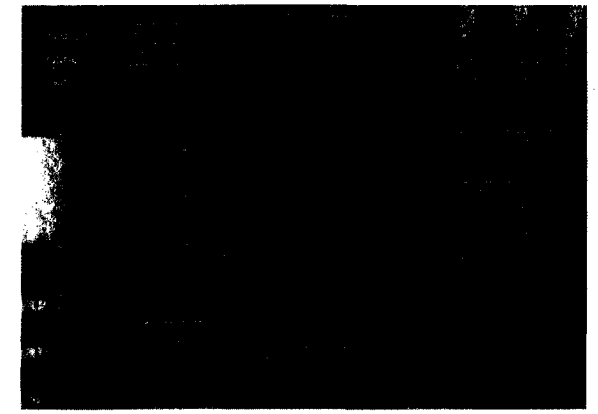

(a)

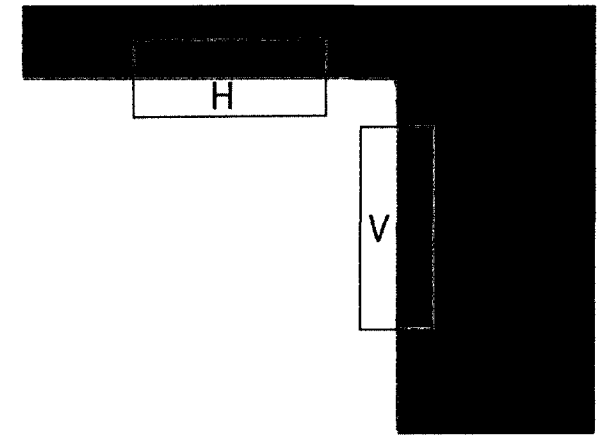

(b)

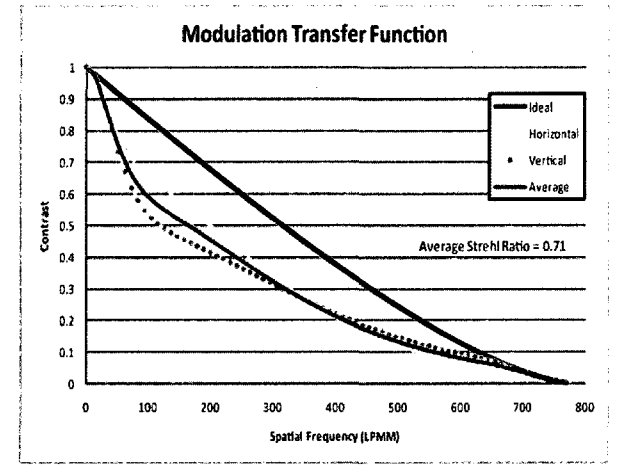

(c)

Fig. 4.11. Imaging results for the prototype objective. (a) Objective can resolve the USAF resolution target group 7 element 6 (256 lp/mm) bars. (b) Image of a corner on the resolution target is used for calculating MTF based on slanted-edge technique. (c) Objective MTF curves for horizontal and vertical edges (dash and dotted curves) shown with ideal MTF curve (solid black). The average for the horizontal and vertical edge is shown in red. The objective has an average SR of 0.71.

4.6. Conclusions

The design concept for creating inexpensive miniature optical systems through the use of self aligning LIGA optomechanics has been successfully proven through its implementation in a miniature high NA objective design for a fiber confocal reflectance microscope. A prototype objective was successfully assembled with no external precision alignment feedback. The optical performance of the objective was tested to have a Strehl Ratio of $SR = 0.71$. The estimated cost of this objective in volumes is in the range of $50-$200 although a more detailed cost analysis is needed to confirm these numbers. In comparison a standard microscope objective with similar FOV and NA will cost between $1,000-4,000. Custom miniature objectives based on more traditional fabrication techniques can cost upwards of $25K in some cases. This technology has the potential to greatly reduce the cost of miniature optical systems increasing their use in industrial and academic applications.

Acknowledgements

This research was supported by the National Cancer Institute under grants RO1 CA 124319 titled, "Integrated Bi-FOV Endoscope for Detection of Precancer," and R01 CA103830 title, "Optical Systems for In Vivo Molecular Imaging of Cancer." The author would also like to thank undergraduate students Syed Saad Ahsan at Cornell University, Ithaca, NY and Keith Michel at Rice University, Houston, TX for their help in assembly and testing of objectives.

5. IMAGING PERFORMANCE AND COST ASSESSMENT OF SELF-CENTERING MINIATURE OPTICAL SYSTEMS FOR MEDICAL DIAGNOSTICS[a]

[a]The contents of this chapter will be submitted in the following journal article: R. T. Kester, M.C. Pierce, J. Sun, R. Richards Kortum, and T. S. Tkaczyk, "Imaging performance and cost assessment of self-centering miniature optical systems for medical diagnostics," (To be submitted).

In chapter 4 the development of low cost, high performance miniature objectives are described offering the potential of disposable optics for endomicroscopy. In this chapter, a more detailed examination of the costs of these optical systems is presented and compared against other technologies. Factors such as quantity and fabrication technology are considered in addition to size and imaging performance. Biological images acquired with these objectives are also presented demonstrating for the first time their potential not only for endomicroscopy, but also for point-of-care diagnostics which is another exciting field where low cost, high performance miniature optics could greatly benefit industrical and academic applications.

5.1. Introduction

There is a growing need for low cost, high performance miniature optical systems for a variety of emerging medical applications particularly in the areas of endomicroscopy and point-of-care diagnostics. Endo-microscopy is an exciting emerging technology which can enable real-time, sub-cellular resolution imaging of tissue, *in situ*. The images provided can help clinicians diagnose and treat diseases such as cancer, while reducing pain and discomfort to patients caused by unnecessary surgical biopsies. Endo-microscopy techniques are also being used in fundamental research, enabling scientists to study multifaceted disease processes as they evolve *in situ*. Endo-microscopy encompasses several optical imaging modalities, including wide-field epi-fluorescence [Jung 2004], confocal fluorescence [Jean 2007, Tanbakuchi 2010, Rouse 2004] and reflectance [Liang 2002], and nonlinear microscopy [Wu 2009, Bao 2008, Piyawattanametha 2009, Barretto 2009]. A common feature of all of these systems is the use of a

high-performance miniature objective lens for illuminating and imaging the tissue site of interest. These objectives are not widely available through commercial vendors, and therefore require a custom design, fabrication, and assembly process which can be expensive and time consuming. In the area of optical based point-of-care diagnostics, low cost, high performance miniature optics are critical for providing portable, inexpensive, and accurate instrumentation. Several groups are working on developing the appropriate optical microfluidic technology for these applications [Myers 2008, Verpoorte 2003]; however, due to the limited supply of off-the-shelf miniature optical components, most of them must design an entirely custom solution which is very expensive and difficult to obtain.

We recently described a novel platform for the development of a high-performance miniature objective for endomicroscopy which significantly reduced the component cost and greatly simplified the assembly process, while maintaining high-quality imaging performance [Kester 2009]. The technology can also be applied to point-of-care instrumentation providing a more compact, portable microscope or array of microscopes for the detection and monitoring of a variety of diseases including HIV [Rouet 2005], tuberculosis[Park 2005], and enteric diseases [Yager 2006]. Here we present a detailed assessment of this technology by comparing the size, performance, and cost with similar miniature microscope objectives against those made by four alternative design and fabrication processes. As with other reported miniature microscope objectives [Jean 2007, Rouse 2004] our systems have a high NA (0.25-1.0), field-of-view of 200-500 μm, and an outer diameter of less than 10 mm. Figure 5.1 shows a miniature microscope objectives fabricated by each of the four different methodologies, alongside a conventional microscope objective [Liang 2002, Barretto 2009, Chidley 2006, Kester 2007].

Figure 5.1 - Evolution of miniature microscope objectives, alongside a US Quarter and Olympus objective with similar NA and FOV for size comparison. (a) Standard glass[Liang 2002], (b) Plastic injection molding[Chidley 2006], (c) Hybrid Glass/Plastic[Kester 2007], (d) & (e) Hybrid self-centering[Kester 2009].

5.2. Performance vs Size vs Cost analysis

As an optical system is scaled down in size, design tolerances typically tighten, which in turn push the limits of traditional fabrication and assembly technologies. High tolerances can certainly be achieved using these approaches, but come at a significant increase in cost. This trend is evident with the first objective lens shown in figure 5.1(a). This objective used standard glass grinding and polishing to fabricate the eight individual lenses in the system, which was then assembled with high-precision metal optomechanics into a brass housing of 10 mm diameter by 17.8 mm length [Liang 2002]. During the assembly process, the lenses were aligned by highly trained individuals using state-of-the-art alignment equipment which contributed to the final cost of the objective reaching $8,000. However, with a measured Strehl ratio (SR) over 0.9, the imaging performance of this system is diffraction-limited. At a diameter of 10 mm, this objective is still relatively large for many endoscopic applications, and to decrease this figure into the more versatile 3-5 mm range would increase costs to over $15,000 per unit.

To address some of these limitations, a second system was developed based on plastic injection-molding (figure 5.1(b)) [Chidley 2006], allowing individual components to be mass produced in high volume, significantly reducing the cost of each objective. A reduction in the total number of lens

elements required to produce a well-corrected objective was achieved through use of components with aspheric shaped surfaces. In addition, the physical size of this objective was reduced by integrating optomechanical positioning features into the individual lenses. The fabrication cost for this objective (in large volume) is estimated to be 30x lower than those involving traditional grinding and polishing methods in glass. The main drawback is that the overall size of the objective remains relatively large at a diameter and length of 8 mm and 14.5 mm respectively. In addition, the lack of variety in injection-moldable plastics with high refractive indices currently prohibits a further reduction in size with this method.

The objective shown in figure 5.1(c) [Kester 2007] is based on a hybrid glass/plastic optical design approach combined with a new MEMS fabrication technology termed LIGA [Madou 2002]. This approach simultaneously takes advantage of the high refractive indices available in glass, the ability to generate aspheric surfaces at low cost with plastic injection molding, and the development of high-precision / high-volume optomechanical positioning components with LIGA technology. The complete objective resides within the desired diameter range of 3-5 mm at only 3.8 mm and had a length of 10.4 mm. This approach also enables the objective assembly process to be greatly simplified, lowering this cost component which traditionally escalates rapidly with shrinking system dimensions. The solution was found by using the LIGA process to incorporate features into the optomechanics for self-aligning the components [Kester 2009]. A fourth objective, again using self-centering LIGA optomechanics with a hybrid glass/plastic optical design was created as shown in figure 5.1(d,e). Objective (e) includes a blackening oxidation process for reducing stray light within the system. The overall diameter of these objectives remains very small at 3.8 mm diameter by 10.4 mm length. This objective has excellent optical performance with a measured Strehl ratio of 0.75 [Kester 2009]. Table 5.1 summarizes the size and performance parameters of the different technology approaches used for the different endomicroscope objectives.

Table 5.1: Summary of the size versus performance for the different endomicroscope objective technologies.

System	OD	NA	FOV	SR
Glass	10 mm	1.0	250 μm	> 0.9
Plastic Injection molded	8.0 mm	1.0	250 μm	0.7 – 0.75
Hybrid Glass/ Plastic I	3.9 mm	1.0	250 μm	0.7 – 0.75
Self centering	3.9 mm	1.0	250 μm	0.7 – 0.75

5.3. Detailed Costs Analysis of Self-Centering Objective

The cost of fabricating this self-centering hybrid glass/plastic endomicroscope objective (fig. 5.1d,e) can be farther analyzed based upon the assumption of low- or high-volume production. This objective is composed of three lenses, eight LIGA optomechanical layers, and two precision-cut hypodermic tubes [Kester 2009]. The first lens in the design is an off-the-shelf glass lens (Edmund Optics M43-396), costing $28 each for quantities below 50, dropping to $6-$10 for quantities approaching 1000. At the prototyping stage, the second and third (plastic) lenses were diamond-turned directly at an approximate cost of $200 per lens, independent of volume. Once a design is finalized these lenses can be injection molded, requiring a master mold to be fabricated for a one-time cost of $20,000 - $50,000 (depending on the number of lens cavities). For these miniature (< 10 mm diameter) plastic lenses, the marginal cost of injection molding each lens is estimated at $1-2. For components that require anti-reflection (AR) coatings, the cost is in the range of $1,600 - $2,000 per coating run, which can accommodate up to 1,000 lenses, adding $1.60 - $2.00 / lens. The total cost for the optics in the objective is then $13-$18. Table 5.2 summarizes the price of the lenses in the self-centering objective along with the quantities.

Table 5.2 - Costs comparison of optics in endomicroscope objective for prototyping quantities and production quantities.

Description	Qty	Costs (Size < 50)	Costs (Size = 1000)
Glass lens	1	$28	$6-10
Plastic lens	2		
Diamond Turning		$200	--
Injection Molding*		--	$2
Coatings (two sides)	1	$32-$40	$1.6-$2
Total		**$492-$508**	**$13.2 - 18**

*Note: Requires initial investment of $20,000 - $50,000 for mold

The LIGA optomechanical components used in the objective require an initial investment in a mask which costs $2,000 for process I (a 2 in. x 3 in. mask) or $6,000 for process II (a 4 in. x 6 in. mask.) Although less expensive, process I can only produce about 300 components at a time, while process II can produce 1,200 which reduces the per part costs for larger volume production. The exposure and electroplating costs for process I is $2,000 and slightly higher for process II at $3,000. The fixturing to pick the parts up from the substrate is the same for both processes costing $1,000. The oxidation process to blacken the parts for reduced scattering within the objective is also the same for both processes adding an additional cost of $200. The total costs of either process and the costs per part is shown in table 5.3. For process I the cost is approximately. $30/part and for process II the cost is approximately $10 / part. The total cost for the optomechanics (8 components) is then $240 or $80 depending on volume.

Table 5.3- Costs comparison of LIGA optomechanics for endomicroscope objective for prototyping quantities and production quantities.

Process	Quantity produced	Final costs	Cost per component
1	300	$9,200	$30
2	1200	$12,200	$10

The spacer and housing material for this objective is standard hypodermic tubing cut to length using a precision diamond saw. The total cost of each tube is estimated at < $1. Assembly of the objective is assumed to add another $15 / objective for volumes below one thousand units. For volumes greater than a thousand units, a batch assembly fixture is assumed which would lower the costs to under $5 per objective. Based on these estimations, a cost summary for the self-centering hybrid glass / plastic endomicroscope objective (figure 5.1 (d,e)) is shown as a function of manufacturing volume in figure 5.2. For prototype quantities (50-200 units), the use of diamond-turned lenses removes the burden of purchasing an expensive mold, while still enabling reasonably priced miniature integrated endomicroscope objectives to be assembled for $500-$660. At higher production quantities, the use of injection molding becomes highly beneficial, decreasing the costs of the objectives to below $100. In

comparison, an all-glass endomicroscope objective costs an estimated $8,000 for prototyping and $3,000 in production quantities.

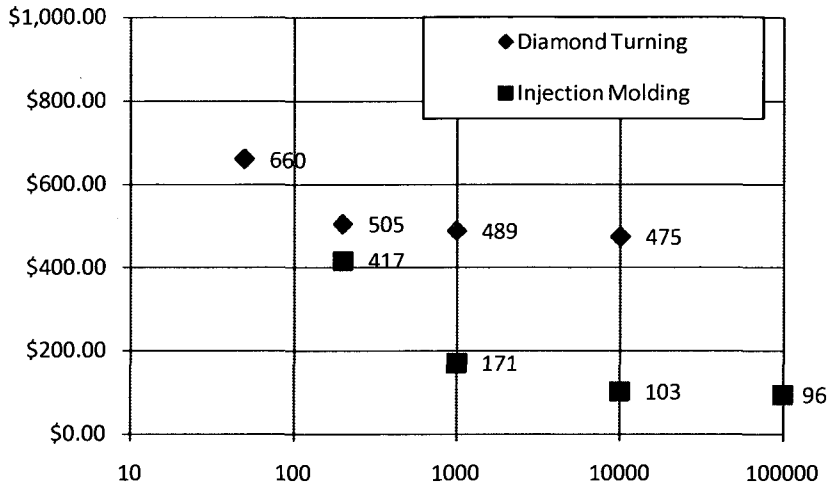

Figure 5.2: Hybrid glass/plastic objective cost summary for prototyping (Diamond-turning) and production (Injection-molding) quantities.

5.4. Biological Imaging Results

The biological imaging performance of the low-cost, self-centering miniature microscope objective (figure 5.1d,e) was studied for a series of tissue and cell samples mounted on conventional glass microscope slides. The samples were illuminated in the Kohler configuration for transmitted light brightfield imaging, or in the epi-configuration for fluorescence imaging. The image of the specimen formed by the miniature objective was re-imaged onto a CCD camera (Zeiss, MRc5) with an infinity-corrected 10x / 0.45 microscope objective and tube lens. Figure 5.3 presents brightfield images of two differently stained histopathology specimens acquired with a conventional microscope objective (40x / 0.95) (figure 5.3a,b) and the miniature objective (figure 5.3c,d). Figure 5.4 demonstrates fluorescence imaging with a triple-labeled slide of bovine pulmonary artery endothelial cells (Invitrogen F-14780), revealing F-actin (labeled green), mitochondria (red) and cell nuclei (blue). In both brightfield and fluorescence modes, image quality was noticeably higher with the conventional benchtop microscope objective, but cellular and sub-cellular detail could be resolved with the low-cost miniature lens system.

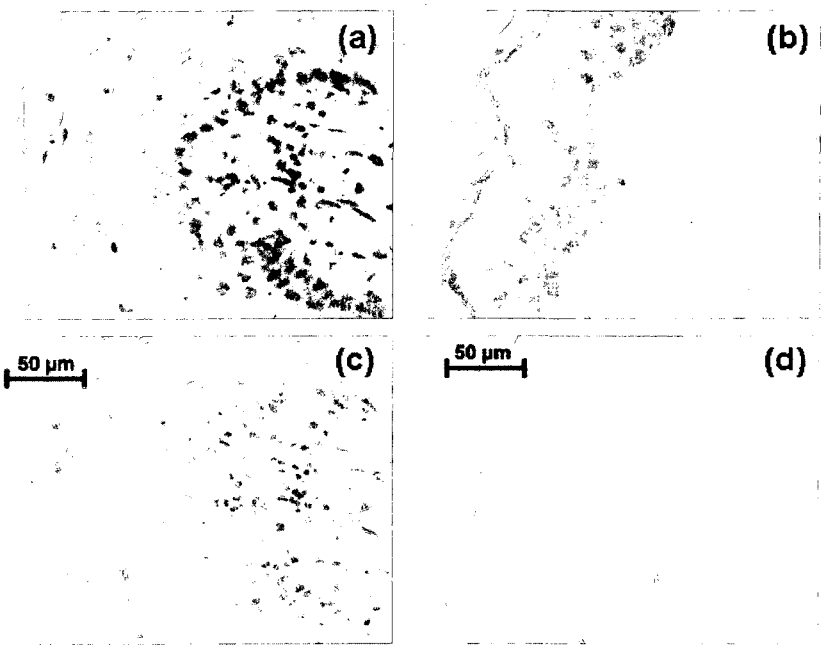

Figure 5.3 - Brightfield microscopy with the hybrid self-centering microendoscope objective. Images of (a) H&E-stained buccal mucosa tissue section and (b) immunohistochemistry-stained skin section. (c,d) Corresponding images acquired with a Zeiss 40x / 0.95 plan-apochromat.

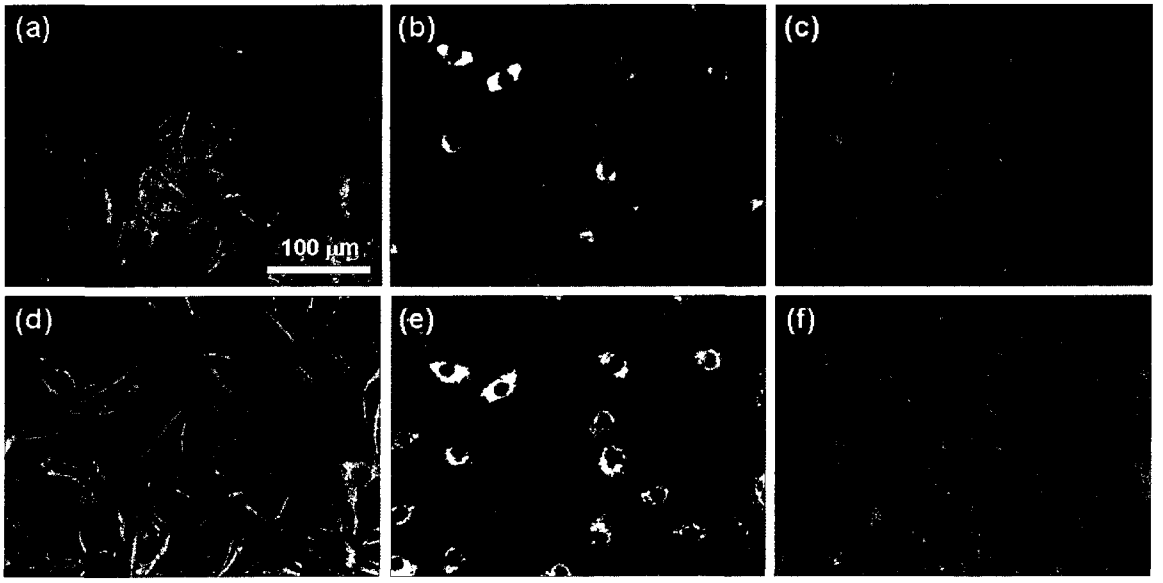

Figure 5.4 - Fluorescence microscopy with the hybrid self-centering microendoscope objective. (a-c) Images of triple-labeled bovine pulmonary artery endothelial cells at three different excitation / emission wavelengths. (d-f) Corresponding images acquired with a Zeiss 20x / 0.75 plan-apochromat

5.5. Conclusion

This chapter concludes my work in the area of low cost, high performance miniature objectives. I have shown in chapters 3 and 4 that high-performance miniature objective lenses can be assembled using the synergistic features of a hybrid glass / plastic optical design, with LIGA optomechanical parts. Of particular importance, is the ability to create self-centering optomechanics using LIGA technology providing a means to create easy to assemble systems. In this chapter a thorough analysis of the fabrication and assembly costs of these self-centering objectives have been analyzed for prototype and production volumes demonstrating that these systems may be realized at low costs, raising the prospect of disposable endomicroscopy optics for high-resolution *in vivo* imaging and point-of-care diagnostics. The imaging performance of these objectives have been evaluated against research grade microscopes and been shown to have similar quality. More *in vivo* imaging with these objectives is still needed and should be explored in the context of the Bi-FOV endoscope to be developed with this technology. This research was supported by the National Cancer Institute (NCI) under grants R01 CA124319 and R01 CA103830.

6. REAL-TIME SNAPSHOT HYPERSPECTRAL ENDOSCOPE FOR EARLY CANCER DIAGNOSTICS

The contents of this chapter are to be submitted in the following journal article: R. T. Kester, N. Bedard, L. Gao, and T. S. Tkaczyk, "Real-Time Endoscope for Early Cancer Diagnostics," J. Biomed. Opt. (To be submitted)

The second major goal of my research is to develop a widefield real-time hyperspectral imaging system for the macroscopic portion of the Bi-FOV endoscope. This chapter describes the development the IMS endoscope which is based on a new snapshot hyperspectral imaging technique called image mapping spectrometry (IMS) developed in our lab. The IMS approach is a fully parallel, high throughput, direct measurement approach that allows for the unambiguous recording and display of 3D (x, y, λ) datacubes in real time. A prototype IMS endoscope has been design, fabricated, and tested being capable of acquiring 3D (x, y, λ) datacubes of 350 x 350 x 48 at 5.2 frames per second. The IMS endoscope has successfully imaged tissue *in vivo* through a fiber optic probe of diameter 1.0mm and FOV of ~7mm and has detected what we believe is oxy-hemoglobin within and around vasculature patterns in the oral cavity although more testing is required to verify this result.

6.1. Introduction

Early diagnosis of cancer can significantly increase the chance of survival and improve quality of life post-treatment [Horner 2009]. However, most people are not detected with cancer until later stages (III or IV). Bio-photonics- based *in vivo* diagnostics such as optical imaging offers tremendous potential as an early cancer detection technology because it can be real time, non-invasive, high resolution, and inexpensive. To date most cancer screening techniques rely on white light visual examinations using the human eye or a digital color camera. These techniques obtain large scale morphologic and architectural details of the tissue but miss many of the more subtle, hidden clues pertaining to early stage cancer development such as metabolic activity. To address this issue researchers are now actively exploring the combination of spectroscopy with widefield imaging. Point spectroscopy studies have already shown that important endogenous early cancer bio-markers such as NADH, FAD, collagen, and oxy- and deoxy-

hemoglobin have distinct fluorescence- and reflectance-based spectral signatures [Drezek 2001, Wu 2007, Zonios 1999]. The combination of these two complimentary techniques may improve current screening devices to more correctly identify suspicious tissue sites. Ongoing clinical studies have shown that multi-spectral based imaging approaches particularly, Auto fluorescence Imaging (AFI) [Lane 2006], Narrow Band Imaging (NBI) [Sharma 2006, Kara 2006], and Tri-Modal Imaging [Curvers 2008] have improved early cancer detection specificities and sensitivities over the existing "gold standard" white light imaging method.

In light of this work, researchers are now actively pursuing real-time hyperspectral imaging devices which can provide 10's-100's of spectral channels per image pixel. The hope is that the increase in spectral information will translate to even more accurate early diagnosis of cancer. However, specific drawbacks have limited their use as affordable, real-time screening tools. The most common approaches are scanning based in either the spectral or spatial domains. These serial acquisition systems can only collect a fraction of the full 3D datacube at a single instant in time and therefore must tradeoff critical imaging parameters such as speed, image size, resolution, and/or signal-to-noise ratio (S/N). In addition, the hardware required performing the precision scanning and subsequent reconstruction is often very expensive, limiting its accessibility for most clinical settings. For example, spectral scanning techniques that utilize liquid crystal or acousto-optic tunable filters have been used by various groups for acquiring increased spectral bandwidth [Vo Dinh 2004, Gebhart 2007, Martin 2006, Roblyer 2009, Pan 2004] but can take >23 secs for complete data collection depending on the datacube size and when combined with a sensitive camera system can cost >$30K.

Recently, several new snapshot hyperspectral imaging approaches have been developed which have the potential to overcome the challenges of scanning based techniques by acquiring the entire 3D (x, y, λ) datacube simultaneously. These techniques include aperture splitting [Mathews 2008], field sampling [Matsuoka 2002, Bodkin 2006], computed tomography imaging spectrometry (CTIS) [Ford 2001], and coded aperture snapshot spectral imaging (CASSI) [Gehm 2007, Wagadarikar 2009]. To date

only aperture splitting and field sampling techniques have been shown to acquire and display the 3D (x, y, λ) datacube in real-time which is one of the main requirements for *in vivo* imaging. However, these techniques have other limitations. Aperture splitting has reduced optical throughput as it divides the numerical aperture from each object point by the same number of spectral channels. Field sampling sacrifices spatial for spectral resolution by under sampling the object plane in a discrete fashion or compromises optical throughput by sampling only a portion of the light from each point in the image. Therefore, while techniques that enable simultaneous acquisition of the 3D (x, y, λ) datacube are desirable for real-time imaging, the reduction in performance of the other imaging parameters has limited their usability for many *in vivo* applications.

Our group recently developed a new type of snapshot hyperspectral imaging technique called image mapping spectroscopy (IMS) that avoids many of these same limitations [Gao 2009, Gao 2010]. It works by spatially distributing (i.e. mapping) neighboring image zones to isolated regions on a CCD camera (see Figure 6.1A & 6.1B). The mapping is accomplished through the use of an array of densely packed tiny mirror facets located at the field position. With this technique there is no compromise of optical throughput or spatial resolution as the mirror facets are smaller than the incident point spread function and highly reflective. A dispersing element then spreads the spectral content from each isolated region in the mapped image into the surrounding void space on the CCD image sensor (see Figure 7.1C). In this way we can avoid any spectral overlap, resulting in un-ambiguous x, y, λ information on the image sensor. The IMS technique provides a very efficient and direct method for mapping each 3D voxel (volume element) of the datacube to s single 2D pixel (picture element) of the image sensor. Simple image re-mapping is sufficient to reconstruct the original object in real-time. This paper presents for the first time a real-time, hyperspectral endoscope based on the snapshot IMS technology developed for microscopy. To adapt the IMS technology for real-time *in vivo* imaging required development in four main area: first, decreasing the overall system size for portability to the clinic and improved optical throughput; second, increasing the spatial sampling of the IMS system for larger tissue region

observation; third, faster acquisition and display times for real-time (6 frames per second) operation. And fourth, development of a miniature optical probe for insertion into the instrument channel of a standard endoscope;

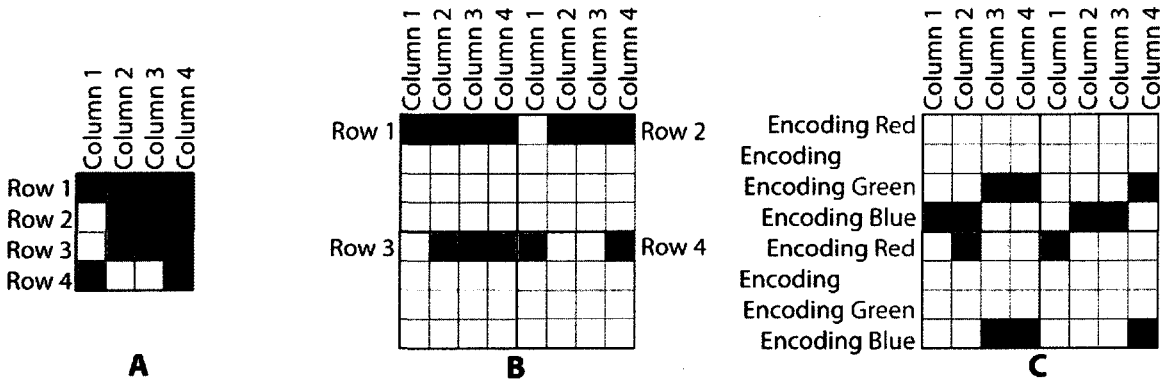

Figure 6.1. Image Mapping Spectroscopy (IMS) Concept.

6.2. Optical Design Concept

To achieve a more compact design with higher optical throughput and spatial sampling requires a more efficient optical design than the previous IMS systems which incorporates a large beam expander between the pupils and under utilizes the field-of-view of the collecting objective with a small image mapper. In the previous designs the beam expander was necessary for relaxing the design parameters of the system's components primarily the image mapper, however it was also responsible for reducing the throughput by over 50% and adding to overall large size of 24 in. x 24 in. x 12 in. [Gao 2010]. For the endoscopy system a new optimized design approach has been developed, as shown in figure 6.2, which removes all unnecessary optical components (beam expanders) and maximizes the functionality of each component. The final design is comprised of only 7 primary components: (1) a miniature objective and coherent fiber optic bundle for insertion into the instrument channel of a standard endoscope, (2) a 33X Image Relay which transfers the image at the face of the fiber optic bundle onto the Image Mapper, (3) an Image Mapper which breaks apart the image into sub images containing selected mappings of the original image, (4) a Collecting Lens which captures the different sub images from the image mapper creating an array of

stops at the back pupil plane of the collecting lens. (5) a Rows of Prisms for dispersing these sub-pupils and an (6) Array of Lenses which forms dispersed sub-images onto an (7) Image Sensor. The illumination system (not shown) is a 100W halogen lamp with a fiber bundle.

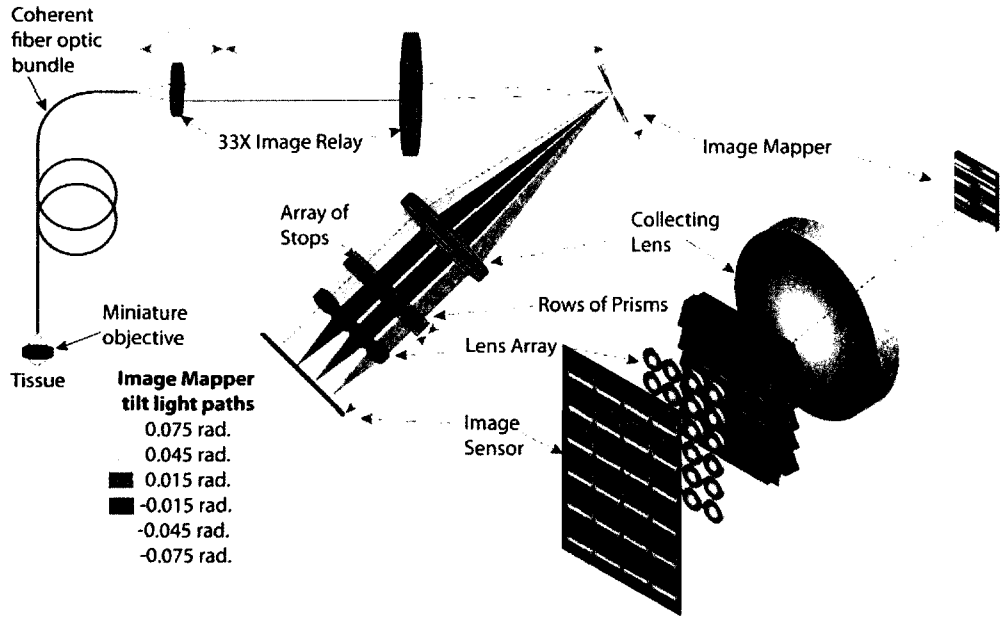

Figure 6.2. Image Mapping Spectrometer (IMS) Endoscope optical design layout.

Discussion of the system's operation begins at the tissue (distal) side where the illumination source provides light to an area of the tissue. Reflected, Scattered, and/or fluorescent light from the tissue is collected and imaged through a miniature widefield objective onto the distal face of the coherent fiber optic bundle (Sumitomo P/N: IGN-08/30) which is then transferred to the proximal face. A double telecentric 33X image relay system composed of a 20X objective (Olympus P/N: UPLSAPO, f=9 mm NA=0.75) and achromatic doublet tube lens (Thorlabs P/N: AC508-300-A1, f=300 mm, Dia. = 50.8 mm) magnifies and re-images the proximal fiber bundle face onto the image mapper. The image mapper is composed of an array of tiny mirror facets (total number = 3 x 350 = 1050 mirrors) which reflect linear mappings of the image to different regions in the stop of the collecting objective (Olympus P/N: MVPLAPO, f = 90 mm, NA ~ 0.189), shown by different ray colors, creating an array of stops. The individual mirror facets are 70 microns wide and 8.67 mm long. A row of prisms then disperse the light in

each stop in an orthogonal direction to the length of the linear mappings. A re-imaging lens array (Edmund Optics P/N: 49278 f=20mm, Dia. = 5mm) arranged in a 6 x 4 format forms 24 sub-images containing dispersed linear segments from similar tilted mirror facets. A 16 megapixel interline CCD camera (Imperx P/N: IPX-16M3-L) is used record the final mapped image. A simple software remapping program re-maps the sub-images to reconstruct the complete 3D (x, y, λ) datacube of the object (i.e. tissue region). Since there is no scanning and only trivial image processing, the system can acquire and display spectral images in real time, limited only by the CCD camera readout speeds (full frame = 3 fps, 2X binning = 6 fps).

The image mapper plays a key role in the hyperspectral imaging properties of the IMS endoscope. The total number of mirror facets (M), the number of resolvable image points along the length of each facet (N), and the number of different tilt angles (L), determine the volume and dimensions of the 3D (x, y, λ) datacube. N determines the total number of spatial data points in the x-dimension, given by the length of each facet divided by the width of the point-spread function at the mapper. M is the total number of spatial data points in the y dimension, given by the number of distinct tilt angles (L) multiplied by the number of repeating blocks in the image mapper. Λ is the total number of spectral data points for (L) resolvable spectral bands (λ). For our system Λ is equal to ~ 2 x L, the Nyquist sampling rate. The resulting 3D datacube is then $M \times N \times \Lambda$. In order to generate the required void regions to provide room for spectral dispersion, the image mapper is composed of repeated blocks of grouped facets with L tilt angles, as shown in figure 6.3 with L = 4 for clarity. In the actual IMS endoscope there are L = 24 tilt angles in each block. Each facet re-directs a part of the image within that block to a unique location in the pupil, shown labeled in figure 6.3 with the same number as its corresponding tilt angle. The block is then repeated down the length (x-axis in figure 6.3) of the image mapper.

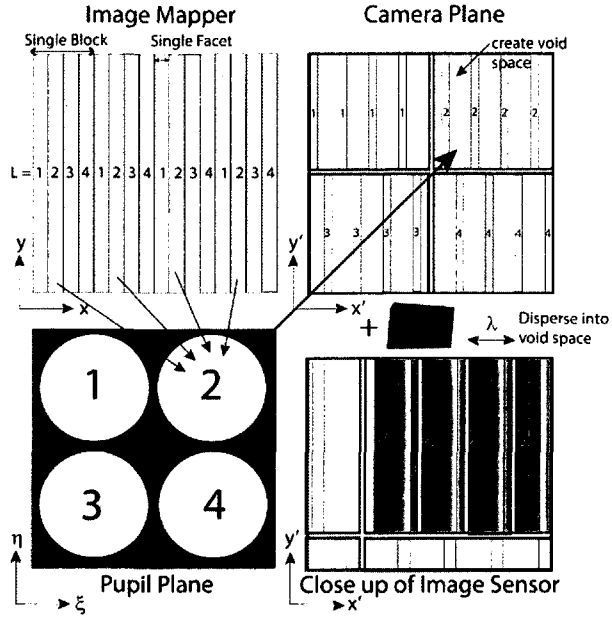

Figure 6.3. Diagram showing the role of the image mapper in the system as it relates to the final 3D datacube size. See text for detail.

The design is also telecentric in the optical space around the image mapper which is important for the mapping. The chief rays reflected by specific facets in each mapped image all have the same reflection angle. After passing through the collecting lens, light associated with these chief rays enters the pupil at a location corresponding to the specific facet from the image mapper. Each re-imaging lens is then dedicated to only one tilt direction and images only the lines from each tilt. The image is thus efficiently redistributed for spectral separation without loss of light. The IMS endoscope is designed to achieve a 3D (x, y, λ) datacube of 350 × 350 × 48 sampling (x, y, λ); however, due to under sampling by the coherent fiber bundle, the system's effective sampling is limited to 200 x 200 x 48. This corresponds to 100 μm spatial resolution over a tissue area of 10 mm (closest conjugate plane). This resolution was chosen to resolve tissue vascularization which is a critical feature for early cancer detection. Table 6.1 lists the system specifications.

Table 6.1. Design requirements for the real-time ISE system.

Optical Requirements	**Requirement**
Spectral Range	450-650 nm
Spectral Bands	48
Image Size	200x200
Frame Rate	8-10 fps
FOV	10 mm
Spatial Resolution	100 μm
Spectral Resolution	4-10 nm

The spectral range of the IMS endoscope covers most of the visible spectrum (450-650 nm) which includes important spectral features from endogenous tissue fluorophores (NADH, FAD, Collagen, etc), oxy-and deoxy-hemoglobin absorption and scattering. The spectral resolution for detecting these features was chosen to be between 4 – 10 nm to provide adequate resolution for distinguishing these tissue features. For the initial prototype system 48 spectral bands were chosen for simultaneous acquisition over an ~96 nm spectral window corresponding to 4 nm resolution. This measurement window can be adjusted by simply inserting different bandpass filters into the system as long as it is within the designed spectral range. This is a nice advantage for this system over multi-spectral or other snapshot techniques allowing us to tune the system for specific contrast agents within the tissue. For initial experiments, four bandpass filters where used with the system covering the full spectral range from 460 nm – 747.5 nm as shown in Table 6.2.

Table 6.2 – Filters used with the IMS endoscope.

Filters (Chroma)	**Spectral range**
HQ 480/40 X	460 – 500 nm
HQ535/70 M-2P	500 – 570 nm
HQ 620/100 M	570 – 670 nm
HQ 710 / 75 M	672.5 – 747.5 nm
D 557/60 M	527 – 587 nm

A more detailed description of each critical component in the IMS endoscope design is discussed further in the sections below.

6.3. Prism and Lens Optical Design

Most of the IMS endoscope uses off-the-shelf optics with propriety lens prescriptions. The exception to this is the image mapper and the prism/lens array. For the custom prism/lens array system optical modeling software (ZEMAX) was used to achieve diffraction limited performance. Before modeling the system three different dispersing approaches were explored: a diffraction grating, a single prism, and a double Amici prism. The double Amici prism design was chosen as the best approach as it could achieve the right range of dispersion angles while removing the central deviation angle which is important for maintaining a common perpendicular image plane for multiple optical systems that use the same image detector. The disadvantage of the double Amici design is that the prisms are much thicker than either the diffraction grating or single prism making it difficult to keep the system compact. This is especially important as all the sub-images must fit on the image sensor which has dimensions of 24 x 36 mm. To address this issue the prism was broken into 6 smaller prisms that could then be stacked on top of each other to cover the full array of stops in the collecting objective. The final design of the system is shown in Figure 6.4.

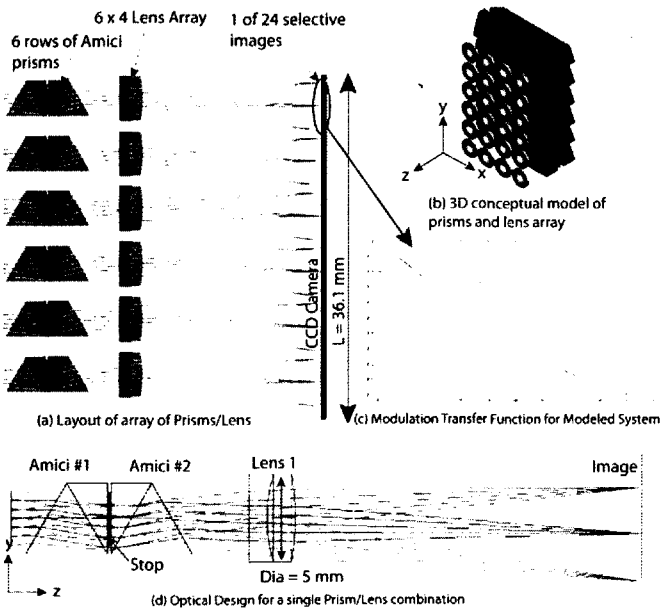

Figure 6.4. Prism/Lens array design layouts and performance metrics.

The prism is composed of 12 custom Amici prisms fabricated by Tower Optical, Inc. The prisms are placed back-to-back with a stop array between them as shown in figure 6.4(d). The re-imaging lens array is composed of 24 achromatic doublets (Edmund optics P/N: 45-408) placed 4.376 mm behind the prism. A cross section profile in the y-z plane of the design is shown in figure 6.4(a). The final image size is 5.33 mm in diameter with a fiber spacing of 27.3 μm and fiber core diameter of 16.4 μm. Each linear mapping on the CCD camera has dimensions of 16.7 μm x 5.33 mm. The linear mappings are sampled slightly above the Nyquist criteria with 7.4 x 7.4 μm pixels on the CCD. The individual stop diameters are 2.02 mm neglecting diffraction effects and are separated 5.6 mm apart. The width of the individual prisms (along the y-axis), diameter of the lens, and size of the final image were designed to be less than this stop spacing preventing overlap and/or vignetting in the sub-images. All sub-images and their spacing's reside within a 33.33 mm x 22.13 mm region which is also within the CCD detector area. The prism and lens array are diffraction limited across the visible spectrum as shown in the modulation transfer function (figure 6.4(c)) for three field positions (0, -2.8 mm, +2.8 mm) and one (F-band) out of the three bands (F- 486.1nm, d- 587.6nm, C- 656.3nm) commonly used for visible color correction. Figure 6.4(d) and table 6.3 provide a more detailed layout and accompanying lens prescription for the design. The input parameters used for the design were an entrance pupil size of 2 mm and angular field-of-view = +/-7.64° matching the expected stop array parameters created by the preceding collecting objective and 33x image relay.

Table 6.3. Lens Prescription for Prism/Lens array.

Surf	Comment	Radius	Thickness	Glass	CA	Y tangent*
1*	Amici Prism #1	Infinity	2.310	F_SILICA	2.84	0.577350
2*		Infinity	1.155	N-SF57	3.60	-0.577350
3		Infinity	0.100		3.59	
STOP		Infinity	0.100		3.57	
5	Amici Prism #2	Infinity	1.155	N-SF57	3.55	
5*		Infinity	2.310	F_SILICA	3.55	0.577350
6*		Infinity	4.374		2.80	-0.577350
7	Lens #1	75.590	1.030	SF10	4.12	
8		8.630	1.610	BAFN10	4.36	
9		-14.110	19.712		2.30	
IMA		Infinity			5.33	

*Tilted Surfaces

6.4. Miniature Objective

For initial experiments a miniature grin lens (Grintech P/N: GT-IFRL-100-010-50-NC) was used to image samples onto the fiber bundle. The grin lens has a focal length, f = 0.92 mm, and diameter, d = 1.0 mm, making it compatible for most endoscope tool channels. A ZEMAX optical model of the grin lens was provided by Grintech for evaluation of its performance. Figure 6.5(a) shows the optical layout for the lens at its designed conjugate distance of 10 mm corresponding to a field-of-view of 8.4 mm. At this field of view the spacing between the fibers within the bundle provide 43 μm sampling of the object corresponding to a resolution of 86 μm based on the Nyquist criterià. The simulated performance of the lens indicates around 6 percent barrel distortion as shown in figure 6.5(b). The errors in image mapping introduced by this barrel distortion can be corrected by our software remapping matrix described later in this paper. The predicted polychromatic modulation transfer function (MTF) plots (Figure 6.5(c)) indicate significant reduction in the image contrast as the spatial frequencies increase. For comparison, the top curve of the plot is the diffraction limited MTF curve, while the system's MTF curve for the three commonly used field positions (on-axis, 0.707 field, and full field) are shown in the colored lines.

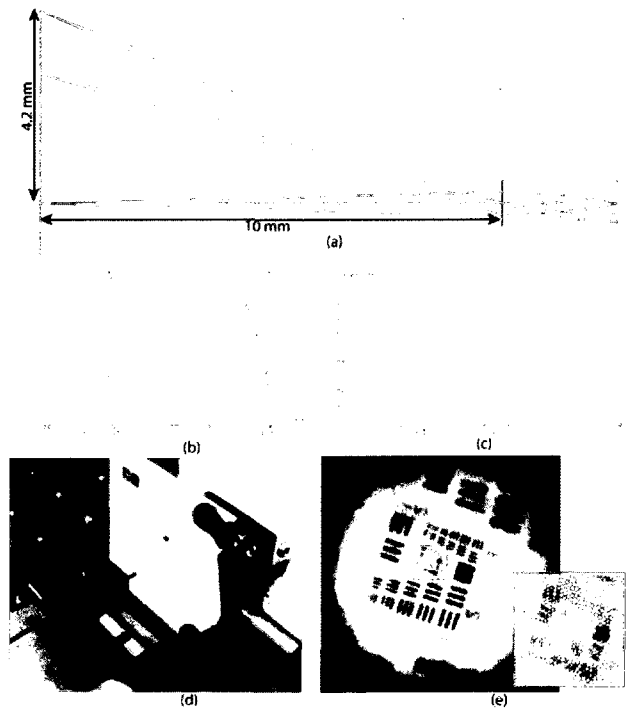

Figure 6.5. IMS endoscope miniature grin lens: (a) design, (b) performance metrics, (c) prototype, and (d) imaging result.

A prototype of the grin lens / coherent fiber bundle was constructed and used to image a 1951 USAF resolution target at its optimum working distance of 10mm as shown in Figures 6.5(d) and 6.5(e). The illumination source was a tungsten halogen lamp (100W) with a ground glass diffuser. The field of view (FOV) of the system was measured by comparing the known size of the bars in the image to the overall image size giving ~ 7 mm, which is slightly less than the expected value of 8.4 mm. Position inaccuracy of the target with respect to the grin lens was probably the largest source of error in this measurement. At this conjugate position, the smallest resolvable line pair was in the Group 4 Element 1 bars (Figure 6.5(e)) that correspond to 16 LPMM or 62.5 μm resolution at the object plane. This is slightly better than the designed resolution of 86 mm, most likely due to the closer conjugate position. The ability to see these small bars is somewhat encouraging based on the large expected image aberrations from the grin lens. In the future we plan on developing a custom diffraction limited miniature lens for detection of the small, low contrast features within tissue that will be obscured by the lower quality grin lens.

6.5. Image mapper

By removing the beam expander between the pupils in the previous IMS designs, larger tilt angles are needed for the image mapper to achieve the necessary pupil spacing's. This requires a new design approach for the image mapper since the previous monolithic design and fabrication approach could not achieve these tilts without exceeding the 300 micron depth of cut limitation of the diamond tools. To overcome this limitation, the image mapper was broken into 3 smaller segments of dimensions 24 x 8.67 mm, length and width respectively. Each segment is composed of 350 mirror facets. The three segments are bolted together to create a single image mapper that is 24 mm high and 26 mm long (Figure 6.6(a)). To reduce the possibility of alignment errors of the individual segments, they are fabricated at the same time using a diamond raster fly cutting process (Figure 6.6(b)). The fabrication method is described in more detail in our previous publication [Kester 2010]. For this application the individual mirror facets within each segment are 70 μm wide and 8.67 mm long. This size was chosen to provide close to Nyquist

sampling rate of the intermediate image of the fiber bundle. The fiber bundle image has a diameter of 24 mm with a fiber spacing of 122.7 μm and fiber core size of 73.7 μm. The image mapper is designed to be positioned at a 20 degree angle to the incident image, providing an angular separation of 40 degrees between the incident and reflected paths - sufficient displacement for the large collecting lens to avoid vignetting. The reflected beam tilt angle is also small enough to keep the image mapper within the depth of field range of the incident image. The image mapper's axial position range due to the 20 deg. tilt is +/- 4.44 mm with respect to the on-axis focal plane. The allowable depth of field is +/- 5.84 mm based on the geometric minimum blur diameter being less than or equal to the size of an individual mirror facet (70 μm). The 4 possible x-tilts for the image mapper facets are +/- 0.015 and +/- 0.045 radians while the 6 possible y-tilts are +/-0.015, +/-0.045, and +/-0.075 radians. There are 24 unique combinations of these tilts that are used to create a 4 x 6 stop array in the collecting objective. As mentioned earlier the arrangement of these facet tilts are repeated down the height of the image mapper covering the entire surface area. A picture of a finished segment of the image mapper is shown in figure 6.6(c) next to a U.S. Quarter for size comparison.

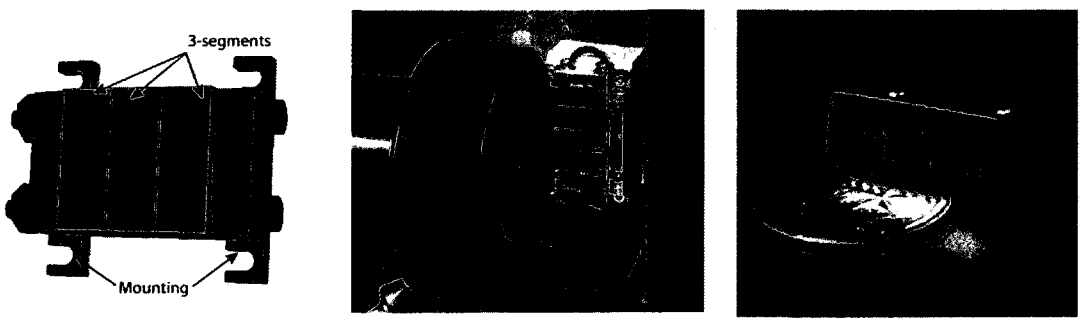

(a) (b) (c)

Figure 6.6. Image mapper (a) design, (b) fabrication process, and (c) prototype segment.

6.6. Prototype

A prototype of the IMS endoscope has been assembled as shown in figure 6.7. The system resides on a portable optical breadboard of dimensions equal to 12 in x 24 in. The green line in figure 6.7(a) traces the path of the incoming light from the grin lens to the image mapper. A reference CCD camera is

incorporated in the system using a 92:8 beamsplitter. A filter wheel between the 33X image relay lenses has been added to the system to select different spectral windows for taking measurements.

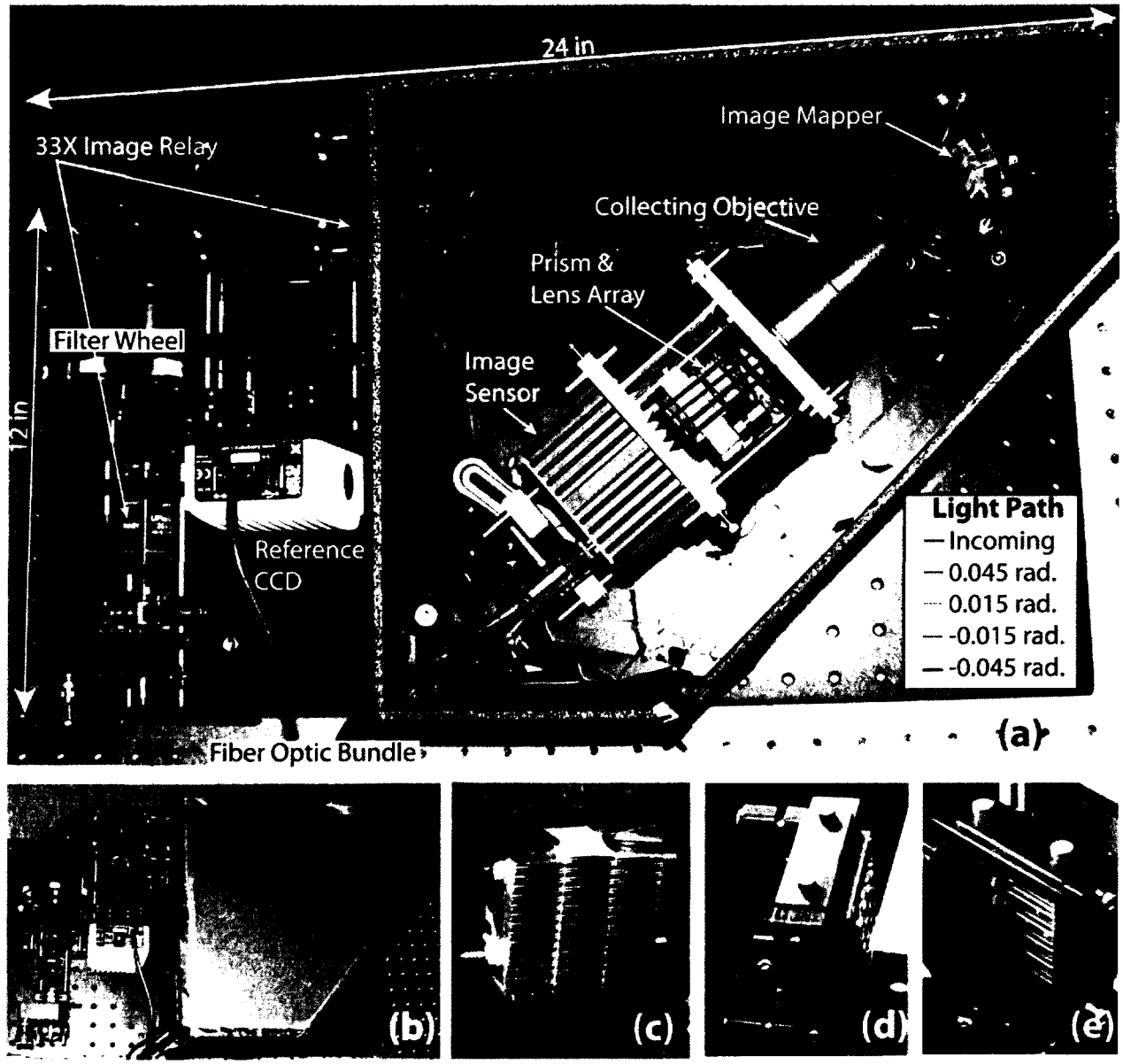

Figure 6.7. – Assembled IMS endoscope system prototype (a) Full system and (b) with cover. Close up images of (c) image mapper, (d) lens array, and (e) rows of Amici prisms.

The multi-colored paths after the image mapper show the possible (y-axis) paths the light may travel after reflection depending on the facet tilt geometry. Figure 6.7(b) shows the prototype with the cover on for blocking ambient light. The system can operate in normal lighting conditions. Figure 6.7(c) displays a close up of the three segment image mapper comprising 1050 mirror facets. The three segments are

identical to each other creating three ramp functions across the face of the image mapper. Initial testing showed excess shadowing of the adjacent image mappers due to edge height differences. To remove this shadowing the middle segment was slightly raised to match the mirror opposite of the tilt facets. Future image mappers will have a mirrored segment fabricated as the middle segment. Figures 6.7(d) and 6.7(e) display close ups of the rows of prisms and lens array assembly.

A custom LabVIEW interface was also developed for the IMS endoscope for acquiring, reconstructing, and displaying 3D datacubes is shown in figure 6.8. In real-time, the program displays one user-selected false-colored spectral channel from the full reconstructed datacube, while simultaneously showing spectral slices through the datacube for one set of X and Y spatial lines. For on-the-fly analysis of acquired data, tools are included to graph the spectra from any spatial coordinate, or to easily scan through spectral channels. Functions for saving raw data, spectral channel images, or full datacubes are also provided.

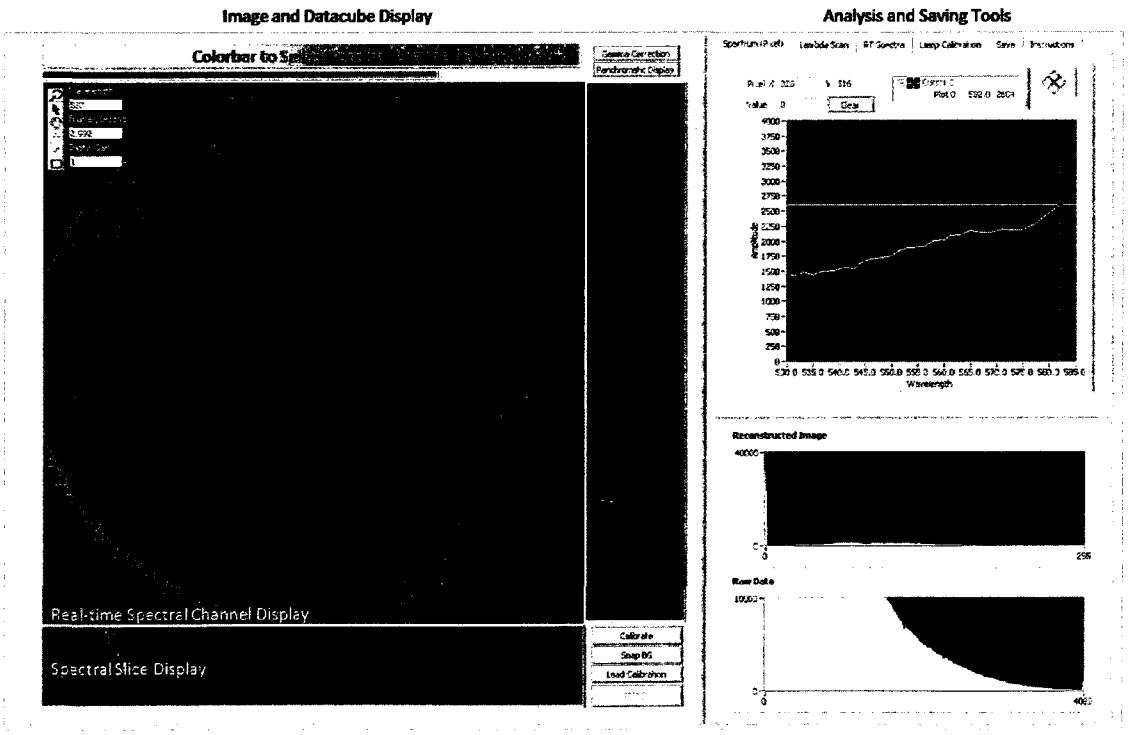

Figure 6.8 – The custom LabVIEW interface for the IMS endoscope for acquiring, reconstructing, and displaying 3D datacubes

6.7. Testing and Calibration

The spectral range and resolution for the IMS prototype was calibrated using a liquid crystal tunable filter (LCTF, Cambridge Research Instruments) placed in front of a broadband 100W halogen lamp. Narrowband light from this setup was projected onto a ground glass diffuser to create uniform illumination in the field-of-view of the IMS system. At every ~ 2 nm spectral step, a raw image was recorded on the CCD camera and the relative change in the image position (# pixels moved) was recorded. The spectral position of the LCTF was independently verified using an Ocean Optics Spectrometer (P/N: USB4000) during the experiment. Figure 6.9 shows the results of this experiment compared to the theoretical performance of the system. Note that the IMS system is capable of simultaneously recording any 48 consecutive spectral channels (i.e. pixels) within the spectral range, and the selection of channels can be easily adjusted by inserting different bandpass filters into the system. This corresponds to a ~96 nm wide spectral window depending on the where in the spectrum the measurements are located.

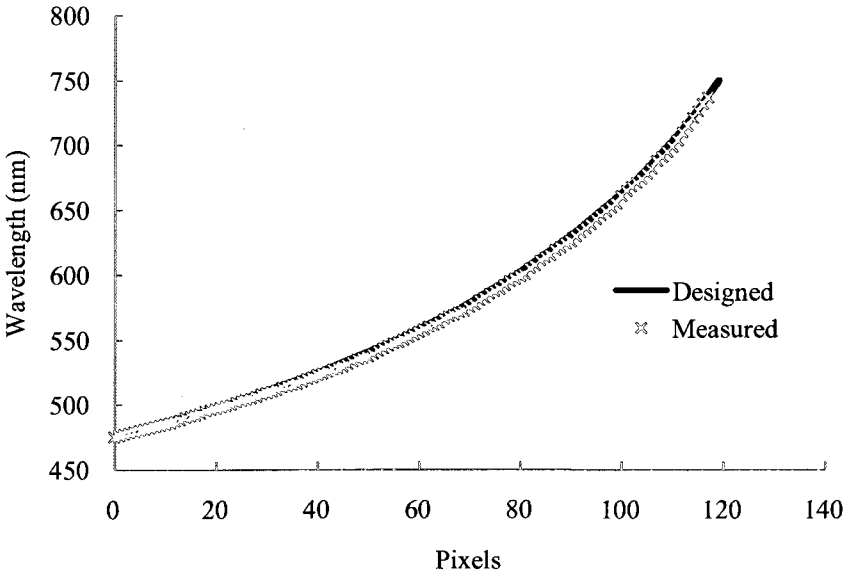

Figure 6.9. Comparison of predicted and measured wavelength to pixel shift for IMS endoscope system

The same system setup was used to create the mapping matrices that transform the 2D raw data into a 3D (x, y, λ) datacube, as previous described by Gao. [Gao 2010]. Briefly, monochromatic images were recorded on the CCD camera and bright pixels were thresholded. One-pixel wide lines were fitted to these thresholded pixels, which represents light from a single 70-um wide mirror facet of the image mapper. By knowing the periodic pattern of the image mapper facet angles, fitted lines in the raw data can be reshuffled into a single monochromatic image; the result of this process is a lookup table that provides raw data coordinates for every pixel in the reconstructed image. An illustration of these steps is shown in figure 6.10. This procedure was repeated using monochromatic images throughout the spectral range of 450 nm – 720 nm.

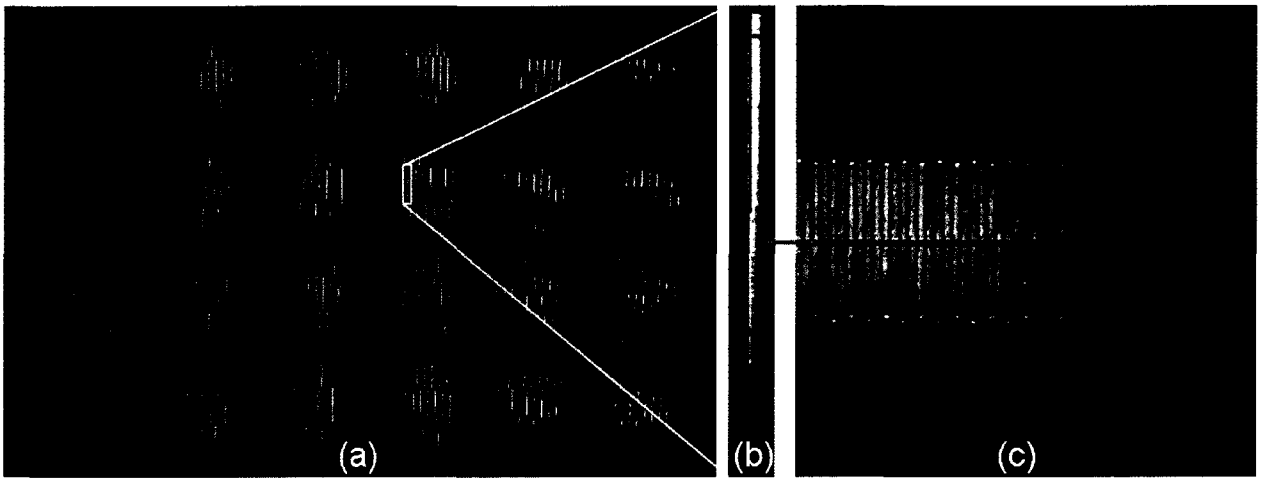

Figure 6.10 – Demonstration of how the raw data is remapped to form a single monochromatic image within the simultaneously acquired 3D (x, y, λ) datacube. This process is repeated for each wavelength within the datacube.

To account for small mapping errors between the sub-images in the system, a Ronchi ruling was used to vertically correct image lines from each mirror facet. A reconstructed image of the Ronchi ruling was recorded and an edge-detection program was run to determine the misalignment of each image line in terms of pixel shift. The mapping matrix was then updated to include this offset. Figure 6.11 demonstrates this procedure for an actual image of the Ronchi ruling. The uncorrected mapping is shown in 6.11(b) and the final correct mapping is shown in 6.11(c)

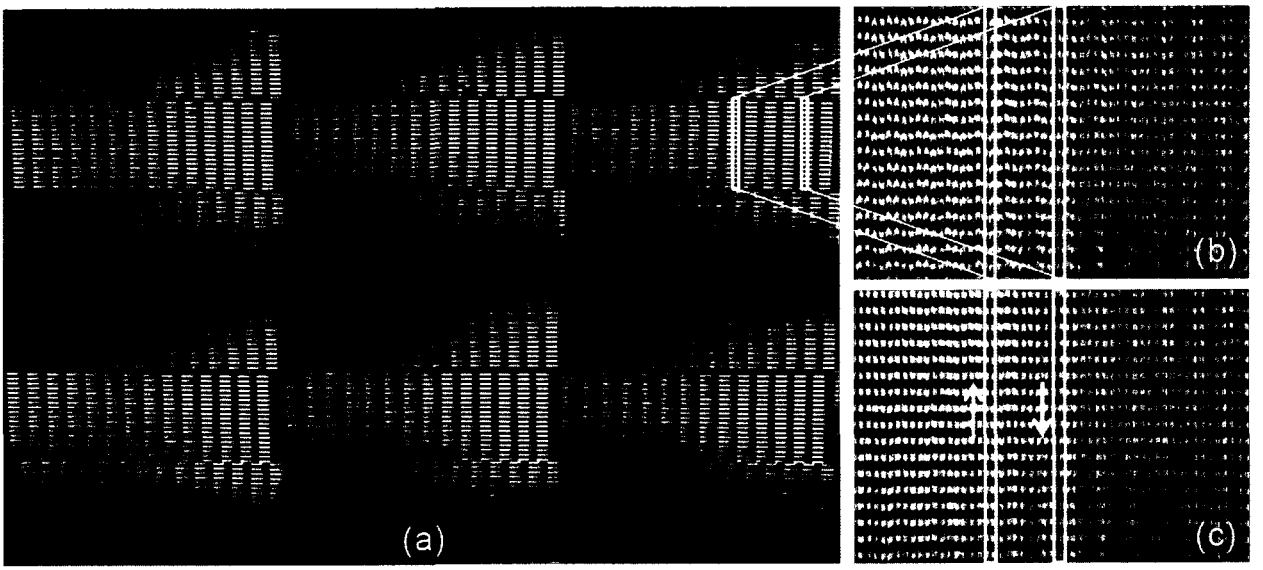

Figure 6.11 – Depiction of the procedure for correcting small mapping errors in the IMS system. (a) Close up of 6 sub-images in the IMS system. (b) The incorrect remapped image of a Ronchi ruling. (c) The corrected remapped image of a Ronchi ruling.

Once the correct mapping matrices were determined for each wavelength, a vector-shaped lookup table containing indexes into the raw data was created for the entire datacube. Simple indexing and reshaping operations allow the 2D raw data from the CCD to be transformed in real-time into a 3D datacube. Using the custom LabVIEW program, the datacube can be calibrated for intensity (by imaging a reflective target with a broadband source), background signal can be subtracted, signals can be averaged or binned, and the spectral band can be shifted all simultaneously, with the speed only limited by the frame rate of the camera.

The power of this technique is that the full 3D (x, y, λ) datacube can be recorded at a single instant in time unambiguously. Figure 6.12 shows this principle in practice. Figures 6.12(a) and 6.12(b) show a raw monochromatic image with a close up of one of the 24 sub-images. Figures 6.12(c) and 6.12(d) show the polychromatic version (527-587nm), in which all 48 spectral images are being acquired simultaneously. This image was taken of a white sheet of lens paper; the horizontal stripes in the images are due to sampling of the fiber bundle pattern, as shown in 6.12(e). The illumination was provided by a 100 W halogen lamp. A bandpass filter (Chroma D557/60 M) was used to provide a spectral window of

about 60 nm centered at 557 nm. Notice that there is no overlap of light between the separate dispersed lines. Image artifacts apparent in the sixth column of sub-images are due to a fabrication error in the image mapper that will be corrected in the future.

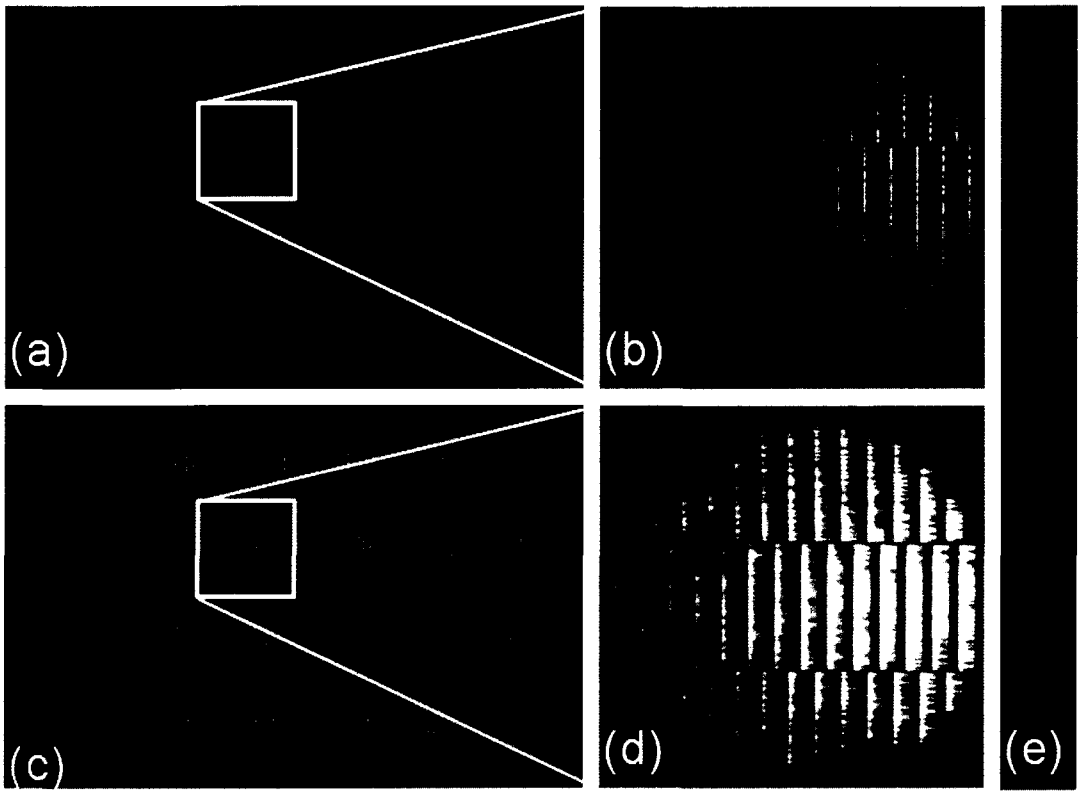

Figure 6.12– Raw monochromatic image from IMS endoscope showing (a) all 24 sub-images, (b) close up of a single sub-image. Polychromatic image with (c) all 24 sub-images and (d) close up of a single polychromatic sub image. (e) A close up of a single line within a monochromatic sub-image shows the individual fibers within the multi-fiber bundle.

To verify correct spatial remapping, spatial resolution, and intensity calibration, images of a 1951 USAF resolution target were taken with the endoscope portion removed from the system. Figure 6.13(a) shows the raw data acquired from the CCD camera. Figure 6.13(b)-(e) are 4 representative spectral images out of the 48 acquired simultaneously and displayed in real-time with the IMS endoscope. The spectral channel wavelengths for these images are 584 nm, 567 nm, 549 nm, and 532 nm respectively. The acquisition time was 5.29 frames per second (fps) which is the maximum readout rate for the camera with vertical binning. Using the LCTF and other test targets, spectral calibration was verified by

comparing the measured spectra of pixels throughout the data cube with the readout of an Ocean Optics Spectrometer.

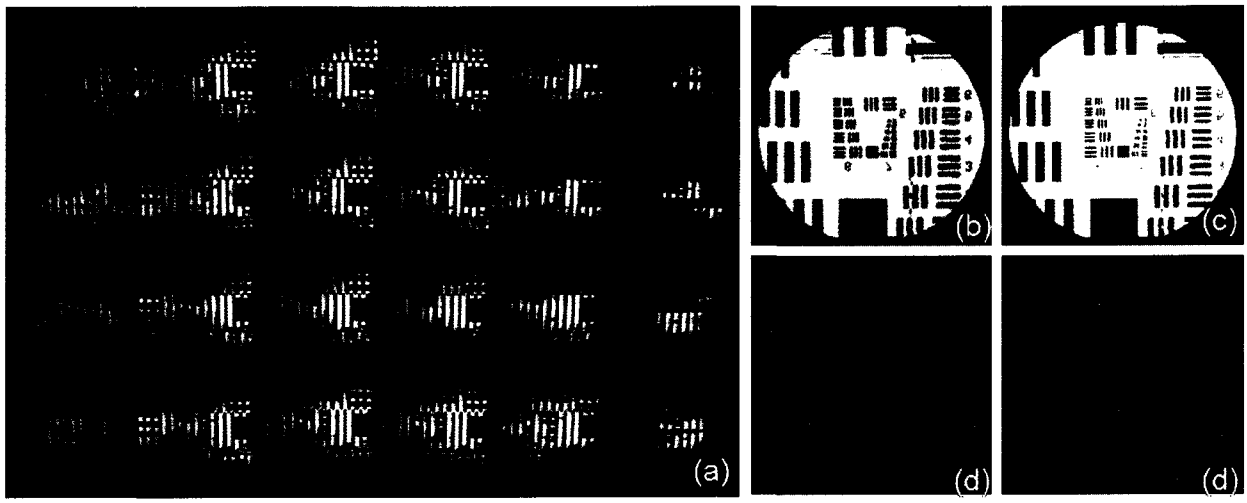

Figure 6.13 – (a) Raw image from the IMS of a USAF resolution target acquired simultaneously. (b-e) 4 out of 48 remapped images for the wavelengths (584 nm, 567 nm, 549 nm, 532 nm).

6.8. Biological Images

To evaluate the biological imaging performance of the IMS endoscope, the system was used to image the vasculature of the lower lip of a normal volunteer. The lip was illuminated by a 100 W halogen lamp through a fiber optic bundle. The irradiance level at the tissue was measured to be 41.8 mW/cm^2. An intensity calibration of the source was performed prior to tissue imaging by imaging a white piece of paper. The fiber optic tip of the IMS endoscope was place at ~ 10 mm from the tissue site. Figure 6.14 shows the experimental setup for imaging.

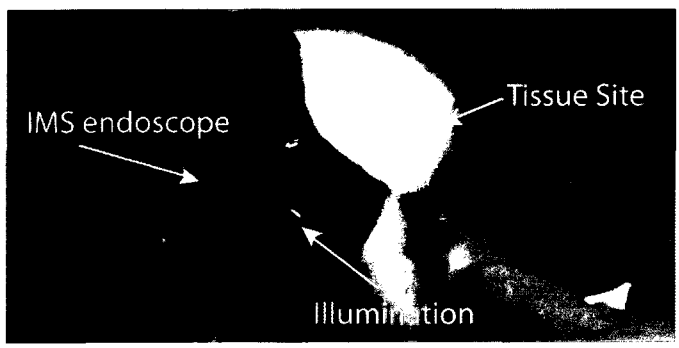

Figure 6.14 – Experimental setup for imaging the tissue vascularization of the lower lip of a normal volunteer.

A green filter (Chroma D557/60 M) with a spectral window from 527-587 nm was placed into the IMS system for this experiment. This filter was selected to optimize the spectral response of the IMS endoscope for oxy-hemoglobin's green absorption lines at 542 nm and 576 nm. The full size of the 3D (x, y, λ) datacube acquired with this filter is 350 x 350 x 29. The main limitation on the spectral range is due to the bandwidth of the filter (only 60 nm). To fully utilize the spectral range of the system at this region would require a custom filter which was not available at the time. Under these experimental conditions, the IMS endoscope was able to acquire datacubes at the fastest read-out time of the camera (5.2 fps) corresponding to an integration time of 192 ms. The dynamic range of the datacubes where 12-bit with the lowest gain setting on the camera at 6 dB. The custom LABVIEW software remapped and displayed the datacubes at a rate of 3.2 fps. Figure 6.15(a) shows one of the 29 spectral images (wavelength 546 nm) within a single acquired datacube.

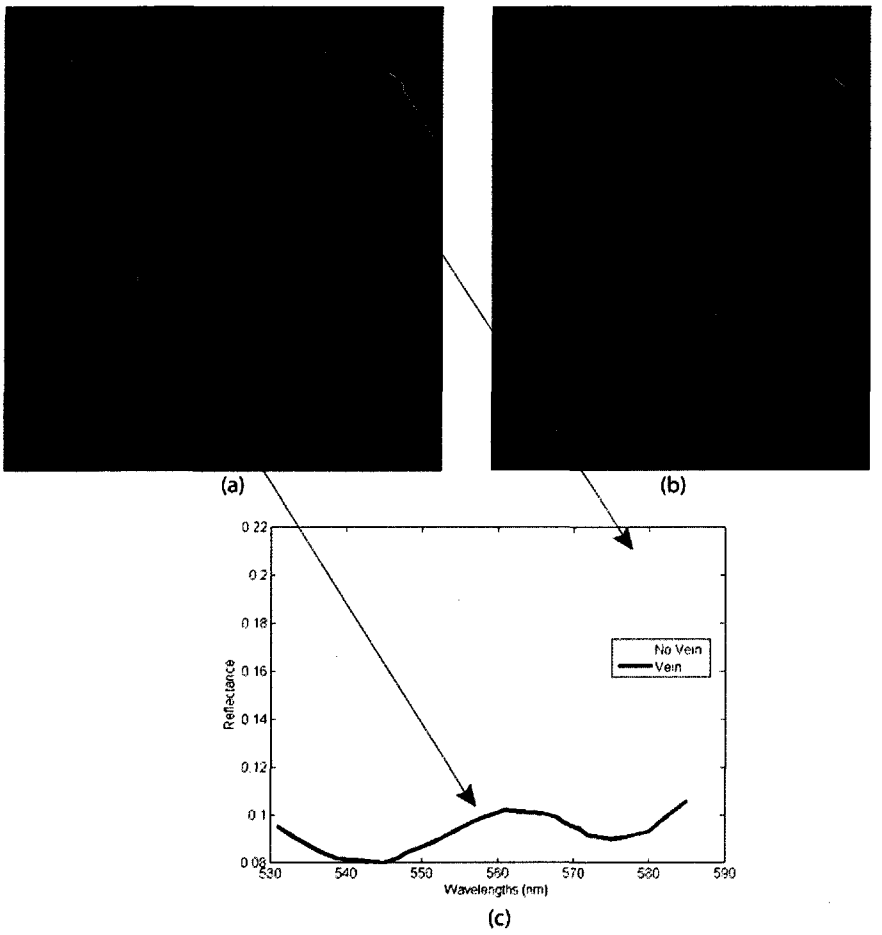

Figure 6.15 – Lower lip vasculature imaging results from a normal volunteer using the IMS endoscope. (a) One of the 29 spectral images acquired simultaneously with the IMS endoscope corresponding to the 546 nm band. (b) Reference image taken with the color CCD camera. (c) Spectral curves from an area in the image where there appears to be a vein (black sold line) and no vein (dashed gray line).

As one can see the image quality is slightly reduced due to some intensity artifacts (periodic lines through the image) caused by fabrication defects in the image mapper. Ongoing research is being carried out to reduce or eliminate these effects for future systems. However, even with these defects tissue architectural features such as vasculature patterns can be easily observed and have similar image contrast as those acquired using a color CCD camera (Luminera Infinity II) from the same tissue site. The ability of the IMS endoscope to detect the spectral information within an image simultaneously was also evaluated during this experiment. Spectral curves from two regions within the datacube are shown in figure 6.15(c). The black solid line is taken from a region in the datacube where there is a vein (left red

box in 6.15(a)) and the dashed gray line is taken from another region in the datacube where there is no vein (see right red box in 6.15(a)). We believe the "W" shape of the two curves corresponds to the oxy-hemoglobin absorption peaks around 542 nm and 576 nm. Additional tests are required to confirm that this is the case. However, these initial results are very exciting and open up the possibility for real-time oxy-and deoxy-hemoglobin detection within a standard endoscope image.

6.9. Discussion and Conclusion

An endoscopic version of the image mapping spectrometer has been successfully demonstrated. The system is capable of collecting 48 spectral images simultaneously over a spectral window of ~ 96 nm which corresponds to a spectral sampling of 2 nm. This spectral window can be positioned anywhere within the visible spectrum (450 nm – 650 nm) by inserting the appropriate filter between the 33X image relay. The system has also been shown to acquire the full 3D (x, y, λ) datacube = 350 x 350 x 48 in real-time a rate of 5.2 fps and displaying this datacube at 3.2 fps. The system's spatial resolution and contrast is sufficient for detecting the vasculature patterns of tissue and has successfully imaged the inside of the lower lip *in vivo*. Results from this initial experiment, indicates that we have detected oxy-hemoglobin within the image, however, more thorough testing is required to confirm these results.

Future work is still needed in several areas before the endoscope system can be applied to clinical applications. First, the system must be ruggedized for transport to the clinic. Second, defects in the image mapper must be corrected to reduce image artifacts. Third, faster image acquisition and display will be required (8-10 fps) to eliminate motion artifacts. A faster camera has already been purchased that can achieve these speeds. And fourth, the spectral window for the system must be increased to detect more biomarkers. The next generation system's spectral window will go from 450 – 650 nm with a spectral sampling of 4.2 nm. In addition, further testing of the system for the detection of other early cancer biomarkers such as FAD, NADH will be done in the lab before clinical testing. We are encouraged by these initial results and believe the IMS endoscope will provide clinicians with a valuable screening tool

for more accurately locating early cancer sites. These sites may then be further evaluated using "optical" biopsy tools or more traditional biopsy methods although the later is more invasive. We are currently exploring combining the IMS endoscope with a microscopic detection technique for screening and diagnosing cancer within a single procedure although the work toward this dual mode system is still very early on.

Acknowledgements

The authors would like to thank NIH for their funding support of this project through the grant R01 CA124319 titled "Integrated Bi-FOV endoscope for detection of Precancer" and grant R21EB009186 titled "Image Slicing Spectrometer (ISS) for high resolution sub-cellular microscopy".

7. DEVELOPMENT OF IMAGE MAPPERS FOR HYPERSPECTRAL BIOMEDICAL IMAGING APPLICATIONS[a]

[a]The contents of this chapter have been published in the following journal articles: R. T. Kester, L. Gao, and T. S. Tkaczyk, "Development of image mappers for hyperspectral biomedical imaging applications," *Appl. Opt.* **49**, 1886-1899 (2010)

Implementation of the IMS concept into a compact endoscope system (as presented in Chapter 6) required significant development of the image mapper. The image mapper is the most critical component in the IMS technology responsible for mapping the original 3D (x, y, λ) datacube onto a 2D detector plane. This chapter presents a new design and fabrication method that I developed for creating large format (> 100 mirror facets) image mappers. To verify the new methods, a 250 facet image mapper with 25 multi-tilt angles was designed and fabricated using precision diamond raster fly cutting with surface shaped tools. The resulting image mapper has minimal edge eating, tilt errors of < 1 mrad, and an average roughness of 5.4 nm. Crosstalk between adjacent sub-images were measured to be ~10% due to individual facet geometry errors. Further improvements in the fabrication and design methods are still being developed with the ultimate goal of crosstalk < 1%. The techniques described here were used for fabricating the image mappers for the IMS endoscope as well as a high sampling fluorescence microscopy system [Gao 2010] also being developed in our lab.

7.1. Introduction

Snapshot imaging spectrometers based on integral field spectroscopy have recently been developed for the astronomical community providing a powerful new tool capable of collecting a 3D (x, y, λ) datacube in a single integration event [Weitzel 1996, Allington-Smith 1998, Henault 2004, Smith 2006, Content 2006, Tecza 2006, Laurent 2006, Vives 2006]. This simultaneous data collection is crucial for obtaining high fidelity image and spectroscopy information of low light level objects such as distant galaxies, planets, and stars. This technique relies on the use of arrays of high precision miniature optical elements located near a conjugate image plane. These components are very difficult to fabricate and often become the limiting factor in the performance of the system. Our group recently developed a new snapshot

hyperspectral imaging technique called an image mapping spectrometer (IMS) for fluorescence microscopy [Gao 2009]. The IMS relies on the use of an array of high precision, miniature optical elements called an image mapper, which is placed near a conjugate image plane. The requirements for the image mapper differ from those used in astronomy in that the individual elements are much smaller, more densely packed together, and have more complex individual geometries (i.e. compound angles). It is this unique combination of parameters that allow the IMS to provide higher spatial sampling (> 100 x 100 points), diffraction limited resolution, and a compact size making it ideal for use in biomedical applications.

Astronomical groups have developed many fabrication techniques for creating their arrays (called image slicers) which were considered during the development of the image mapper. In general these techniques are all based on two main technological approaches the first, grinding and polishing, and the second, diamond machining. Grinding and polishing approaches have been reported to achieve state-of-the-art optical surface qualities with form accuracies of $\lambda/100$ RMS and $\lambda/20$ PTV and roughness of 0.3-0.4 nm [Vives 2008]. However alignment of the individual elements is a tedious, manual process often susceptible to individual geometrical errors as well as errors from neighboring elements which accumulate as the total image slicer is assembled [Bonneville 2003]. For a large number of elements these errors can become quite significant. Recently, Vives et. al, has reported on a new method for making image slicers which is more cost effective and holds tighter geometrical tolerances with tilt errors < 0.07 mrad PTV and edge quality of 1 to 5 um [Vives 2008]. One disadvantage of this technique however is that the overall number of elements is low ($\leq$60 x 60) limiting its usefulness for applications that require large format imaging like those found in microscopy.

Diamond machining techniques on the other hand are capable of achieving higher numbers of elements (100's – 1000's) with relative ease by cutting directly into a single monolithic substrate. No individual element alignment or assembly is required. By using this fabrication approach high geometrical accuracies, tip-tilt errors of 0.2 mrad, and focus position errors of around 1 micron [Dubbeldam 2006] can be achieved. The main drawback with diamond machining is a lower optical surface quality for the

individual elements with roughness around 10-20 nm rms [Dubbeldam 2006, Schmoll 2006, Todd 2003]. This can decrease the optical throughput and image contrast especially for systems with multiple diamond machined components like those used in astronomy. For the IMS system the image mapper is the only diamond machined component, therefore the decrease in optical throughput due to surface roughness should be minimal. It should be pointed out that post diamond machining techniques such as ductile grinding [Preuss 2006], ion beam polishing [Preuss 2006], and smoothing films [Soufli 2004] are being developed to minimize the roughness although results similar to polishing have yet to be reported. Important work is also being carried out to develop cost effective replication techniques [Schmoll 2006] using diamond machined substrates as the master mold. This is an important development for the image mapper as high volumes and lower costs will be critical for broad acceptance of the IMS in the biomedical field. For all of these reasons diamond machining was chosen as an appropriate fabrication technology for the image mapper.

This paper presents our work toward designing and fabricating these new image mappers based on diamond machining technology. The image mapper design incorporates a large format (285 element) array of high precision multi-tilt (x & y) miniature mirrors that produces a final image matching the size of a single CCD sensor. A detailed design analysis based on both geometric and diffraction based methods is presented in section 2. To fabricate this complex geometry, a new fabrication method is also presented that uses surface shaped tools to cut the individual mirror cross sections. The tools work in a raster fly cutting configuration on a 4 axis (X, Y, Z, C) diamond lathe which precisely controls the orientation and number of mirror facets in the image mapper. This approach represents a significant development as it opens up the possibility to create densely packed, multi-tilt mirror arrays without significant compromise to surface quality or increased fabrication time. To test this approach a 285 element, 25 tilt image mapper is designed, fabricated, and tested. The fabrication setup and process for this image mapper is discussed in more detail in section 7.3 followed by the individual mirror facet characterization in section 7.4. Lastly, the optical performance of the image mapper is evaluated in section 7.5.

7.2. Optical Design

7.2.1.Image Mapping Spectrometer (IMS)

The basic configuration of the IMS system for fluorescence microscopy is shown in Figure 7.1(a). The IMS consists of 6 components. A telecentric relay lens system (1) that transfers the image from the side port of a conventional microscope onto the image mapper (2). The image mapper is composed of miniature mirror facets that reflect thin 1D mapped image lines in different directions depending on the facet's tilt angle. The image mappings are reflected toward a large FOV, high NA telecentric collecting lens (3) that collects and transfers each image mapping to its pupil plane. Similarly tilted image mappings are grouped in different regions of the pupil forming an array of sub-pupils. A dispersing prism (4) is used to spread the spectrum from each sub-pupil in a perpendicular direction to the linear mapping. An array of lenses (5) is placed behind the prism forming an array of sub-images onto a CCD detector (5). Each sub image is composed of a dispersed mapping of the original image. Figure 7.1(b) shows an illustration of what the final image looks like on the detector prior to dispersing. For clarity only 4 out of the 25 grouped sub-images is shown. Each sub-image contains only a selected mapping of the original image with optically void space between each column of linear mappings. Insertion of the dispersing prism spreads the spectrum from each linear mapping into this void region where it is recorded directly by the detector. Simple image remapping techniques can then be used to reconstruct the original object in real-time if needed. This is advantageous for applications which require fast temporal response. In principle, this technique also preserves the throughput (etendue) of the system making it an ideal approach for many low light applications like fluorescence microscopy. A more detailed description of the operating principle of the IMS system is presented by Gao [Gao 2009].

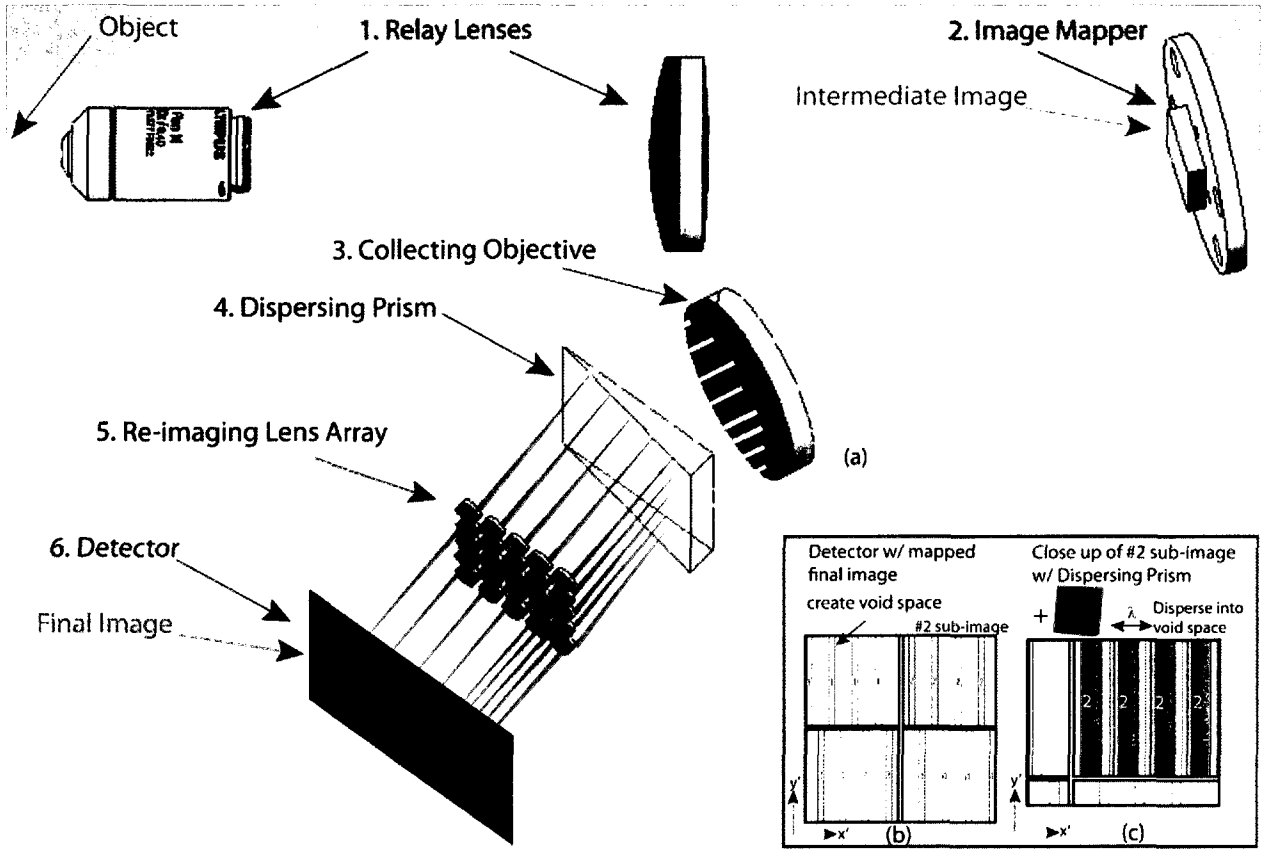

Fig. 7.1- (a) Basic Configuration for the Image Mapping Spectrometer (IMS) System. (b) Illustration of the mapped final image on the detector prior to dispersion. (c) Close up of sub-image #2 with dispersion of the linear mappings.

7.2.2. Image Mapper Geometric Design

One of the most important aspects of the IMS design is its compact size, being able to collect its full 3D (x, y, λ) datacube on a single CCD detector. To accomplish this and still maintain high spatial resolution requires an image mapper with a large number of tiny mirror facets tilted in multiple x- and y- directions. This multi-tilt configuration more efficiently uses a single collecting lens' pupil, creating a closely packed array of sub-pupils (see figure 7.2). This is necessary for forming a final image that matches the size and format of available CCD detectors. This compact design approach does not come without its share of design challenges. There are two main geometric design constraints that limit the information capacity (i.e. volume) of the 3D (x, y, λ) datacube. The first is the size of the collecting lens' field of view (FOV) relative to the length and width of the individual mirror facets. This parameter determines the number of

points or spatial samples in the image. For example, if the FOV = 10 mm and the mirror facets dimensions are 0.1 mm x 10 mm (width and length), then a total of 100 mirror facets reside within the FOV providing a spatially sampled image of 100 x 100. The mirror facets are designed to sample the incident image's point spread function in both directions at the Rayleigh criteria to maintain diffraction limited resolution. Here we assume that the relay optics either match or overfill the FOV of the collecting objective and that the point spread function on the image mapper and CCD camera is also sampled at the Rayleigh criteria. The second main design constraint is the number of tilt angles for the mirror facets. Each tilt angle has a proportional relationship with the spectral sampling of the system. As the total number of tilt angles in both x and y increases the "void" region between the image linear mappings (see figure 7.1(b)) increases creating more space for sampling the spectrum in each linear mapping. The limiting factor for the spectral sampling becomes the NA of the collecting objective which constrains the number and magnitude of the tilts. For an L_x x L_y (x- and y-axis) tilt geometry, the collecting objective must have a minimum $NA_{collect} = NA_{mapper}\sqrt{L_x^{\,2} + L_y^{\,2}}$, where NA_{mapper} is the input NA on the image mapper and $L_{x,y}$ is the number of tilt angles (x or y) as shown in Figure 7.2(a).

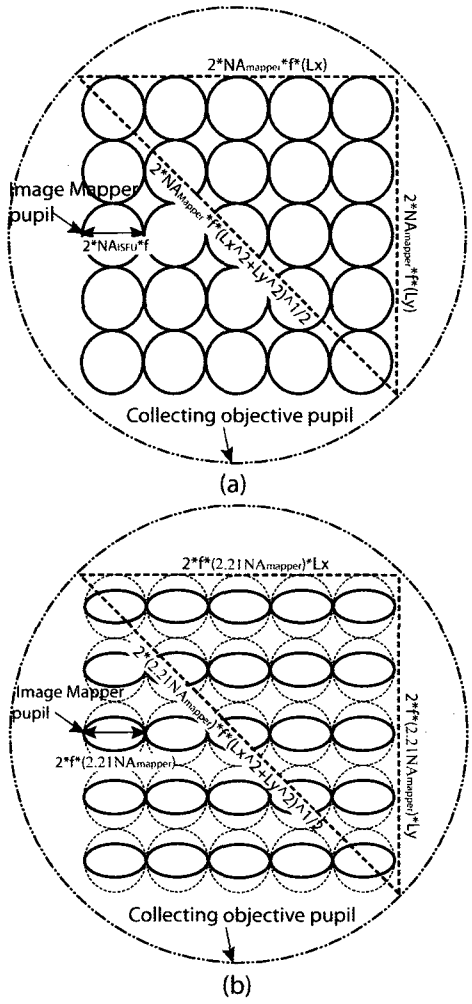

Fig. 7.2- Minimum collecting objective pupil size for the grouped exit pupils based on (a) Geometric and (b) Diffraction models. Pupils in (a) and (b) are not drawn to scale.

As one can see, the collecting objective and image mapper must be designed together to maximize the 3D (x, y, λ) datacube. For example, the system presented by Gao et. al. [Gao 2009] used a commercially available tube lens as the collecting objective, having a FOV of ~ 1 in (25mm) and NA of 0.030. This lens limited the spatial sampling of the system to around 100 as the minimum mirror width fabricated was 160 microns. The number of tilt angles was also limited to a 5 x 5 =25 tilt geometry due to the small NA. Larger format image mappers (> 100) require a collecting objective with a larger FOV and NA. Recently, an objective lens primarily designed for common path stereo-microscopy systems has been

identified as a possible alternative lens. This new collecting objective provides a FOV of 30 mm with a NA = 0.150 as measured, enabling more spatial and spectral sampling.

7.2.3.Image Mapping Diffraction Design

Diffraction effects due to the small and densely packed mirror facets in the image mapper become more prominent for higher sampling IMS systems. This leads to light leaking into neighboring sub-pupils (also called crosstalk) in the grouped pupil plane which will degrade the final image contrast. Therefore, a theoretical model based on scalar diffraction theory was developed for analyzing the effects of diffraction [Barrett 2004] between the entrance pupil plane and the plane of the grouped exit pupils. The results from this model have been used to optimize the image mapper design. The basic configuration between the pupil planes of the IMS (see figure 7.1) can be treated as a standard "4-f imaging system" as illustrated in figure 7.3.

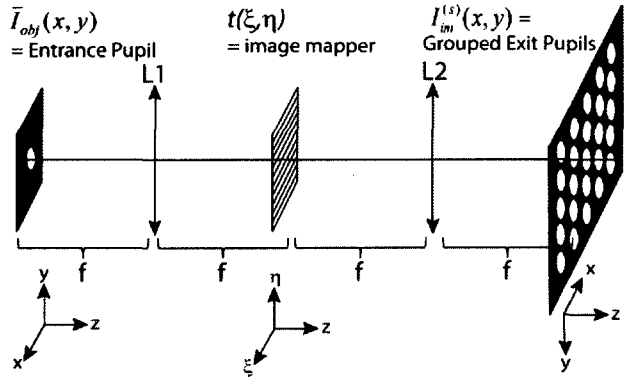

Fig. 7.3 – Theoretical Pupil Diffraction model.

In this model L1 is the second relay lens and L2 is the collecting lens. The following assumptions and simplifications where made: (1) unity magnification (i.e. focal lengths, *f*, are the same) as this only affects the overall scaling of the system not the amount of crosstalk, (2) paraxial approximation, (3) quasi-monochromatic, and (4) a large fluorescent object such that the entrance pupil is incoherently illuminated. This simplification is valid for objects that fill close to the entire field of view of the microscope as is the case for many high magnification applications. For more sparse objects, the model should be adapted to consider partial coherence effects. In addition, a coherent transfer function and point spread function are

presented for simplification of the mathematics and later converted to the incoherent case. These functions are used for relating the different pupil planes and should not be confused with the functions for the object/image planes.

The entrance pupil for this analysis is a circular aperture uniformly and incoherently illuminated by a fluorescent sample (not shown). Under this illumination, the grouped exit pupil's mean irradiance, $\bar{I}_{im}^{(s)}(x,y)$ is then a 2D convolution of the entrance pupil's mean irradiance, $\bar{I}_{obj}(x,y)$ with the pupil's incoherent point spread function, $p_{incoh}(x,y)$.

$$\bar{I}_{im}^{(s)}(x,y) = \bar{I}_{obj}(x,y) * p_{incoh}(x,y) \tag{1}$$

The pupil's coherent transfer function, $P_{coh}(\xi,\eta)$ is the complex amplitude transmittance, $t(\xi,\eta)$ of the image mapper, multiplied by a linear phase factor which will be ignored as it has no consequence on the final result.

$$P_{coh}(\xi,\eta) = \exp(4ikf)t(\lambda f\xi, \lambda f\eta) \tag{2}$$

where ξ, η are the spatial frequencies, k is the wave number equal to $2\pi/\lambda$, and f is the focal length of the lens. The transmittance function of the image mapper is:

$$t(x,y) = \underset{(I)}{rect\left(\frac{x}{w},\frac{y}{l}\right)} \underset{(II)}{\sum_{j=1}^{M}\sum_{k=1}^{N}\exp\left[i2\pi\left(\alpha_j x + \beta_k y\right)\right]} \underset{(III)}{\sum_{m=-\infty}^{\infty} rect\left(\frac{x - mc - (j+k-2)b}{b}\right)} \tag{3}$$

Part *(I)* of this equation defines the overall size of the image mapper where w and l are the width and length respectively. Part *(II)* defines the linear phase introduced by each individual mirror facet in the image mapper. This phase is two dimensional where α_j and β_k are equal to twice the tilt angle ($\alpha_j = 2\theta_x$, $\beta_k = 2\theta_y$) of the mirror facet due to reflection. Part *(III)* defines the width, b, of the individual mirror facets, and c is the period equal to $c = N$ x M x b. The $(j+k-2)$ term corresponds to a lateral shift in the origin of the repeating mirror facets with similar tilts. For this model the image mapper is treated as a thin phase object even though it is placed at a 20 degree angle with respect to the incoming light which creates

an axial (z-) position range of ± 3.6 mm. This is due to the large depth of focus, DOF, of the incident image which is +/- 4.3 mm based on the Rayleigh depth of focus criteria [Pluta 1988]. For designs in which the image mapper exceeds the depth of focus modifications to the theory will be required.

The pupil's coherent point spread function, $p_{coh}(x,y)$ of the system is the Fourier transform of the coherent transfer function which for our system becomes:

$$p_{coh}(x,y) \propto \underbrace{\operatorname{sinc}\left(\frac{wx}{\lambda f},\frac{ly}{\lambda f}\right)}_{(I)} * \sum_{j=1}^{M}\sum_{k=1}^{N}\sum_{m=-\infty}^{\infty} \underbrace{\exp(i\phi_{j,k})}_{(II)} \underbrace{\operatorname{sinc}\left(\frac{bx}{\lambda f}\right)}_{(III)} \underbrace{\delta\left(x-\frac{m\lambda f}{c}\right)}_{(IV)} * \underbrace{\delta\left(x-\alpha_j\lambda f, y-\beta_k\lambda f\right)}_{(V)} \quad (4)$$

Part *(I)* is a 2D sinc function that is convolved with the rest of the equation. This sinc function is the resulting diffraction pattern created by the image mapper's total length and width (l x w). Due to the relatively large size of l and w the associated diffraction pattern is small with the first zero position of the sinc function occurring very close to its center at $\lambda f/w$ or $\lambda f/l$ which is on the order of a few microns for our typical system parameters (l & w = 20mm, λ=0.5x10^{-3} mm, f=90 mm). Part *(II)* of the equation is a linear phase factor introduced by the shift in the x direction for each set of repeating similarly tilted mirror facets (i.e. the same j + k values), $\phi_{j,k}= 2\pi c(j+k-2)$, and should have little effect on the system. Part *(III)* is the result of diffraction from the individual facet widths, b, and has a significant effect with the first zero occurring at $\lambda f/b$ which is on the order of a millimeter for our typical system parameters. This sinc function acts as an envelope for a sampling comb function described in Part *(IV)* which has of period of $\lambda f/c$. As c increases (i.e. more tilt angles (M, N) or wider facets, b) the sample spacing decreases and there are more diffraction orders within the envelop. The last part of this equation, Part *(V)* is a convolving 2D delta function which shifts these diffraction orders in both the x and y directions based on the tilt of the facet (α_j, β_k). The incoherent point spread function $p_{incoh}(x,y)$ is the squared modulus of the coherent point spread function, $p_{coh}(x,y)$ which removes all the phase dependence.

$$p_{incoh}(x,y) = A_c\left|p_{coh}(x,y)\right|^2 \quad (5)$$

Based on this model it is apparent that the x-axis is most susceptible to crosstalk between the sub-pupils due to diffraction effects caused primarily by the sinc function in equation 4, part (IV). This sinc is the result of diffraction from the individual mirror facet's width and spreads light into the x- direction of the pupil array. As the width gets smaller, more light spreads out this can overlap into adjacent pupils creating crosstalk between systems. This effect is unaccounted for in the simple geometric consideration.

7.2.4.Crosstalk analysis

To quantify the amount of crosstalk between neighboring pupils in the x direction we simulated a worst case irradiance profile of a single sub-pupil (see Figure 7.4(a)) in which the sampling comb function (part *III* of equation 4) samples every point of the sinc envelop. A circular mask of equal diameter to the original pupil is translated across this diffraction pattern in the x-axis (see Figure 7.4(b)) simulating different positions for a neighboring sub-pupil. Crosstalk is defined as the irradiance falling inside of this mask. Simulation results show that the x position at which the neighboring sub-pupil has only 1% of the adjacent pupil's irradiance is

$$x_{1\%} \sim \frac{2.7\lambda f}{b} \tag{6}$$

The mirror facet tilt angle corresponding to this x position is then:

$$\alpha_{1\%} = \frac{x}{f} \sim \frac{1.35\lambda}{b} \tag{7}$$

This relationship is only valid for Rayleigh sampling where $b=0.61\lambda/NA_{IMAGE\ MAPPER}$. For conditions above Rayleigh sampling the crosstalk will decrease from this value. Conversely, below Rayleigh sampling the crosstalk will increase. Due to this diffraction effect the minimum NA for the collecting objective must increase ~2x above the geometric limit. Assuming uniform spacing between the sub-pupils the resulting minimum NA for the collecting objective becomes:

$$NA_{\min collect} = 2.21 NA_{mapper}\sqrt{L_x^{\,2} + L_y^{\,2}} \tag{8}$$

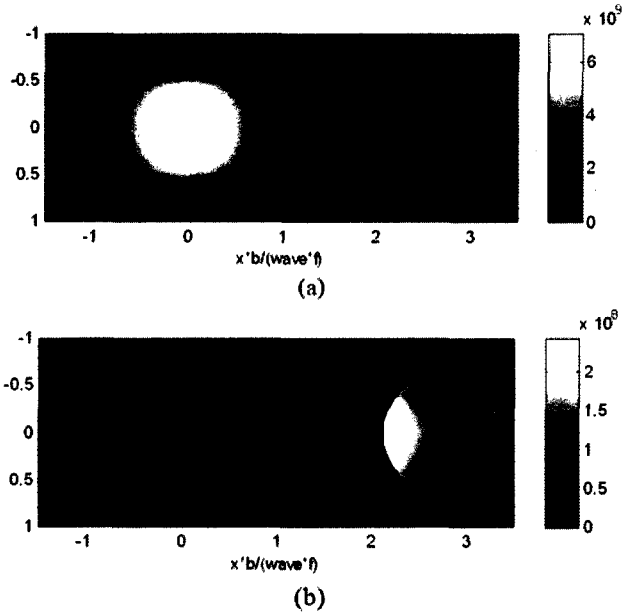

Fig. 7.4 – (a) Simulated irradiance at a single sub-pupil created by diffraction at the image mapper. (b) Irradiance from one pupil entering a neighboring sub-pupil (defined as crosstalk).

7.2.5. Image Mapper Complete Optical Design

Taking into account both geometric and diffraction based models, we have developed an image mapper for use in a large format IMS system capable of acquiring a 3D (x, y, λ) datacube of 250 x 250 x 60 while utilizing a new collecting objective identified in section 7.2. The image mapper's critical optical design features are listed in Table 7.1.

Table 7.1 – Large format image mapper design parameters

Parameter	**Value**
Length, l	20 mm
Width, w	20 mm
Mirror facet width, b	75 um
# of x-tilt angles, Lx	5
# of y-tilt angles, Ly	5
x-tilt magnitude, α_i	0.02 rad.
y-tilt magnitude, β_k	0.04 rad.
NA_{ISFU}	0.004
$NA_{COLLECT}$	0.150
Material	Kobe Al

The collecting objective for the system meets the minimum NA requirement established by the diffraction model ($NA_{min\ collect}$ = 0.063, and $\alpha_{1\%}$ =0.009 (λ=500nm)). The number of mirror facets = 20mm /.075 mm = 267 facets meet the spatial sampling requirement (250 elements) while remaining within the

FOV constraint of the collecting objective. Finally, the input NA from the relay optics creates a spot size diameter of 153 microns which can be sampled by the image mapper's 75 micron wide facets at the required Rayleigh sampling criteria. Note that the spot size is defined as the diameter between the first zeroes of the resulting Airy Disk diffraction pattern for a single point in the object. In addition to the optical design of the image mapper, manufacturing considerations also play an equally important role in the development process and is discussed in the next section.

7.3. Optical Fabrication

7.3.1.Raster fly cutting

The three main configurations for high precision diamond machining are turning, milling, and raster fly cutting. Diamond raster fly cutting is the most appropriate approach for creating thin, straight, high aspect ratio features such as mirror facets for the image mapper. In diamond raster fly cutting the tool rotates about the spindle and scoops material out of the workpiece (i.e. image mapper) see figure 7.5(a). For this example, the workpiece moves up and down in the Y axis to create a thin mirror facet. To create adjacent facets the workpiece then steps over in the Z axis as shown in figure 7.5(b). This is repeated down the length of the image mapper until the entire surface is cut. A close up of the tool cutting the workpiece (figure 7.5(b)) illustrates how adjacent mirror facets with different tilt angles can be cut by the diamond tool. Here the different facet angles correspond to height variations in the workpiece at a specific X-Z plane.

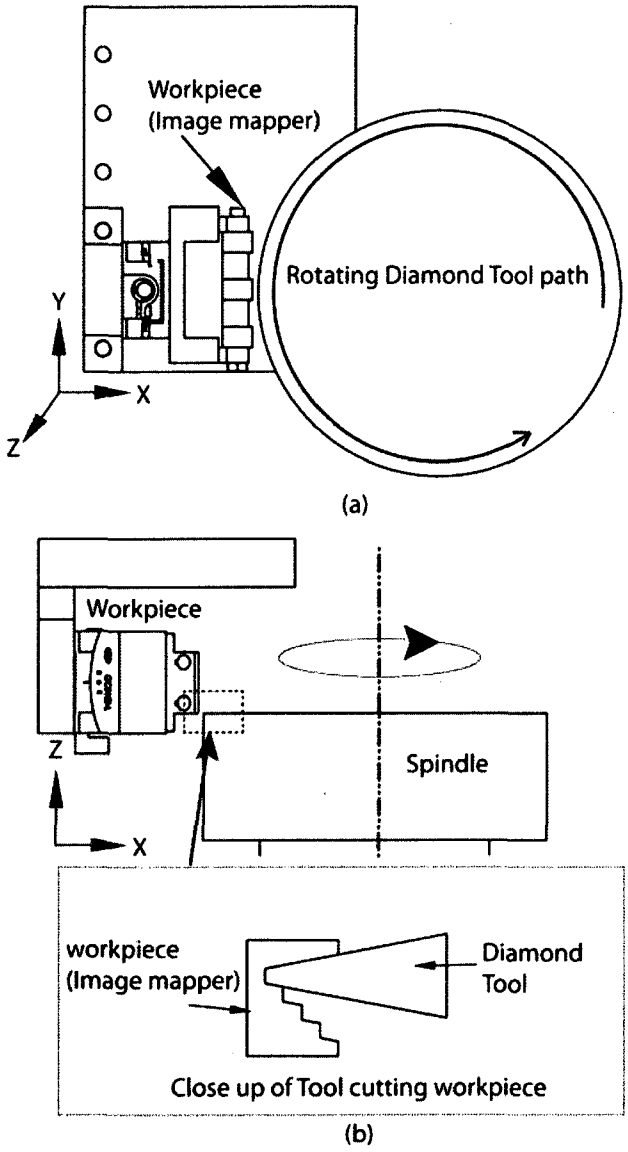

Fig. 7.5 – (a) Front view for fabrication of an image mapper using diamond raster fly cutting technique. (b) Top view of an image mapper during fabrication. The close up shows the diamond tool cutting the facet profile into the workpiece.

Other groups [Dubbeldam 2006, Preuss 2006] have used raster fly cutting to produce much larger mirror facets, however, compact, higher sampling (>100 elements) image mappers require much smaller mirror facets. By scaling down the width of the facets, tools that are pre-shaped for the cross section profile of the mirror facets can be used. This has several advantages including: a significant reduction in fabrication time, program simplicity, a more densely packed mirror array, and high relative geometric accuracy independent of machine precision for axes perpendicular to the cutting direction. The

disadvantage of this approach is that there is little ability to correct for errors in the cross section of the mirror facet due to the tool shape, chips and/or other defects. This makes the quality of the diamond tools a critical component in the fabrication process.

7.3.2. Tool Design

There are several design parameters that must be considered for the surface shaped diamond tools such as: included angle θ, primary side clearance angle α, primary tip clearance angle ϕ, top rake angle β, tool width, maximum depth of cut, edge quality, and material. These geometric parameters are illustrated in figure 7.6(a) and 7.6(b).

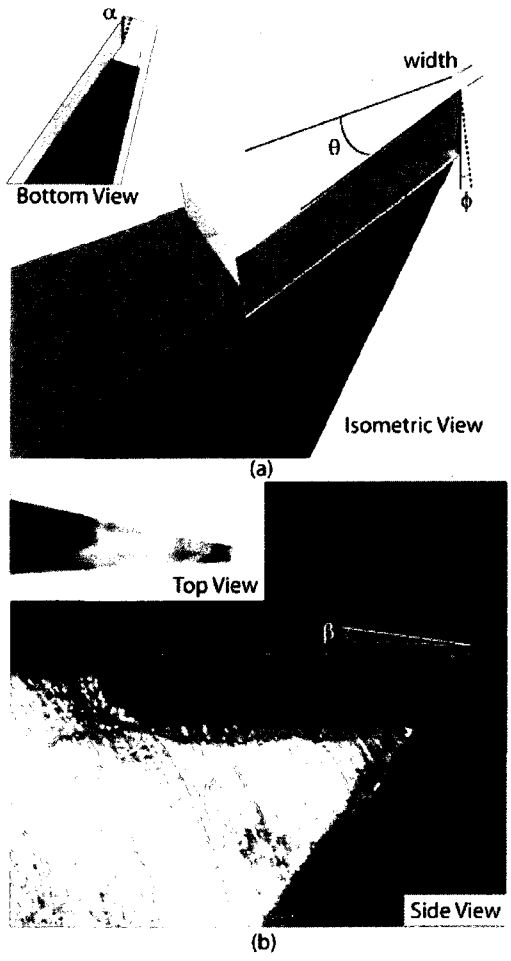

Fig. 7.6 – (a) Drawing of a flat bottom surface shaped tool for fabrication of the image mapper with some of its critical design parameters labeled. (b) Actual fabricated tool with a 75 micron wide flat bottom profile at tip of tool. The location of the rake angle, β, is also shown in this picture.

The flat bottom tool tip width and the maximum depth of cut are the key design parameters of the tool as they are determined by the optical design of the system. The tool tip width becomes the width of the mirror facet while the maximum depth of cut determines the largest achievable y-axis tilt. Proper selection of the other tool parameters is critical for optimum cutting performance, durability, tool manufacturability, and overall cost. It is best to consult with the tool manufacturer to determine the various design tradeoffs for each parameter(s) as they relate to the overall design. We have developed three different tool designs for our image mappers. These tools were manufactured by Chardon Tool, Chardon, Ohio, USA. Table 7.2 lists the different design specifications for each tool.

Table 7.2 – Surface shaped flat bottom tool design parameters

Parameter	**Tool #1**	**Tool #2**	**Tool#3**
Included Angle, θ, (deg)	20±0.5	20 ±0.5	**5 ±0.5**
Side clearance angle, α (deg)	3	3	3
Tip clearance angle, ϕ (deg)	6	5	5
Top rake angle, β (deg)	0	0	0
Tool Tip Width, (μm)	150±15	**70 ±7**	70±7
Max. Depth of Cut, (μm)	500	300	300
Edge quality	750 X	750 X	750 X
Material (Diamond)	Synthetic	Synthetic	Synthetic

Tool#1 was the first tool used to fabricate the 100 element image mapper used in snapshot imaging spectrometer for fluorescence microscope [Gao 2009]. This tool has a 160 micron wide flat bottom tip and was used to create a square shaped image mapper with a side length of 16 mm. In the pursuit of a large format IMS system which still resides within the same FOV, a 75 micron flat bottom tool (Tool#2) was developed. This tool increases the number of mirror facets to ~ 285. The last tool design (Tool#3) is also 75 microns wide but has a reduced included angle to minimize the effects of edge eating. The edge eating effect is due to height differences from adjacent y tilt facets. This fabrication related effect is illustrated in figure 7.7(a) and shown at the edge of a prototype image mapper cut using tool#2.

The dark shaded regions in figure 7.7(a) indicate where the additional material is removed due to the included angle of the tool. Edge eating is most significant at the sides of the image mapper where the

height difference between adjacent y-tilt facets is greatest. The edge eating effect is less significant for larger mirror facets; however, for smaller facets can become quite dramatic reducing the surface area of the facets by over 60% at the edges as demonstrated in figure 7.7(b). Edge eating decreases the throughput of the system and also the image contrast.

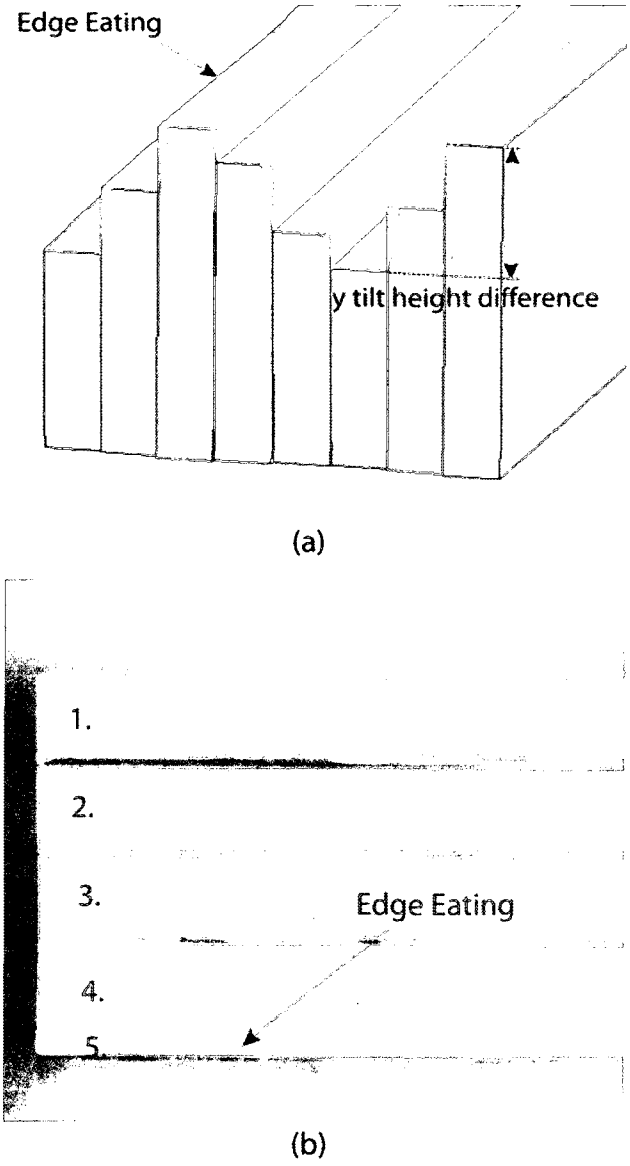

Fig. 7.7 – (a) Illustration of the edge eating effect due to the y tilt height differences at the edge of the image mapper. The shaded regions indicate where excess material is removed. (b) Image of an actual prototype image mapper with obvious edge eating on mirror facet #5.

7.3.3.Edge Eating Reduction

The design of the image mapper must be optimized for the surface shaped tool geometry to minimize the edge eating effect. This is accomplished three ways, first, the y-tilts are staggered to minimize the step height difference between neighboring facets. Figure 7.8(a) shows a non-optimized configuration with a large step height difference between repeating blocks of y-tilt only mirror facets. Figure 7.8(b) shows the improved configuration in which the y-tilts are staggered to minimized the step height difference of the repeating blocks.

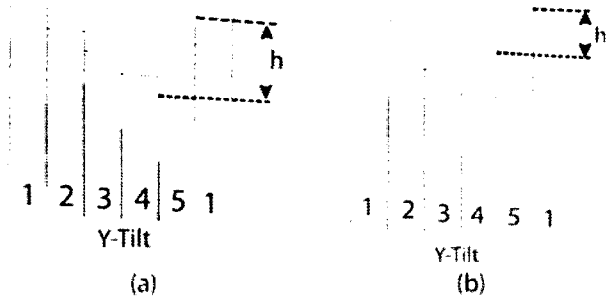

Fig. 7.8 – (a) Non-optimized sequential y-tilt layout with large y tilt height difference, h. (b) Optimized staggered y-tilt image mapper layout with minimum y-height difference.

Second, the x-tilts are grouped on the y-tilts which decrease the edge eating effect by 4x only affecting the 1st and 5th x-tilt facets. Figure 7.9(a) shows an example of a staggered y-tilt design but with no grouping of the x-tilts. In this configuration, every facet experiences some edge eating effect. In contrast by grouping the x-tilts (figure 7.9(b)) on the y-tilts the total number of facets with edge eating is significantly decreased.

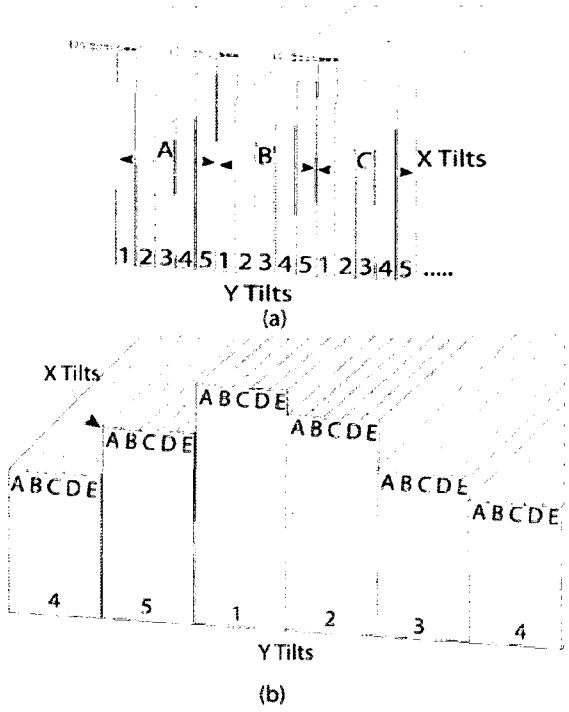

Fig. 7.9 – (a) Non grouped x tilts illustrating an increased edge eating effect. (b) Grouped x-tilts (A, B, C, D, E) on each y tilt (1, 2, 3, 4, 5). Edge eating only occurs at the boundary between x-tilts A and E.

Third, the orientation of the x tilts in a concave (figure 7.10) profile as opposed to other orientations (convex) further reduces the effects of edge eating.

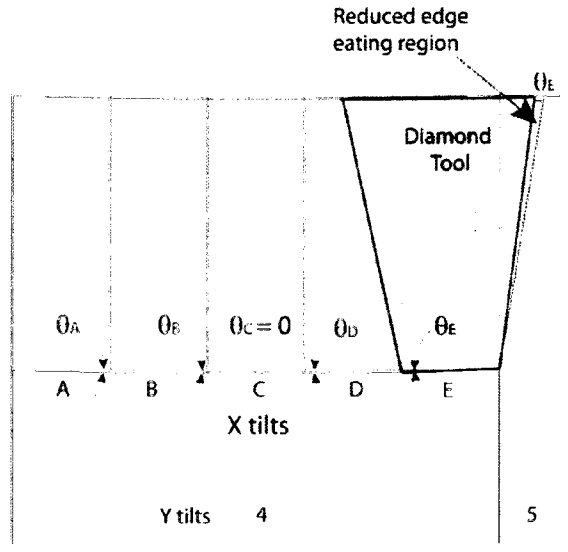

Fig. 7.10 – Concave distribution of x-tilts further reduces the effect of edge eating at the interface regions between y-tilts.

7.3.4.Fabrication setup and machining parameters

For fabrication of the image mappers a high precision CNC 4-axis diamond lathe (Nanotech 250UPL) is used. This machine has 200 mm of travel for each axis (X, Y, Z) with nanometer level precision. The workpiece is mounted on two stages with Y and Z axis movement while the spindle and diamond tool are mounted on the X axis stage see figure 7.11(a). The mirror facets are cut by moving the workpiece up and down in the Y axis. Tilts in the Y direction are achieved by moving in both the X and Y directions while cutting each facet. After cutting a facet the spindle and tool moves away from the workpiece, rewinds, and begins cutting the next facet. The workpiece also steps over in the z axis by the tool width prior to cutting the next facet. The x-tilts are obtained by mounting the workpiece to a goniometer with its cutting surface coincident with the goniometers axis of rotation see figure 7.11(b).

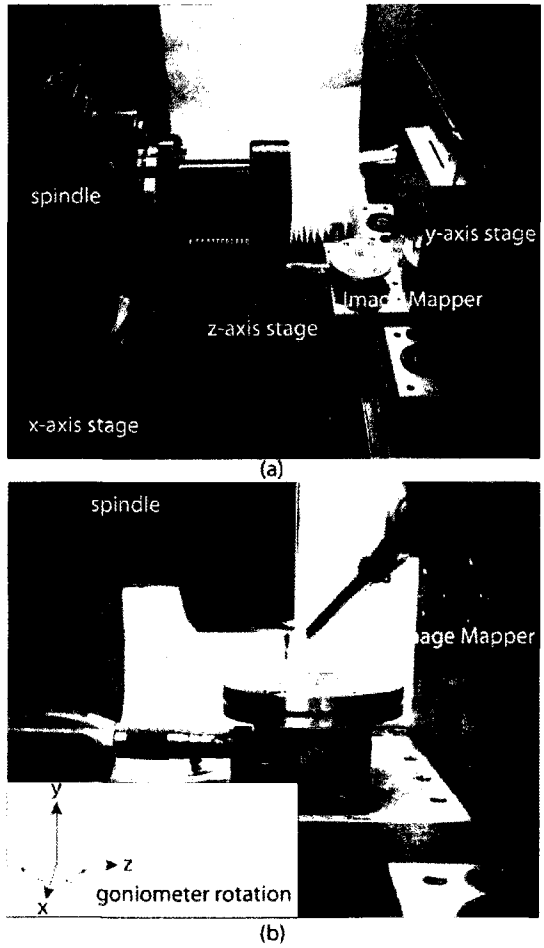

Fig. 7.11 – (a) Picture of Nanotech 250 UPL Machine with axis labeled. (b) Close up of goniometer fixture used to rotate the image mapper for fabrication of x-tilt mirror facets.

Due to the manual rotation of the goniometer, x-tilts are fabricated at the same time. When it is finished the operator adjusts the goniometer to the next x-tilt and the process is repeated until all mirror facets are fabricated. Y height compensation factors are applied for the different x-tilts. For large x-tilt angles, z-axis compensation factors are also used to compensate for the cosine effect.

The cutting parameters for the image mapper are listed in Table 7.3. In general, a rough cut is performed initially to get the different mirror facets into the aluminum substrate. After this step, a fine cutting program is used to clean up the image mapper producing the best surface roughness and removing cosmetic imperfections such as metal flaps, chips, and other debris.

Table 7.3 – Cutting parameters for image mapper.

Parameter	**Rough Cut**	**Final Cut**
Feedrate (mm/min)	30	30
Depth of Cut (microns)	40	5
Spindle speed (rev/min)	2800	2800
Number of passes	11	1

Figure 7.12(a) shows a picture of the final large format (250 element) image mapper fabricated using tool #3. Figure 7.12(b) shows a close up side view of the image mapper showing the excellent alignment of the facets. The x-tilt grouping and concave orientation are easily observed as well as the staggered y-tilts.

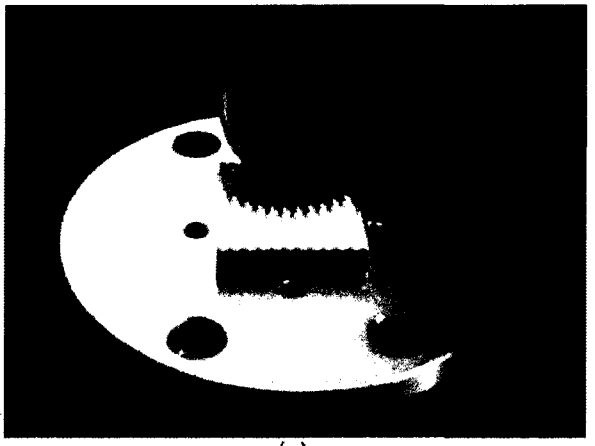

(a)

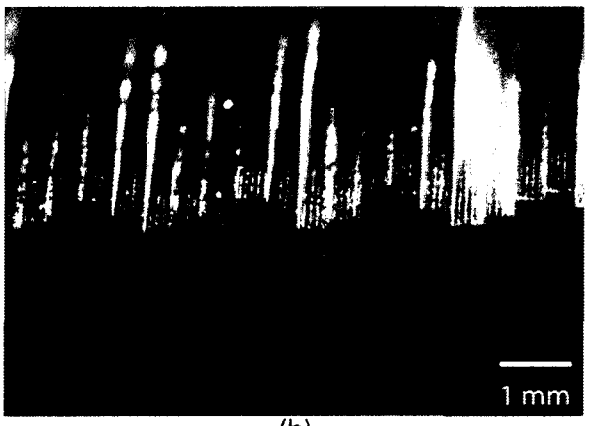

(b)

Fig. 7.12 – (a) Actual picture of the large format image mapper (250 mirror facets) next to a US Quarter for size comparison. (b) Close up side view of the image mapper showing the excellent alignment of the facets.

7.4. ISFU Component Characterization

7.4.1.Geometric Errors

The mirror facet tilts and widths are measured using a white light interferometer (Zygo NewView). Before component testing, the image mapper is placed on the interferometer's motorized 4-axis stage (X, Y, θ_x, θ_y) and adjusted to align the reflected light from the zero tilt (x- and y- axis) mirror facet of the image mapper with the optical axis of the system. Any residual tilt is recorded and subtracted from the other facet tilt measurements. A 10x Mirau Objective with a 1.0x field lens is used to collect the data. Ten measurements were taken for each tilt position and averaged together. Table 7.4 shows the final results comparing the measured values to the designed values.

Table 7.4 – Comparison of image mapper tilt designed and measured values.

x-tilt (α's)	y-tilt (β's)	Ideal (rad.)	Measured (α's)	Measured (β's)	Error (α's)	Error (β's)
α1	β1	+0.020	+0.020	+0.020	0	0
α2	β2	+0.010	+0.098	+0.010	-0.002	0
α3	β3	0	-	-	-	-
α4	β4	-0.010	-0.010	-0.010	0	0
α5	β5	-0.020	-0.021	-0.020	+0.001	0

The results from this study demonstrate an excellent agreement between the ideal 'designed for' tilt values and those actually measured. The largest tilt error was -2 mrad for the x-tilt (α_2=0.010 rad.) with most of the tilts having errors of less than 1 mrad.

Next, the width of each facet was measured by taking a cross section profile across its surface at the left, center, and right edge of the facet. Figure 7.13 shows typical results obtained from these measurements. During the fabrication process, a 5 micron overlap was introduced to remove a thin metal flap between adjacent facets. This overlap changes the designed width of the facets from 75 microns to between 70-65 microns depending on facet position. For the center x-tilts (2-4) the measured widths are within +/- 1 micron of the 70 microns; however, for the edge positioned x-tilts (1 & 5) this changes from 50-70 microns depending on the y-tilt. The highest facet due to the y-tilt will be the thinner due to this overlap as well as some edge eating this shown in the 2D intensity maps in Figure 7.13.

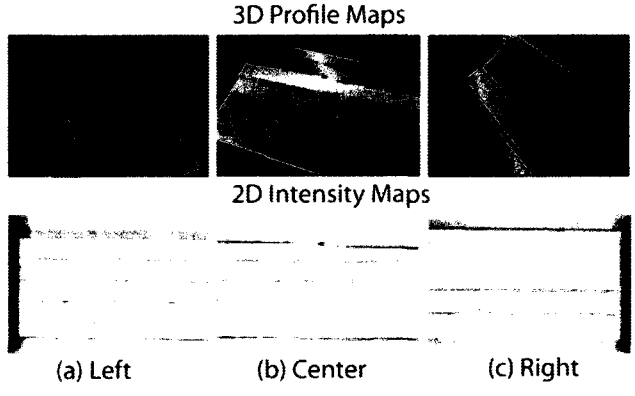

Fig. 7.13 – White light interferometer surface profile measurements of the individual mirror facets in the large format image mapper taken at the (a) left edge, (b) center, (c) right edge of the component.

7.4.2. Surface form errors

In the development of the image mapper, each mirror facet is designed to be flat with no optical power. However, due to imperfections in the cutting tools, the actual surface has some form errors across the facet width direction. These errors add optical power to the reflecting surface that alters the shape of the grouped pupils. For the large format image mapper fabricated using tool#3 there is a depression (depth ~0.24μm) on the left side of the facet (see Fig 7.14). Light reflected from the right edge (length ~15μm) of this region will broaden the pupil on one side, forming a comet shape.

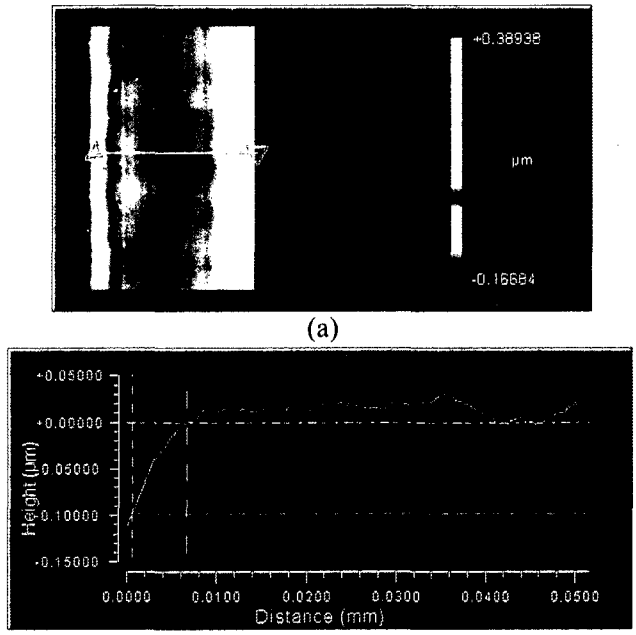

Fig. 7.14 – Facet surface error in facet width direction. (a) Shows the single facet white light interferometer image under 50× objective, 1.3× field lens. (b) Is the cross-section profile for the facet in (a).

7.4.3. Roughness errors

The roughness of the mirror facet surfaces reduces the final image contrast and throughput of the image mapper. To quantify this effect, we used a white light interferometer with a 50x Mirau Objective and 2.0x field lens. Figure 7.15 shows a typical roughness result obtained from a single facet. For this fabrication method, the tool imperfections create lines along the length of the facets.

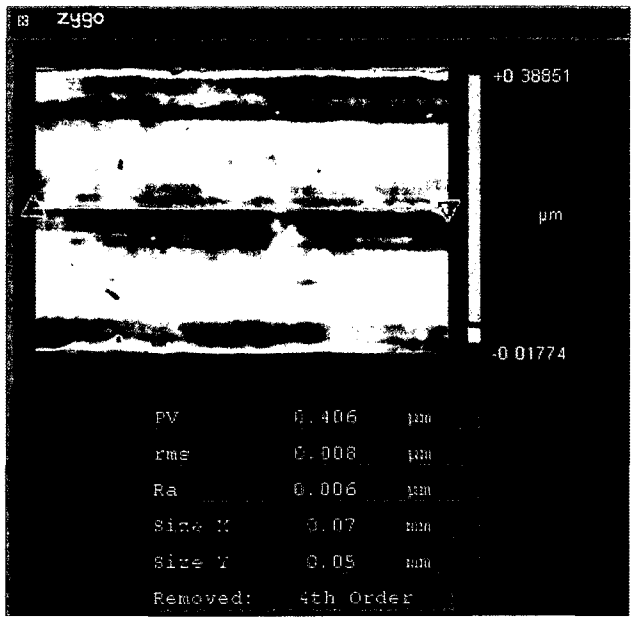

Fig. 7.15 – Typical roughness results obtained from a large format image mapper fabricated using a 75 micron wide surface shaped diamond tool.

To gain a more statistical estimate of the image mapper's surface roughness, ten randomly selected facet surface regions were measured and found to have an average rms roughness of 5.3 +/-1.2 nm. This value is similar to what was previously reported by Gao [Gao 2009] for the larger facets (160 microns wide) and those reported by astronomical groups using other diamond machining techniques. The optical throughput of the image mapper is estimated using an approach similar to the one reported by Dubbeldam et. al. [Dubbeldam 2006], where it is assumed that the image mapper's throughput is dependant only on the total integrated scatter from the mirror facets surface and material reflectivity

$$\eta(\lambda) = R(\lambda)\left[1-\left(\frac{4\pi\bar{\sigma}_{RMS}}{\lambda}\right)^2\right] \tag{9}$$

where $\bar{\sigma}_{RMS}$ is the average rms surface roughness, R(λ=500nm) ~ 99% (aluminum substrate) is assumed for the entire visible spectrum, The image mapper's throughput, η is estimated to be ~ 97% which is still high compared to other snapshot techniques[Ford 2001, Wagadarikar 2009].

7.5. Image Mapper System Level Tests

The final test for the large format image mapper is to examine its ability to redirect light from similarly tilted facets to specific regions in the pupil. The 'ideal' image mapper would create a high contrast pupil image with low scattered light between the separate sub-pupils and sufficient spacing between the pupils to avoid overlap due to diffraction effects. A "4-f system" test setup was constructed using a large FOV, high NA objective as the collecting objective to evaluate the image mapper's performance. A schematic and actual picture of the test setup is shown in figure 7.16 (a) and (b) respectively.

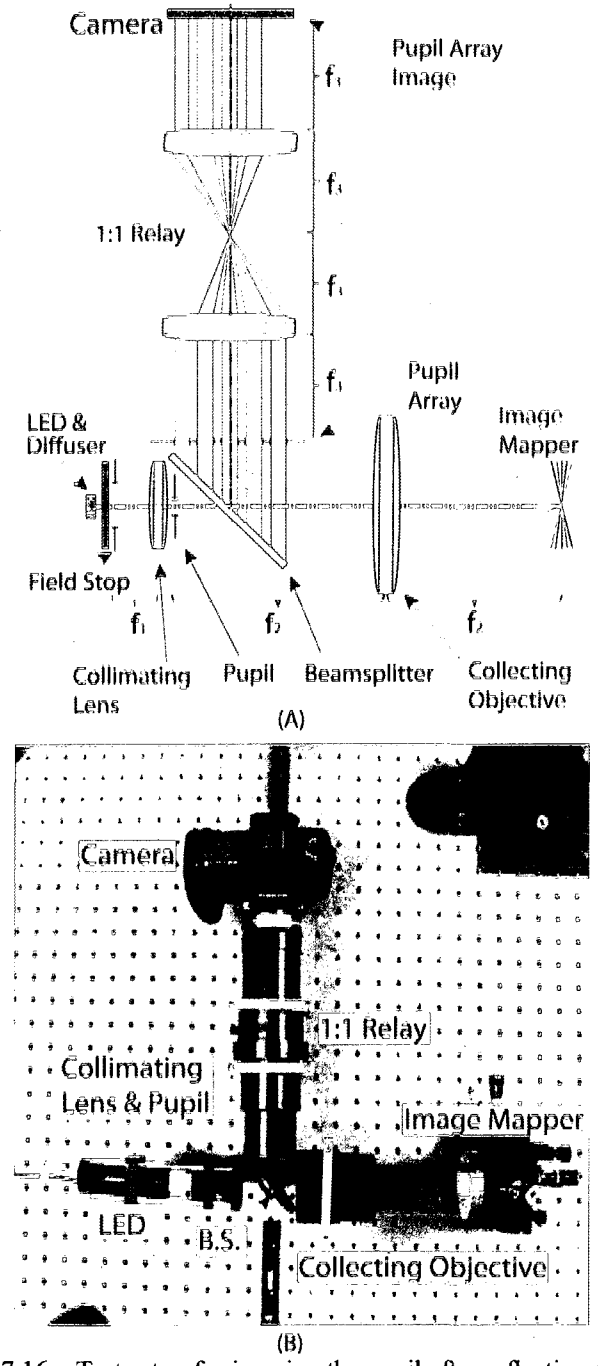

Fig. 7.16 – Test setup for imaging the pupil after reflection from the image mapper, (a) schematic drawing, (b) labeled picture of the actual setup.

A green LED (λ_D=530nm) and diffuser provide uniform incoherent illumination for the setup. Light from this source is then collimated by a collimating lens and refocused on the image mapper by the collecting objective. An adjustable field stop is placed behind the diffuser to adjust the area illuminated on the image mapper. A 600 micron pinhole is used as the input pupil (i.e. aperture stop) for the system.

An image of the pinhole at the image mapper has a diameter of 183 microns which is sampled by the mirror facets above the Rayleigh criteria. Light reflected from the image mapper travels back through the collecting objective and is reflected out of the illumination path by a 45:55 pellicle beamsplitter forming the array of sub-pupils. The sub-pupil array is relayed onto a color CMOS camera using a telecentric 1:1 relay where it is digitally recorded. Figure 7.17(a) shows an image of the actual sub-pupil array. A simulation of a sub-pupil array produced by an 'ideal' image mapper as described by equation 4 is shown in figure 7.17(b). As one can see this there are differences between the ideal and experimental results. One of the major sources of this difference is the non perfectly flat shape of the facets as was assumed in the 'ideal' model. Taking into account the surface form error, an "as fabricated" model was developed as shown in figure 7.17(c). This sub-pupil array has a much better correlation to the experimental sub-pupil array. To model the surface form error, two second order polynomials were fit to the WLI data shown in figure 7.14(b). One polynomial was fit to the first region of the facet (0 mm to .010 mm) and the other polynomial was fit to the second region (0.010 mm to 0.055 mm). The entire surface form error and the WLI data used to generate the surface are shown in figure 7.17(d). Cross section profiles in both the y- and x-axis for both models and the experimental results are shown in figures 7.17(e) and 7.17(f) respectively. For the y-axis, the theoretical and experimental results have excellent agreement with both the pupil diameters and locations. In the x-axis (Figure 7.17(d)) the pupil locations are also in good agreement with the model, however, the experimental cross-talk is still higher than the "as fabricated" model which predicts a new crosstalk level of ~5.4%. This increase is most likely due to other fabrication related imperfections such as facet width variations due to edge eating and tool overlap and facet surface roughness. It is interesting to note that the model generated a similar asymmetric distribution of light in the pupil as is observed in the experimental results. This suggests that the surface form contributes significantly to this effect. In addition, the individual pupils have also become more elongated due to the surface form error which is also present in the experimental results.

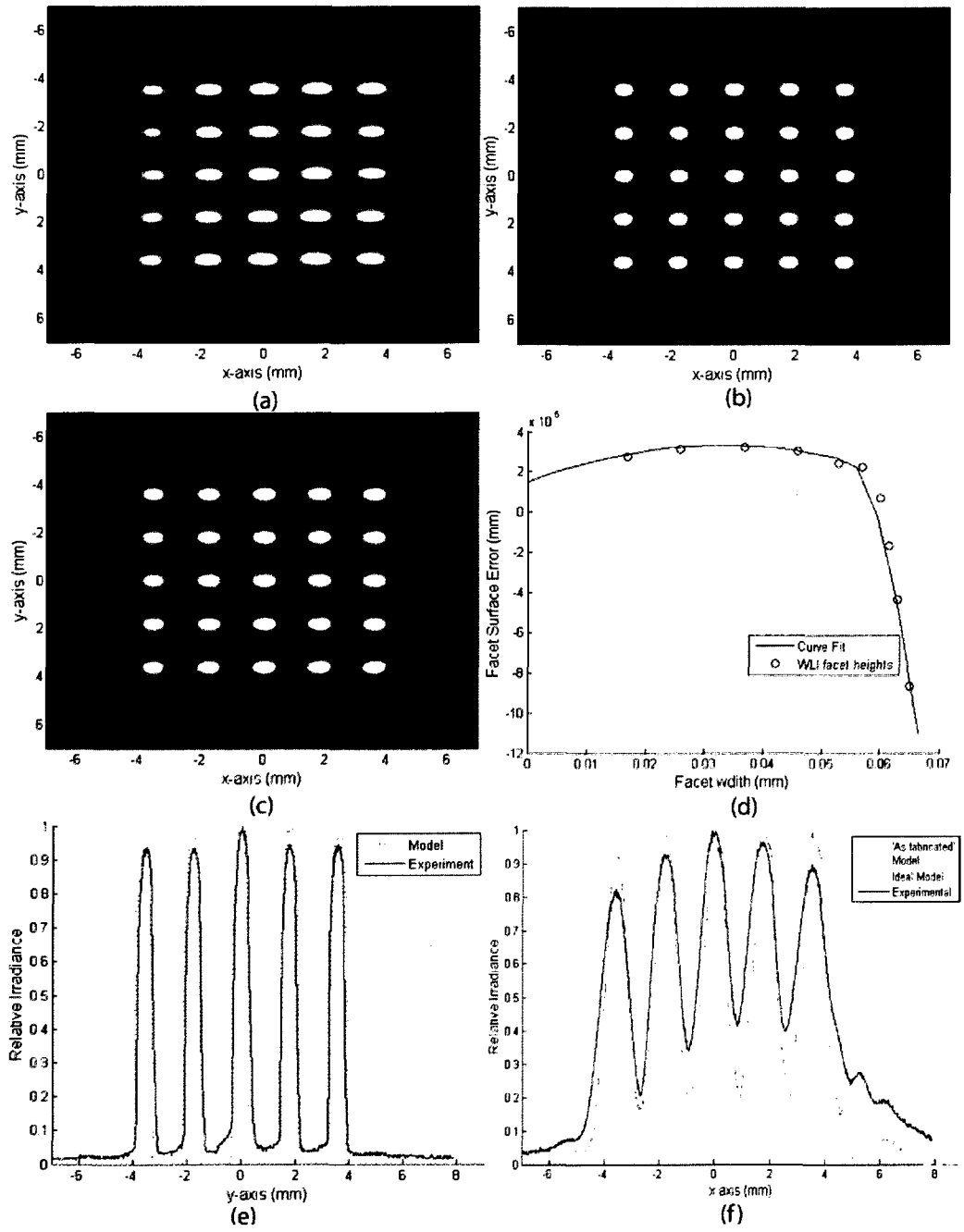

Fig. 7.17- Grouped sub-pupil array comparison between measured and theoretical results: (a) experimental image of the grouped pupils, (b) 'ideal' model, (c) 'as fabricated' model incorporating the surface form error described in section 4.2. (d) Cuve fit of the surface from error used in part (c). Cross sections from both models and experimental results in the (e) x-axis and (f) y-axis.

To quantify the amount of cross-talk between the different sub-pupils generated by the real image mapper, the test setup in figure 7.16 was modified. The 1:1 relay was replaced with a 1:4 relay to increase the size of the pupil making it easier to align and aperture using an adjustable iris. A lens with a

f=100 mm was placed right behind the iris to form a sub-image of the image mapper. This sub-image only contains light from mirror facets with no tilt in either the x- or y- directions (0,0 tilt). This position was chosen as it contains the largest amount of crosstalk and should be a worst case scenario. Figure 7.18(a) shows a close up of two (0,0 tilt) mirror facets. An irradiance cross section profile through the bottom mirror facet is displayed in figure 7.18(b) along with the theoretical cross-section profile. The difference between the two curves is assumed to be caused primarily by crosstalk from neighboring facets. This cross talk is estimated by the ratio of the areas under the cross-section profiles and is found to be ~10% which is higher than the designed value of 1% but much closer the "as fabricated" model which predicted a value of ~ 5%. Note this value is the total contribution from neighboring facets on either side of the primary facet. It is assumed that this crosstalk is consistent over the entire sub-image although further testing is still required.

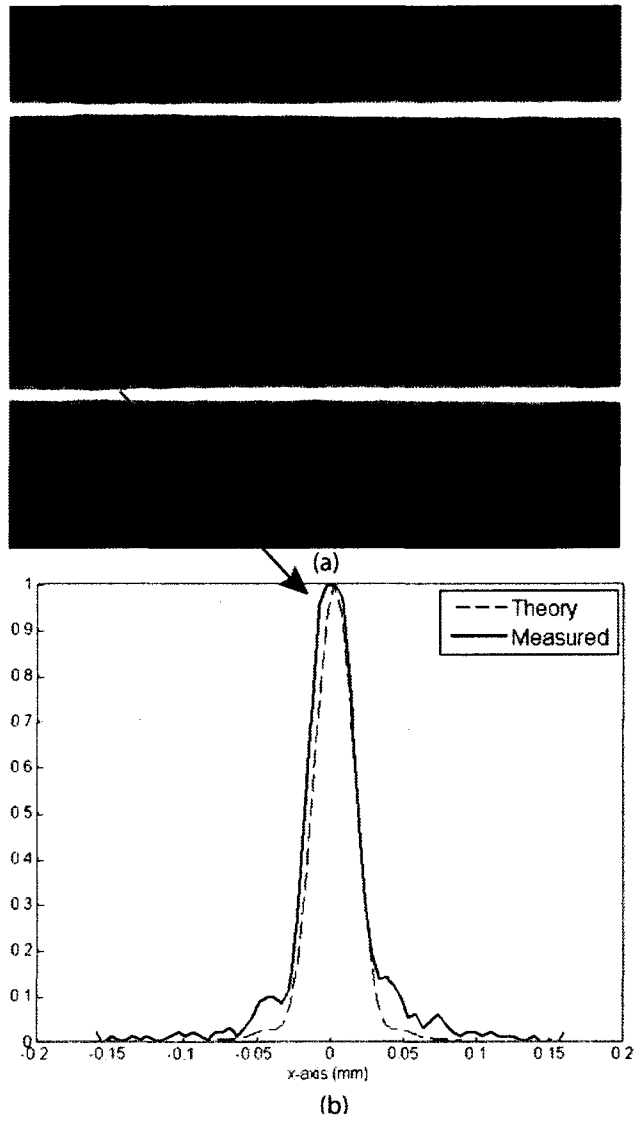

Fig. 7.18- (a) Close up image of the image mapper from the center pupil with only (0,0) tilts for (x,y). (b) Cross section irradiance profile of the top facet showing ~10% crosstalk from the neighboring facet.

Significant work has been undertaken to minimize the effects of crosstalk between adjacent sub-imaging systems. There are two main reasons for removing crosstalk in the system, the first is that crosstalk will reduce the dynamic range making it less sensitive to low light objects, and the second is that crosstalk will create inaccuracies in the spectral information. For our current level of crosstalk (~10%) we anticipate a worst case reduction in our dynamic range from 12 bit to 11 bit which for most biological applications should still be sufficient. The reduction in the quality of our spectral information will require

an additional software calibration step that takes into account the spectral dependence of the crosstalk for each sub-image. Although, this calibration process may be time consuming it is possible and can be implemented with our existing system. Future work will continue to improve the quality of the individual facets in the image mapper to achieve our designed crosstalk of 1%. We believe the majority of this crosstalk is currently due to the surface form error in the facet, however, scattering from the facet surfaces and edges may also contribute to the system and will be further explored in the future. We are also actively working on developing a more advanced calibration procedure to help minimize the effects from crosstalk which may exists in future systems.

7.6. Conclusion

In conclusion, this paper presents a new design and fabrication approach for making compact large format image mappers. The design approach incorporates a multi-tilt (x and y axis) geometry which can be efficiently grouped within a single collecting objectives pupil. Due to the compact nature of the image mapper design, diffraction effects were considered and the design optimized for ~1% crosstalk between adjacent pupils. The unique image mapper geometry was then fabricated using surface shaped diamond tools used in raster flycutting mode on a precision 4-axis diamond turning machine. This fabrication technique was developed specifically for creating large format image mappers as it significantly reduces the fabrication time and makes it possible to create these miniature features. To prove the new design and fabrication methods a 250 element 25 tilt (5 x-tilts, 5 y-tilts) image mapper was fabricated and tested at the component and system level. The geometric accuracy of the image mapper was measured to be < 1 mrad for both x and y directions which is acceptable for our design. Surface roughness for the individual facets was also acceptable for diamond machining techniques with an average roughness of 5.3 nm. This roughness is estimated to decreases the throughput of the image mapper to ~97% which is still high compared to other techniques. Ongoing improvements are still required for the surface form of the mirror facets. Depressions in the mirror facets caused by diamond tool flatness errors are creating additional crosstalk between the pupils. Tools with better flatness and slightly wider (+ 5 microns) are expected to

get our crosstalk down to the designed level of 1%. Software calibration procedures may also be used to remove residual crosstalk in the IMS system; however, dynamic range will be reduced. We are currently exploring new tool fabrication methods such as ion beam etching to get better surface quality tools for the image mapper.

In the future these large format ($\geq$250 element) image mappers will be incorporated into a high resolution IMS fluorescence microscope and/or other biomedical imaging devices. Diffraction effects are also being explored for improving the spectral and/or spatial sampling of the system in addition to minimizing crosstalk between sub-pupils. This work is supported by the National Institute of Health under Grant No. R21EB009186 and R01CA124319.

8. CONCLUSION AND FUTURE WORK

In summary, my research has lead to the development of two important optical imaging technologies for endoscopic imaging for early stage cancer diagnostics. The first technology offers the interesting prospect of low cost, high performance miniature optics for endomicroscopy. This has been demonstrated in the form of a new self-centering miniature objective that has a high NA (NA = 1.0 water immersion) while residing within a total diameter of only 3.9 mm. Initial prototype objectives were assembled in ~15 minutes and required no additional alignment. Test results showed that the objectives achieved near diffraction limited performance with a Strehl ratio of 0.7 – 0.75. This miniature optics technology makes it possible to produce high performance miniature optics for less than $100 in volumes. Biological imaging results obtained with these prototypes display similar image quality as those acquired from research grade microscopes, however are only a fraction of the size and costs. In light of this, applications outside of endoscopy may also benefit from the development of this technology where performance, size, and costs are all critical parameters; these include most diagnostic devices that come in contact with blood such as point-of-care diagnostics and "needle" biopsy systems.

The second major technology breakthrough was the realization of the first ever real-time snapshot hyperspectral endoscope. This hyperspectral endoscope is based on a new principle called image mapping spectroscopy (IMS). A prototype endoscope based on the IMS technology has been developed and shown to obtain 3D (x, y, λ) datacubes of 350 x 350 x 48 at frame rates of 5.2 fps. The tip of the endoscope measures only 1 mm in diameter making it compatible with most endoscope tool channels. The field-of-view and resolution of the endoscope is 7 mm and 62.5 μm respectively. The current spectral window is ~96 nm with a spectral resolution of 4 nm and can be located anywhere between 450 nm – 650 nm. Biological imaging results from the lower lip of a normal volunteer have been obtained and demonstrate the ability of the device to detect vasculature as well as what may be oxy-hemoglobin within the tissue regions although additional testing is required.

I believe the technologies presented here have laid the framework for the much larger vision of constructing an integrated Bi-FOV endoscope for early cancer detection. In the future, work should be focused on integrated these technologies into a single Bi-FOV endoscope system. The following are my recommendations for integration. First, the low cost, high performance, self-centering miniature optics technology (see chapters 3-5) should be implemented at the distal end of the Bi-FOV endoscope. This technology is crucial for the microscopic portion of the system which require miniature high NA objectives that are difficult to obtain. However, this technology may also be beneficial for the macroscopic portion where off-the-shelf components like GRIN lenses produce large chromatic aberrations (see chapter 6). One possible configuration of this technology is shown in figure 8.1.

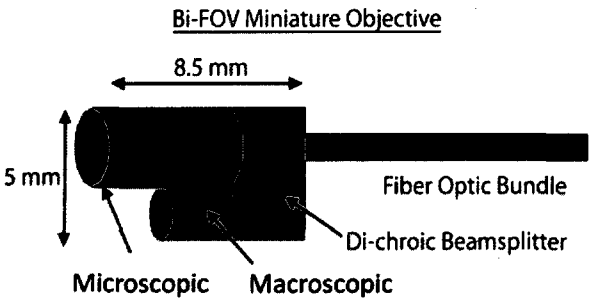

Fig. 8.1 - Conceptual drawing of the Bi-FOV miniature objective for the distal end of the system.

Using this approach both the microscopic and macroscopic systems are placed adjacent to one another in a staggered configuration to accommodate the different working distances. Each system resides within its own hypodermic tubing that is combined together using epoxy. For further integration, the two systems can utilize the same coherent fiber optic bundle through the use of a dichroic beamsplitter attached to either end of the fiber optic bundle. This approach relies on each system operating in a separate spectral region which may not be ideal for some application. In situations where both systems need to operate in the same and/or overlapping spectral domains, each objective should be combined with a separate fiber optic bundle to eliminate crosstalk. Preliminary optical designs using optical design software (ZEMAX) have been developed to see if integration of two different field-of-view objectives using this dichroic approach is feasible. Figure 8.2 shows the 2D layouts for both designs incorporating a dichroic

beamsplitter cube near the image plane. From this initial analysis the biggest concern I have is getting the conjugate planes for the two separate systems aligned. The current designs have object/image conjugate planes separated by 12.6 mm and 8.9 mm for the macroscopic and microscopic systems respectively. The planes will need to be overlapping once the systems are folded into each other to provide simultaneous imaging which may be challenging.

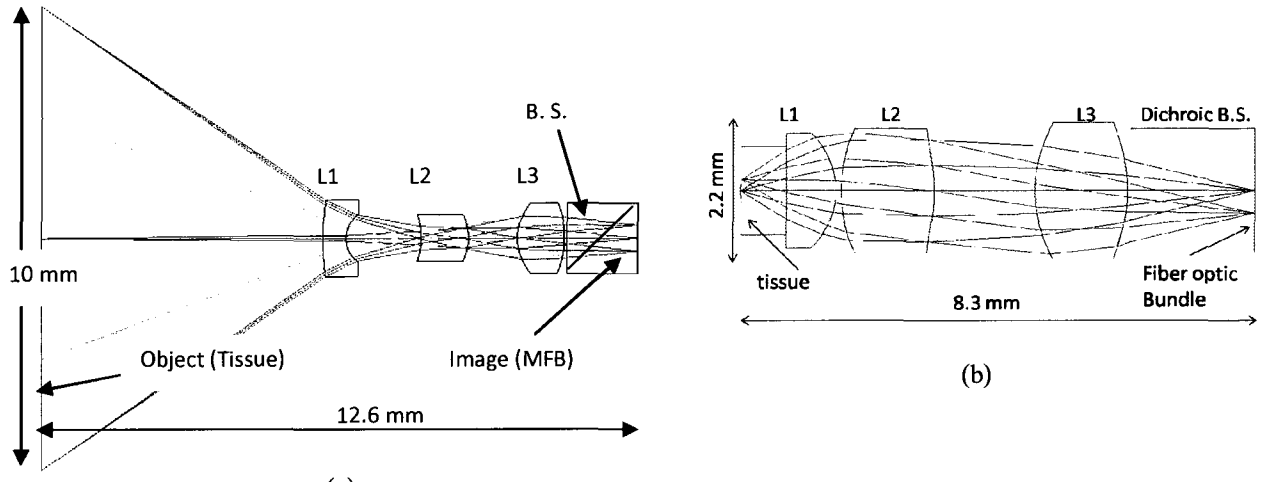

Fig. 8.1 – Optical Design schematics for both the macroscopic (a) and microscopic (b) objectives for the Bi-FOV endoscope.

On the proximal side of the Bi-FOV endoscope, many commercial systems exist on the market today that can be used for the microscopic portion of the imaging system. These systems only require custom miniature optics and a fiber optic bundle for adapting to an endoscope. In particular, Thorlabs, Inc. has a confocal microscope product (VCMS-F) that when combined with the low cost, high performance objectives developed here can provide high resolution images at the tissue surface. Before attaching these objectives to one of these systems, I recommend that the current objective design be achromatized for fluorescence imaging as opposed to the current reflectance imaging since the contrast is much larger due to the reflections from the fiber optic bundle faces. I have spent some time trying to come up with ways to remove these reflections, however, have been unsuccessful without significantly decreasing the performance of the system.

As for the proximal side of the macroscopic imaging portion (i.e. IMS endoscope) several items should continue to be developed. First, the IMS endoscope should be ruggedized. I have already designed a more rugged IMS system as shown in Figure 8.2 and the components have been ordered. The attaching foreoptics and fiber optic probe should also be designed more rugged and attached to this base IMS system.

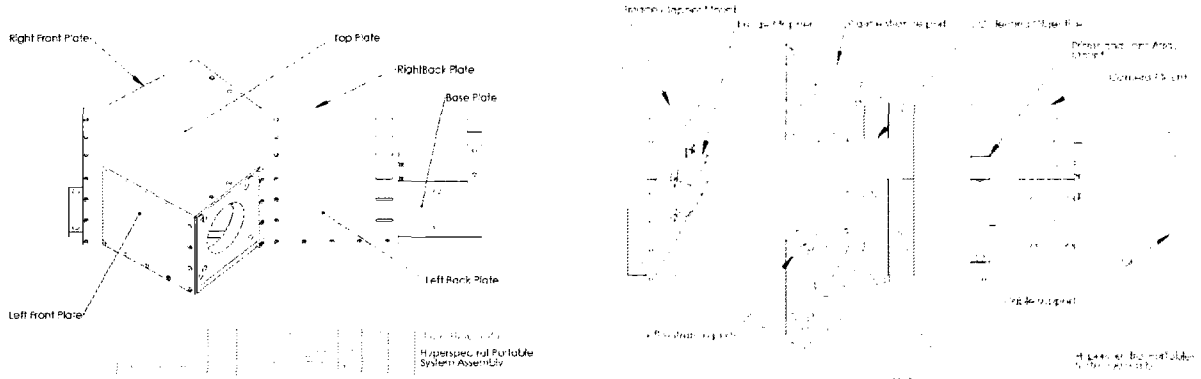

(a) (b)

Figure 8.2 – Drawings for a ruggedized IMS endoscope system for clinical testing. (a) System with cover plates. (b) System without cover plates showing layout of critical components.

Second, the spectral window of the IMS system should be increased to allow instanteous detection from 450 – 650 nm instead of only a ~96nm window like the current system. The design for the increased spectral range has been completed as shown in Figure 8.3. The parts for this system have been ordered and will need to be assembled into the ruggedized IMS system later this summer. The main difference between this new design and the previous design is a new flint material (N-LASF31) with lower dispersion has been used.

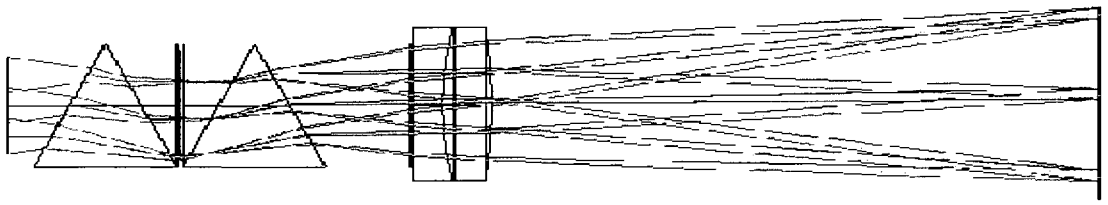

(a)

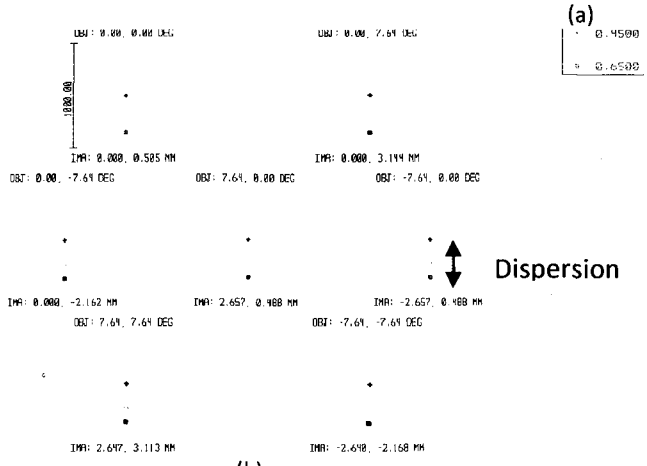

(b)

Field	Dispersion (um)	Dispersion. (pixels)
1	359	49
2	360	49
3	375	51
4	363	49
5	363	49
6	366	49
7	381	51

(c)

Figure 8.3 – Design of IMS prism and lens array for increase spectral window (450-650 nm). (a) Optical Layout, (b) Spot diagram for 7 field positions (x, y), 1=(0, 0), 2 = (0,-7.64), 3 = (0,+7.64), 4(+7.64,0), 5(+7.64,0), 6(+7.64, +7.64), 7(-7.64, -7.64), (c) Dispersion magnitude at this 7 positions in terms of distance and pixels on the CCD camera.

And third, real-time analysis software will need to be developed to identify certain biochemical features within the tissue. For example, tissue regions that have low levels of oxyhemoglobin can be false colored on the visual display to help guide the clinician to those sites. Some of the development of this software can be done in a lab setting; however, most of it will require clinical testing with our collaborator Dr. Anne Gillenwater which should start by the end of 2010, beginning of 2011.

REFERENCES

1. Allington-Smith J. R., Content R., Dubbeldam C.M., Robertson D. J. Preuss W., New techniques for integral field spectroscopy. I. Design, construction and testing of the GNIRS IFU, *Monthly Notices of the Royal Astronomical Society*, **371**, 380-94 (2006).
2. Allington-Smith J. R., Dubbeldam C.M., Content R., Robertson D., Turner J., Rodgers B., Elias J., Gerssen J., Swinbank, M., New techniques for integral field spectroscopy. II. Performance of the GNIRS IFU, *Monthly Notices of the Royal Astronomical Society*, **376**, 785-92 (2007).
3. Allington-Smith J., R. Content, and R. Haynes, "New developments in Integral Field Spectroscopy," Proc. SPIE **3355**, 196-205 (1998).
4. American Cancer Society: Cancer Facts and Figures; 2008. http://www.cancer.org/downloads/STT/2008CAFFfinalsecured.pdf
5. Bao H., J. Allen, R. Pattie, R. Vance, M. Gu, "Fast handheld two-photon fluorescence microendoscope with a 475 μm X 475 μm field of view for *in vivo* imaging," Opt. Lett. **33**, 1333-1335 (2008).
6. Barrett H. H., and K. J. Myers, *Foundations of Image Science* (Wiley, 2004).
7. Barretto R. P. J., B. Messerschmidt, M. J. Schnitzer, "*In vivo* fluorescence imaging with high-resolution microlenses," *Nat Methods* **6**; 511-512 (2009).
8. Bird D., Min G., Two-photon fluorescence endoscopy with a micro-optic scanning head, *Opt. Lett.*, **28**, 1552-4 (2003).
9. Bodkin A., Sheinis A. I., Norton A., "Hyperspectral imaging systems," U. S. Patent 20060072109A1 (2006).
10. Bonneville C., E. Prieto, P. Ferruit, F. Henault, J. P. Lemonnier, F. Prost, R. Bacon, O. Le Fevre, "Design, prototypes and performances of an image slicer system for integral field spectroscopy," Proc. SPIE, **4842**, 162-173 (2003).
11. Burns P. D., "Slanted-Edge MTF for Digital Camera and Scanner Analysis," Proc. IS&T 2000 PICS Conference, 135-138 (2000).
12. Carlson K., Chidley M. Sung K.B., Descour M., Gillenwater A., Follen M., Richards-Kortum R., In vivo fiber-optic confocal reflectance microscope with an injection-molded plastic miniature objective lens, *Appl. Opt.*, **44**, 1792-7 (2005).
13. Chang S.K., Mirabal Y.N., Atkinson E.N., Cox D., Malpica A., Follen M., Richards-Kortum R., Combined reflectance and fluorescence spectroscopy for in vivo detection of cervical pre-cancer, *J. Biomed. Opt.*, **10**, 024031 (2005).
14. Chidley M. D., C. Liang, M. Descour, K.B. Sung, R. Richards-Kortum, and A. Gillenwater, "Miniature injection-molded optics for fiber optic, *in vivo* confocal microscopy," in International Optical Design Conference, P.K. Manhart and J.M. Sasian, ed., Proc. SPIE **4832**, 126-136 (2002).
15. Chidley M.D., Carlson K.D., Richards-Kortum R., and Descour M.R., Design, assembly, and optical bench testing of a high-numerical-aperture miniature injection-molded objective for fiber-optic confocal reflectance microscopy, *Appl. Opt.*, **45**, 2545-54 (2006).
16. Christodoulides N., S. Mohanty, C. S. Miller, M. C. Langub, P. N. Floriano, P. Dharshan, M. F. Ali, B. Bernard, D. Romanovicz, E. Anslyn, P. C. Fox, J. T. McDevitt , "Application of microchip assay system for the measurement of C-reactive protein in human saliva," Lab Chip, **5**, 261-269 (2005).
17. Collier T., Guilland M., Follen M., Malpica A., Richards-Kortum R., "Real-time reflectance confocal microscopy: comparison of two-dimensional images and three dimensional image stacks for detection of cervical precancer," J. Biomed. Opt. **12**(2), 024021 (2007).
18. Content R., "Slicer system of KMOS," N. Astron. Rev. **50**, 374-377 (2006).
19. Content R., Dubbeldam C.M., Robertson D.J., Sharples R.M., Morris S.L., Large-field reflective integral field systems for visible and infrared spectroscopy, *Proc. SPIE*, **5492**, 281-92 (2004).

20. Curvers W.L., Singh R., Wong-Kee Song L-M., Wolfsen H.C., Ragunath K., Wang K., Wallace M.B., Fockens P., and Bergman J. J. G. H. M., Endoscopic tri-modal imaging for detection of early neoplasia in Barrett's oesophagus: a multi-centre feasibility study using high resolution endoscopy, autofluorescence imaging, and narrow band imaging. *Gut,* **57**, 167-172 (2008).
21. Descour M.R., Volin C.E., Dereniak E.L., and Thome K.J., Demonstration of a high-speed nonscanning imaging spectrometer, *Opt. Lett.*, **22**, 1271-1273 (1997).
22. Downer MC, Moles DR, Palmer S, Speight PM. A systematic review of test performance in screening for oral cancer and precancer. *Oral Oncol,* **40**(3), 264–73 (2004);.
23. Drezek R., Brookner C., Pavlova I., Boiko I., Malpica A., Lotan R., Follen M., Richards-Kortum R., "Autofluorescence microscopy of fresh cervical-tissue sections reveals alterations in tissue biochemistry with dysplasia," *Photochem Photobiol* **73**, 636-41 (2001).
24. Drezek, R. et al. Autofluorescence microscopy of fresh cervical-tissue sections reveals alterations in tissue biochemistry with dysplasia. *Photochem Photobiol* **73**, 636-41 (2001).
25. Dubbeldam C. M., D. J. Robertson, "Freeform Diamond Machining of Complex Monolithic Metal Optics for Innovative Astronomical Applications," Proc. SPIE, **6149**, 61490R (2006).
26. Flusberg B.A., Cocker E.D., Piyawattanametha W., Jung J.C., Cheung E.L.M., and Schnitzer M.J., Fiber-optic fluorescence imaging, Nat. Methods, **12**, 941 (2005).
27. Flusberg B.A., Jung J.C., Cocker E.D., Anderson E.P., Schnitzer M.J., In vivo brain imaging using a portable 3.9 gram two-photon fluorescence microendoscope, *Opt. Lett.*, **30**, 2272-4 (2005).
28. Ford B. K., Volin C. E., Murphy S. M., Lynch R. M., Descour M. R., "Computed tomography-based spectral imaging for fluorescence microscopy," *Biophysical*, **80**, 986-93 (2001).
29. Ford B., M. Descour, and R. Lynch, "Large-image-format computed tomography imaging spectrometer for fluorescence microscopy," Opt. Express **9**(9), 444–453 (2001).
30. Frangioni J.V., In vivo near-infrared fluorescence imaging, *Current Opinion in Chemical Biology,* **7**, 626-634 (2003).
31. Gao L., Kester R. T., N. Hagen, Tkaczyk T. S., "Snapshot Image Mapping Spectrometer (IMS) with high sampling density for hyperspectral microscopy," *Opt Express*, in review (2010).
32. Gao L., Kester R. T., Tkaczyk T. S., "Compact Image Slicing Spectrometer (ISS) for hyperspectral fluorescence microscopy," *Opt Express* **17**, 12293-12308 (2009).
33. Gebhart S.C., Thompson R.C., and Mahadevan-Jansen A., "Liquid-crystal tunable filter spectral imaging for brain tumor demarcation." *Appl. Opt.,* **46**, 1896-1910 (2007).
34. Gehm M. E., John R., Brady D. J., Willett R. M., Schulz T. J., "Single-shot compressive spectral imaging with a dual-disperser architecture," *Opt Express* **15**, 14013-14027 (2007).
35. Given Imaging, http://www.givenimaging.com/en-us/Pages/GivenWelcomePage.aspx
36. González S. and Tannous Z., Real-time, in vivo confocal reflectance microscopy of basal cell carcinoma, *J Am Acad Dermatol* ,**47, 869-874** (2002).
37. Henault F., R. Bacon, R. Content, B. Lantz, F. Laurent, J. Lemonnier, and S. Morris, "Slicing the universe at affordable cost: the quest for the MUSE image slicer," Proc. SPIE **5249**, 134–145 (2004).
38. Henk L. Malignant Tumors of the Oral Cavity. London: Edwad Arnold, 1985
39. Horner M.J., Ries L.A.G., Krapcho M., Neyman N., Aminou R., Howlader N., Altekruse S.F., Feuer E.J., Huang L., Mariotto A., Miller B.A., Lewis D.R., Eisner M.P., Stinchcomb D.G., Edwards B.K. (eds). SEER Cancer Statistics Review, 1975-2006, National Cancer Institute. Bethesda, MD, http://seer.cancer.gov/csr/1975_2006/, based on November 2008 SEER data submission, posted to the SEER web site, 2009.
40. Hsiung P. L., Hardy J., Friedland S., Soetikno R., Du C. B., Wu A. P., et al. Detection of colonic dysplasia in vivo using a targeted heptapeptide and confocal microendoscopy. *Nat Med, **14***, 454–458 (2008).
41. Jean F., G. Bourg-Heckly, and B. Viellerobe, "Fibered confocal spectroscopy and multicolor imaging system for in vivo fluorescence analysis," *Opt. Express* **15**, 4008-4017 (2007).

42. Jung J. C., A. D. Mehta, E. Aksay, R. Stepnoski, M. J. Schnitzer, "*In vivo* mammalian brain imaging using one- and two-photon fluorescence microendoscopy," *J. Neurophysiol.* **92**, 3121–3133 (2004).
43. Jung J., Schnitzer M.J., Multiphoton endoscopy, Opt. Lett., **28**, 902-4 (2003).
44. Kano A., Rouse A.R., Kroto S.M., Gmitro A.F., Microendoscopes for imaging of the pancreas, Proc. SPIE, **5318**, 50-58 (2004).
45. Kara M. A., Peters F.P., Fockens P.,ten Kate F.J.W., and Bergman J.J.G.H.M., "Endoscopic video-autofluorescence imaging followed by narrow band imaging for detecting early neoplasia in Barrett's esophagus." *Gastrointest. Endosc.,* **64**, 176–185 (2006).
46. Kara M.A., Peters F.P., Fockens P.,ten Kate F.J.W., and Bergman J.J.G.H.M., Endoscopic video-autofluorescence imaging followed by narrow band imaging for detecting early neoplasia in Barrett's esophagus. *Gastrointest. Endosc.,* **64**, 176–185 (2006).
47. Karadaglic D., Juskaitis R., Wilson T., Confocal endoscopy via structured illumination, *Scanning*, **24**, 301-304 (2002).
48. Kester R. T., Gao L., Tkaczyk T. S., "Development of image mapping field units for hyperspectral biomedical imaging applications," *Appl Opt.*, **49**, 1886-1899 (2010)
49. Kester R.T., T. Christenson, R. Richards Kortum, and T. S. Tkaczyk, "Low cost, high performance, self-aligning miniature optical systems," *Appl. Opt.* **48**, 3375-3384 (2009).
50. Kester R.T., Tkaczyk T.S., Descour M.R., Christenson T., Richards-Kortum R., High numerical aperture microendoscope objective for a fiber confocal reflectance microscope, *Opt. Express,* **15**, 2409-2420 (2007).
51. Kumar S., Sokolav K., Richards-Kortum R., In vivo optical detection of intranuclear cancer biomarkers using gold nanoparticles, *Proc. SPIE*, **6095**, 609504-1-10 (2006).
52. Lane P.M., Gilhuly T., Whitehead P., et al., "Simple device for the direct visualization of oral-cavity tissue fluorescence," *J. Biomed. Opt.*, **11**, 024006 (2006).
53. Lane P.M., Gilhuly T., Whitehead P., et al., Simple device for the direct visualization of oral-cavity tissue fluorescence, *J. Biomed. Opt.*, **11**, 024006 (2006).
54. Laurent F., F. Henault, E. Renault, R. Bacon, and J. Dubois, "Design of an Integral Field Unit for MUSE, and Results from Prototyping," Publ. Astron. Soc. Pac. **118**(849), 1564–1573 (2006).
55. Laurent F., Renault E., Bacon R., Dubois J.P., Henault F., Robert D., Optical design, manufacturing, and tests of the MUSE image slicer, *Proc.SPIE*, **5965**, 59650J-1-12 (2005).
56. Lee D., Wells M., Dickson C.J., Shore P., Morantz P., Development of diamond machined mirror arrays for integral field spectroscopy, *Proc. SPIE*, **6273**, 62731Y-1-9 (2006).
57. Levene M. J., D. A. Kasischke, K. A. Molloy, W. W. Webb, "In vivo multiphoton microscopy of deep brain tissue," J. Neurophysiol. **91**, 1908-1912 (2004).
58. Li X., C. Chudoba, T. Ko, C. Pitris, J. G. Fujimoto, "Imaging needle for optical coherence tomography," Opt. Lett. **25**, 1520-1522 (2000).
59. Liang C., "Design of miniature microscope objective optics for biomedical imaging," Ph.D. dissertation, The University of Arizona (2002).
60. Liang C., K.B. Sung, R. Richards-Kortum, and M.R. Descour, "Design of a high-numerical-aperture miniature microscope objective for an endoscopic fiber confocal reflectance microscope," *Appl. Opt.*, **41**, 4603-4610 (2002).
61. Liang C., Sung K.B., Richards-Kortum R., Descour M.R., Fiber confocal reflectance microscope (FCRM) for in-vivo imaging, Opt. Express, **9**, 821-830 (2001).
62. Lin A. W., N. A. Lewinski, J. L. West, N. J. Halas, R. A. Drezek, "Optically tunable nanoparticle contrast agents for early cancer detection: model-based analysis of gold nanoshells," *J. Biomed Opt.*, **10**, 064035 (2005).
63. Loewke K., Camarillo, D., Piyawattanametha W., Breeden D., and Salisbury K., Real-time image mosaicing with a hand-held dual axis confocal microscope, *Proc. SPIE*, **6851**, 68510F-1-9 (2008).
64. Madou M. J., *Fundamentals of Microfabrication 2nd ed.* (CRC Press 2002).

65. Maitland K.C., Gillenwater A., Williams M.D., El-Naggar A.K., Descour M.R., and Richards-Kortum R., In vivo imaging of oral neoplasia using a miniaturized fiber optic confocal reflectance microscope, *Oral Oncology*, ***44***, 1059-1066 *(2008).*
66. Martin M.E.,Wabuyele M.B., Chen K., et al. "Development of an advanced hyperspectral imaging (HSI) system with applications for cancer detection." *Ann Biomed Eng.*, **34**, 1061-1068 (2006).
67. Mathews S. A., "Design and fabrication of a low-cost, multispectral imaging system," *Appl Opt.,* **47**, 71-76 (2008).
68. Matsuoka H., Kosai Y., Saito M., Takeyama N., Suto H., "Single-cell viability assessment with a novel spectro-imaging system," *J Biotech,* **94**, 299-308 (2002).
69. Meining A., Bajbouj M., Delius S., Prinz C., Confocal Laser Scanning Microscopy for in Vivo Histopathology of the Gastrointestinal Tract., Arab J. of Gastroenterol, 8, 1-4 (2007).
70. Miyajima H., Murakami K., Katashiro M., MEMS Optical Scanners for Microscopes, *IEEE J. Selected Topics in Quantum Electronics, 10*, 514-527 (2004).
71. Myaing M.T., MacDonald D.J., Xingde L., Fiber-optic scanning two-photon fluorescence endoscope, *Opt. Lett.,* **31**, 1076-8 (2006).
72. Myers F. B., Lee L.P., "Innovations in optical microfluidic technologies for point-of-care diagnostics," *Lab Chip*, **8,** 2015-2031 (2008).
73. Nadeau V., Hamdan K., Hewett J., Sibbett W., Tait I., Cuschieri A., Padgett M., Endoscopic fluorescence imaging and point spectroscopy system for the detection of gastro-intestinal cancers, *J. Modern Opt.*, **49**, 731-41 (2002).
74. Olympus Corporation: http://www.olympusconfocal.com/theory/resolutionintro.html
75. Osdiot A., Lacombe, C., Cave C., Loiseau S., Peltier E., To see...the unseeable: confocal miniprobes for routine microscopic imaging during endoscopy. Proc. SPIE ,**6432**, 64320F-1 (2007)
76. Osdoit A., Magalie G., Perchant A., Loiseau S., Abrat B., In vivo fibered confocal reflectance imaging: totally non-invasive morphological cellular imaging brought to the endoscopist. *Proc. SPIE*, **6082**, 608208 (2006)
77. Pan, Z., Healey G., Prasad M., and Tromberg B., "Hyperspectral face recognition under variable outdoor illumination," *Proc. SPIE,* **5425**, 520-529 (2004).
78. Park H., H. Jang, E. Song, C. L. Chang, M. Lee, S. Jeong, J. Park, B. Kang and C. Kim, "Detection and Genotyping of *Mycobacterium* Species from Clinical Isolates and Specimens by Oligonucleotide Array," *J. Clin. Microbiol.*, 2005, **43**, 1782–1788.
79. Parkin D.M., Bray F., Ferlay J., Pisani P., Estimating the world cancer burden: Globocan 2000, *Int J Cancer*, **94**, 153-6 (2001).
80. Pickard D.C., Bigio I.J., Bown S.G., Lovat L.B., Ripley P.M., Novelli M., Optical biopsy for the diagnosis of dysplasia in Barrett's oesophagus, *Proc. SPIE,* **4613**, 234-43 (2002).
81. Piyawattanametha W., E. D. Cocker, L. D. Burns, R. P. J. Barretto, J. C. Jung, H. Ra, O. Solgaard, M. J. Schnitzer, "*In vivo* brain imaging using a portable 2.9 g two-photon microscope based on a microelectromechanical systems scanning mirror," *Opt. Lett.* **34**; 2309-2311 (2009).
82. Pluta M., *Advanced Light Microscopy vol. 1*, (Elsevier 1988).
83. Preuss W., K. Rickens, "Precision machining of integral field units," N. Astron. Rev. **50**, 332–336 (2006).
84. Ra H., Piyawattanametha W., Taguchi Y., Lee D., Mandella M., Solgaard O., Two-Dimensional MEMS Scanner for Dual-Axes Confocal Microscopy, *J. Microelectromech. Syst.*, **16**, 969-976 (2007).
85. Ries L.A.G., Melbert D., Krapcho M., Stinchcomb D.G., Howlader N., Horner M.J., Mariotto A., Miller B.A., Feuer E.J., Altekruse S.F., Lewis D.R., Clegg L., Eisner M.P., Reichman M., Edwards B.K. (eds). *SEER Cancer Statistics Review, 1975-2005*, National Cancer Institute. Bethesda, MD, http://seer.cancer.gov/csr/1975_2005/, based on November 2007 SEER data submission, posted to the SEER web site, 2008.
86. Roblyer D., Kurachi C., Gillenwater A.M., Richards-Kortum R., "In vivo fluorescence hyperspectral imaging of oral neoplasia," *Proc. SPIE*, **7169**, 71690J-10 (2009).

87. Rogers J.D., Landau S., Tkaczyk T.S., and Descour M.R., Imaging performance of a miniature integrated microendoscope, *J. Biomed. Opt.*, **13**, 054020-1 (2008).
88. Rouet F., D. K. Ekouevi, M. Chaix, M. Burgard, A. Inwoley, T. D. Tony, C. Danel, X. Anglaret, V. Leroy, P. Msellati, F. Dabis and C. Rouzioux, "Transfer and Evaluation of an Automated, Low-Cost Real-Time Reverse Transcription-PCR Test for Diagnosis and Monitoring of Human Immunodeficiency Virus Type 1 Infection in a West African Resource Limited Setting," *J. Clin. Microbiol.*, 2005, **43**, 2709–2717.
89. Rouse A. R., A. Kano, J. A. Udovich, S. M. Kroto, and A. F. Gmitro, "Design and Demonstration of a Miniature Catheter for a Confocal Microendoscope," *Appl. Opt.* **43**, 5763-5771 (2004).
90. Rouse A. R., J. A. Udovich, A. R. Gmitro, "In-vivo multi-spectral confocal microscopy," Proc. SPIE **5701**, 73-84 (2005)
91. Rouse A.R., Kano A., Gmitro A.F., Development of a fiber-optic confocal microendoscope for clinical endoscopy, *Proc. SPIE,* **4613**, 244-253 (2002).
92. Sakamoto J.M.S., Higuti R.T., Pacheco G.M., Kitano C., Overlap integral factor applied to reflective fiber optic displacement sensor: theory and experiment, Submitted to XXX Encontro Nacional de Física da Matéria Condensada, São Lourenço, MG, May 2007.
93. Sandler HC. Cytological screening for early mouth cancer, *Cancer*, **15**, 1119–24 (1962).
94. Schmoll J., D. J. Robertson, C. M. Dubbeldam, F. Bortoletto, L. Pina, R. Hudec, E. Prieto, C. Norrie, and S. Ramsay-Howat, "Optical replication techniques for image slicers," N. Astron. Rev. **50**, 263–266 (2006).
95. SEER Cancer Statistics Review; 1973–1998. <http://seer.cancer.gov/csr/1973_1998/index.html>.
96. Seibel E.J., Johnston R.S., Melville C.D., A full-color scanning fiber endoscope, *Proc. SPIE*, **6083**, 608303-1-8 (2006).
97. Sharma P., Bansal A., Mathur S., Wani S., Cherian R., McGregor D., Higbee A., Hall S., and Weston A., "The utility of a novel narrow band imaging endoscopy system in patients with Barrett's esophagus," *Gastrointest. Endosc.* **64**, 167–175 (2006).
98. Sharma U., Kang J.U., Common-path optical coherence tomography with side-viewing bare fiber probe for endoscopic optical coherence tomography, *Rev. Sci. Instrum.*, **78**, 113102 (2007).
99. Shin H.J., Pierce M.C., Lee D., Ra H., Solgaard O., and Richards-Kortum R., Fiber-optic confocal microscope using a MEMS scanner and miniature objective lens, *Opt. Express*, **15**, 9113-22 (2007).
100. Silverman Jr S. Early diagnosis of oral cancer. *Cancer,* **62** (8), 1796–9 (1988).
101. Smith J. A., "Basic principles of integral field spectroscopy," N. Astron. Rev. **50**(4-5), 244–251 (2006).
102. Soufli R., E. Spiller, M. A. Schmidt, J. C. Robinson, S. L. Baker, S. Ratti, and M. A. Johnson, "Smoothing of diamond-turned substrates for extreme ultraviolet illuminators," Opt. Eng, **43**(12), 3089-3095 (2004).
103. Sung K. B., C. Liang, M. Descour, T. Collier, M. Follen, A. Malpica, R. Richards-Kortum, "Near real time in vivo fibre optic confocal microscopy: sub-cellular structure resolved," *J. of Microsc.*, **207**, 137–145 (2002).
104. Sung K.B., Richards-Kortum R., Follen M., Malpica A., Liang C. and Descour M., Fiber optic confocal reflectance microscopy: a new real-time technique to view nuclear morphology in cervical squamous epithelium in vivo, Opt. Express, **11**, 3171-3181 (2003).
105. Tanbakuchi A. A., J. A. Udovich, A. R. Rouse, K. D. Hatch, A. F. Gmitro, "*In vivo* imaging of ovarian tissue using a novel confocal microlaparoscope," Am J Obstet Gynecol 202, 90; e1-9 (2010).
106. Tecza M., N. Thatte, F. Clarke, T. Goodsall, D. Freeman, Y. Salaun, "SWIFT Image Slicer: large format, compact, low scattering image slicing," Proc. SPIE, **6273**, 62732L (2006).
107. The MEMS Handbook, 2nd Edition, Mohamed Gad-el-Hak, ed., CRC Tayor & Francis, Boca Raton, v.2, MEMS Design and Fabrication, Ch. 5, X-Ray Based Fabrication, 2006.
108. Tkaczyk T.S., Rahman, M., Mack V., Sokolov K., Rogers J.D., Richards-Kortum R., Descour M.R., High resolution, molecular-specific, reflectance imaging in optically dense tissue phantoms with structured-illumination, *Opt. Express*, **12**, 3745-3758 (2004).

109. Todd S. P., M. Wells, S. K. Ramsay Howat, P. R. Hastings, "A cryogenic image slicing IFU for UKIRT – manufacture, alignment, laboratory testing and data reduction," Proc. SPIE, **4842**, 151-161 (2003).
110. Tumlinson A.R., Barton J.K., Povazay B., Sattman H., Unterhuber A., Leitgeb R.A., Drexler W., Endoscope-tip interferometer for ultrahigh resolution frequency domain optical coherence tomography in mouse colon, *Opt. Express*, **14**, 1878-87 (2006).
111. Udovich J.A., Rouse A.R., Tanbakuchi A., Brewer M.A., Sampliner R., Gmitro A.F., Confocal microendoscope for use in a clinical setting, *Proc. SPIE* 6432, 64320H (2007).
112. US Mortality Data 2005, National Center for Health Statistics, Centers for Disease Control and Prevention, 2008.
113. Verpoorte E., "Chip vision-optics for microchips," *Lab Chip*, **3**, 42N-52N (2003).
114. Vivès S., and E. Prieto, "Original image slicer designed for integral field spectroscopy with the near-infrared spectrograph for the James Webb Space Telescope," Opt. Eng. **45**(9), 093001 (2006).
115. Vives S., E. Prieto, Y. Salaun, P. Godefroy, "New technological developments in Integral Field Spectroscopy," Proc. SPIE, **7018**, 70182N (2008).
116. Vives S., Prieto E., Original image slicer designed for integral field spectroscopy with the near-infrared spectrograph for the James Webb Space Telescope, *Opt. Eng.*, **45**, 93001-1-6 (2006).
117. Vo-Dinh T., "A hyperspectral imaging system for in vivo optical diagnostics," *IEEE* , **23**, 40-49 (2004).
118. Wagadarikar A. A., N. P. Pitsianis, X. Sun, and D. J. Brady, "Video rate spectral imaging using a coded aperture snapshot spectral imager," Opt. Express **17**(8), 6368–6388 (2009).
119. Warger II, W.C., Guerrera, S.A., and DiMarzio C.A., Toward a compact dual-wedge point scanning confocal reflectance microscope, *Proc. SPIE*, **6443**, 644311 (2007).
120. Weitzel L., A. Krabbe, H. Kroker, N. Thatte, L. E. Tacconi-Garman, M. Cameron, and R. Genzel, L. E. Tacconi, Garman, M. Cameron and R. Genzel, "3D: The next generation near-infrared imaging spectrometer," Astron. Astrophys. Suppl. Ser. **119**(3), 531–546 (1996).
121. Werning J.W., Oral cancer: diagnosis, management, and rehabilitation, Thieme, 33-35 (2007).
122. Wetherall W.B., "The Calculation of Image Quality," in *Applied Optics and Optical Engineering*, R. R. Shannon, and J. C. Wyant, eds. , vol. 8 (Academic, 1980), pp. 171-316.
123. Wickline S.A., Neubauer A.M., Winter P.M., Caruthers S.D., Lanza G.M., Molecular imaging and therapy of atherosclerosis with targeted nanoparticles. *J Magn Reson Imaging,* **25**, 667-680 (2007).
124. Wilson B. C., "Detection and treatment of dysplasia in Barrett's esophaus: a pivotal challenge in translating biophotonics from bench to bedside," *J. Biomed Opt.*, **12**(5) 051401 (2007).
125. Wu Y., Y. Leng, J. Xi, X. Li, "Scanning all-fiber-optic endomicroscopy system for 3D nonlinear optical imaging of biological tissues," *Opt. Express* **17**; 7907-7915 (2009).
126. Wu Y., Zheng W., Qu J.Y., "Time-resolved confocal fluorescence spectroscopy reveals the structure and metabolic state of epithelial tissue," *Proc. SPIE*, **6430**, 643013 (2007).
127. Yager P., T. Edwards, E. Fu, K. Helton, K. Nelson, M. R. Tam and B. H. Weigl, "Microfluidic diagnostics technologies for global public health," *Nature*, 2006, **442**, 412–418.
128. Zanati S.A., Marcon N.E., Cirocco M., Bassett N., Streutker C., Kandel G.P., Kortan P.P., Rychel S., Douplik A., and Wilson B.C., Oncol-LIFE fluorescence imaging during colonoscopy assists in the differentiation of adenomatous and hyperplastic polyps and improves the detection rate of dysplastic lesions in the colon," *Endosc.* (in press).
129. ZEMAX Development Corporation: http://www.zemax.com.
130. Zonios G., Perelman L.T., Backman V., Manoharan R., Fitzmaurice M., Van Dam J., Feld M.S., Diffuse reflectance spectroscopy of human adenomatous colon polyps in vivo, *Appl. Opt.*, **38**, 6628-6637 (1999).